

Simulation of Chain Exchange Between Ordered Block Copolymer Micelles: Influence of Chain Architectures

by

M. Shane Holden

A Thesis

Presented to

The University of Guelph

In partial fulfilment of requirements

for the degree of

Master of Science

in

Physics

Guelph, Ontario, Canada

© M. Shane Holden, May, 2019

Abstract

SIMULATION OF CHAIN EXCHANGE BETWEEN ORDERED BLOCK COPOLYMER MICELLES: INFLUENCE OF CHAIN ARCHITECTURES

M. Shane Holden
University of Guelph 2019

Advisor:
Professor Robert Wickham

We examine kinetics of chain exchange of block copolymers between body-centered cubic ordered spherical micelles, focusing on the influence of chain architectures. We compare linear AB, ABA and BAB block copolymers using dynamical self-consistent field theory simulations. We connect equilibrium properties such as micelle aggregation number, unimer fraction and micelle volume to chain exchange kinetics. The effects of different equilibrium structures on chain exchange are found by measuring the chain exchange of labelled chains and chain self-diffusion for pure melts of each chain architecture. To eliminate influences of equilibrium structure on dynamics, we perform simulations of tracer triblocks in a constant array of micelles formed by AB diblocks. Comparisons of the tracer diffusion coefficients show that BAB triblocks diffuse faster, due to the looping of the core block at the micelle core-corona interface, than AB diblocks while ABA triblocks diffuse slower than AB diblocks due to the additional core block.

Acknowledgements

First, I would like to extend my thanks and gratitude to the entire Department of Physics at the University of Guelph for their continued support both inside and outside of the office. The welcoming atmosphere and friendly office culture has been a genuinely pleasant experience since day one.

Specifically, I would like to thank my supervisor Rob Wickham, whose advice and guidance were invaluable to this thesis. I owe a lot to the support provided by Rob throughout this degree and, for that, I am eternally grateful. As well, I would like to thank the discussions held between the entire Wickham group for being insightful and often entertaining.

I would also like to extend my thanks to my advisory committee of An-Chang Shi and Mark Matsen whose expertise helped shape and guide this thesis.

While it often goes without saying, I would like to thank my mother, Karen Moore. She has always been there for me, despite being halfway across the country.

And of course, I would like to thank all of my friends and family who have supported me along the way.

Contents

Abstract	ii
Acknowledgements	iii
List of Figures	vi
List of Tables	viii
1 Introduction	1
1.1 Theory of Polymers	1
1.2 Exchange Kinetics of Block Copolymers	5
1.2.1 Experimental Observations	5
1.2.2 Theoretical Methods	8
1.3 Polymer Dynamics Theories	11
1.3.1 The Rouse Model	11
1.3.2 Kramer’s Transition State Theory	12
2 Dynamical Self-Consistent Field Theory	14
2.1 The Microscopic Model	15
2.2 Dynamical Mean-Field Approximation	18
2.2.1 Dimensionless Mean-Field Equations for Triblock Copolymers	26
3 Simulation Details	27
3.1 Numerical Method	27
3.1.1 Initialization	28
3.1.2 Calculation of the Density Field	29
3.1.3 Calculation of the Dynamical Mean Force-Field	29
3.1.4 MPI Communication Routines	34
3.1.5 Time Evolution Algorithm	36
3.1.6 BCC Ordering Field	42
3.2 Analysis and Routines	43
3.2.1 Estimation of Equilibrium BCC Period	43
3.2.2 Chain Labelling	49
3.2.3 Calculation of chain extraction relaxation time	50
3.2.4 Aggregate Equilibrium Properties	51

4	Results	53
4.1	Equilibrium Properties	54
4.1.1	AB Diblock Copolymer Melt	54
4.1.2	ABA Triblock Copolymer Melt	60
4.1.3	BAB Triblock Copolymer Melt	64
4.1.4	AB/ABA Copolymer Blends	71
4.1.5	AB/BAB Copolymer Blends	75
4.2	Dynamical Properties	76
4.2.1	AB Diblock Copolymer Melt	76
4.2.2	ABA Triblock Copolymer Melt	81
4.2.3	BAB Triblock Copolymer Melt	83
4.2.4	AB/ABA Copolymer Blends	86
4.2.5	AB/BAB Copolymer Blends	88
5	Conclusion	90
A	Discrete Cosine Transform	95
B	Kramers' Barrier Hopping Problem	98
	Bibliography	101

List of Figures

1.1	Schematic illustration of block copolymer architectures	3
1.2	Illustration of diblock copolymer ordered phases	4
1.3	Illustrative example of a spherical micelle formed by diblock copolymers . . .	4
1.4	Experimental relaxation function curves	6
1.5	Schematic illustration of proposed chain exchange mechanisms	8
3.1	Diagram illustrating grid-labelling method	31
3.2	Schematic diagram of tree-structured communication algorithm	35
3.3	Average micelle core volume as a function of L/n	48
4.1	Slice of AB diblock copolymer melt phase diagram	55
4.2	Compositional order parameter of AB diblock copolymer melts at different segregation strengths	56
4.3	AB diblock copolymer melt average aggregation number	57
4.4	AB diblock copolymer melt unimer fraction	58
4.5	AB diblock copolymer melt average micelle core volume	59
4.6	ABA triblock phase diagram	60
4.7	ABA triblock copolymer melt average aggregation number	62
4.8	ABA triblock copolymer melt unassociated core block fraction	63
4.9	ABA triblock copolymer melt average micelle core volume	64
4.10	Slice of BAB triblock copolymer melt phase diagram	65
4.11	BAB triblock copolymer melt average aggregation number	66
4.12	BAB triblock copolymer melt unimer fraction	67
4.13	BAB triblock copolymer melt average micelle core volume	68
4.14	A-monomer density cross section through micelle centroids	69
4.15	BAB copolymer melt average aggregation number N dependence	70
4.16	BAB micelle core volume N dependence	71
4.17	Radial probability density distribution of AB/ABA blends	74
4.18	Radial probability density distribution of AB/BAB blend	75
4.19	AB diblock copolymer melt contrast function at various ϵN	77
4.20	AB diblock copolymer melt relaxation times at various ϵN	78
4.21	AB diblock copolymer melt mean-squared displacement curves	80
4.22	AB diblock copolymer melt diffusion coefficient at various ϵN	81
4.23	ABA triblock copolymer melt relaxation times at various ϵN	82
4.24	ABA triblock copolymer melt diffusion coefficient at various ϵN	83

4.25	BAB copolymer melt relaxation time N dependence	84
4.26	BAB triblock copolymer melt relaxation times at various ϵN	85
4.27	BAB triblock copolymer melt diffusion coefficient at various ϵN	86
4.28	AB/ABA polymer blend diffusion coefficient at various ϵN	88
4.29	AB/BAB polymer blend diffusion coefficient at various ϵN	89
B.1	Illustration of Kramers barrier hopping problem	98

List of Tables

3.1	Table of equilibrium period data for the AB diblock copolymer melt. . . .	46
3.2	Table of equilibrium period data for the ABA triblock copolymer melt. . . .	46
3.3	Table of equilibrium period data for the BAB triblock copolymer melt. . . .	47

Chapter 1

Introduction

This thesis employs a computational field-theoretic approach to study the chain exchange dynamics between BCC-ordered micelles in AB, ABA and BAB block copolymer melts. This technique, originally developed by Grzetic et al.[1, 2], has a flexibility that allows us to extend its use beyond the homopolymer blend and diblock melts to the systems of interest to this thesis. In particular, we focus on the study of chain exchange dynamics between BCC-ordered spherical domains self-assembled by the segregation of unlike monomer species.

1.1 Theory of Polymers

Polymers consist of elementary chemical repeat units called monomers that are connected by covalent bonds, often to form a long linear chain molecule. Polymers can consist of a large number of these repeat units, typically between 10^3 to 10^4 monomers, and are characterized by the number of monomers N , called the degree of polymerization. For large N , through the covalent bond's rotational degrees of freedom, the molecule gains flexibility and tends to form a coil to maximize the entropy of the polymer. Polymers are ubiquitous in the modern world. They appear in aspects of the biological, industrial and technological worlds. Due to a wide variety of possible polymer architectures, the synthesis of novel polymer structures is crucial in areas such as drug delivery [3, 4].

Polymers possess several universal properties regardless of the type of chemical repeat units that make up the chain, as properties such as the viscosity and chain configuration obey scaling laws that are independent of the monomeric species. Therefore, we can model polymers without being concerned about the specific chemistry. Therefore, a coarse-grained description is possible and appropriate.

For a generic polymer, we can characterize its size, and whether it has a coiled or stretched configuration, by calculating its radius of gyration R_g . By definition, the radius of gyration of a polymer is given by

$$R_g^2 = \frac{1}{N} \sum_{i=1}^N (\mathbf{R}_i - \mathbf{R}_{cm})^2,$$

where \mathbf{R}_i is the position of the i th monomer and \mathbf{R}_{cm} is the polymer's centre of mass. In a melt, a polymer is in an ideal configuration and $R_g^{(0)} = b\sqrt{N/6}$. Examining $R_g/R_g^{(0)}$ can then tell us if a polymer is in a stretched ($R_g/R_g^{(0)} > 1$) or coiled $R_g/R_g^{(0)} \approx 1$ configuration.

Polymers can be formed by many different monomer species. For example, polystyrene (PS) and polyethyl-alt-propylene (PEP) repeat units have been used in experiments relevant to this thesis [5]. In particular, we are interested in polymers that are composed of sections (or blocks) of distinct chemical species that are covalently bonded. These polymers are referred to as block copolymers and have many different architectures. The simplest block copolymer is the diblock copolymer which consists of two blocks of distinct chemical species often referred to as A-type and B-type monomers. We can refer to this copolymer as an AB diblock copolymer. In this thesis, the focus of the work is on the extension of this diblock copolymer to include a third block that is comprised of either A-type or B-type monomers, forming an ABA or BAB triblock copolymer. The three architectures of interest to this work are shown in Figure 1.1

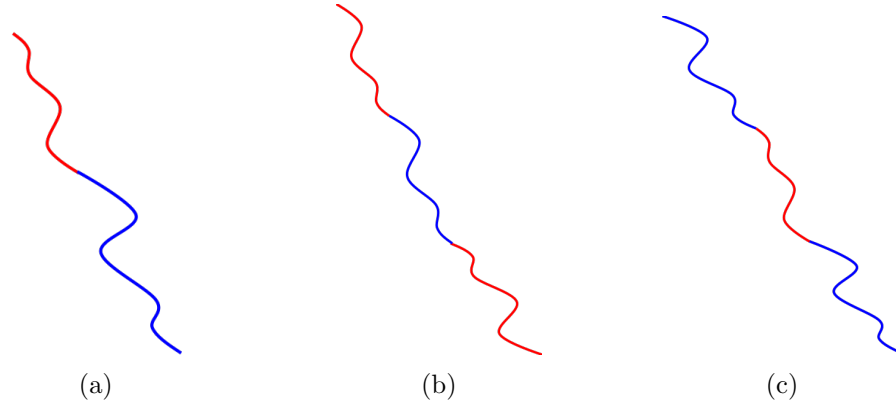


Figure 1.1: Schematic illustration of three chain architectures of block copolymers: a) AB diblock copolymer, b) ABA triblock copolymer and c) BAB triblock copolymer. The red blocks shown in each figure are the core-forming A block, while the blue blocks are the B blocks that form the corona.

Block copolymers exhibit micro-phase separation, where the different monomer species form A- or B-rich domains. This is due to the incompatibility of the two monomeric species. However, due to the aforementioned covalent bond between the two blocks, the two species are unable to completely separate. This property allows us to form a variety of different structures simply by varying the fractional composition of the monomer species on the copolymer as well as the temperature (or interaction strength). The common phases found for diblock as well as triblock copolymers are the lamellar (LAM), cylindrical (HEX), spherical (BCC) and gyroidal (GYR) phases, whose structures are shown in Figure 1.2. The phase behaviour of more complicated block copolymer architectures is continuously being studied. This is an incredibly interesting research topic as more exotic phases, such as the Frank-Kasper phases[6], can be found by changing the chain architecture with more blocks or by mixing copolymers with core blocks of different length[7, 8, 9].

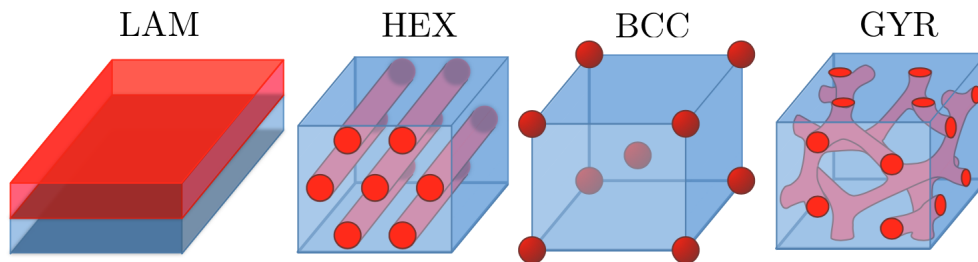


Figure 1.2: Illustration of the phases in which a diblock copolymer melt can self-assemble, such as lamellar (LAM), cylindrical (HEX), spherical (BCC) and gyroidal (GYR) phases. Figure is from Ref. [10].

In this work, we are concerned with the chain exchange of copolymers between BCC-ordered spherical micelles. Figure 1.3 shows an example of a spherical micelle formed by diblock copolymers. The red domain is the micelle core and is formed by high densities of the core-forming A blocks. The blue domain is the corona of the micelle which denotes high densities of the B blocks. In this diagram we can also see the core-corona interface which, for illustration, is very well-defined and represents the average junction point of core and corona blocks.

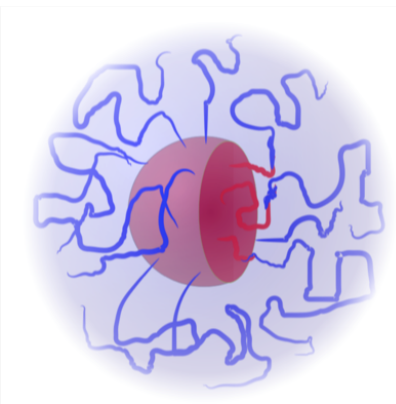


Figure 1.3: Illustrative example of a spherical micelle formed by diblock copolymers. The micelle core, shown in red, is the region formed by the minority A block (or core-forming block). The blue region outside of the core is the micelle corona which is formed by the majority B block, simply referred to as the corona block. Illustration is from Reference [11].

1.2 Exchange Kinetics of Block Copolymers

While the self-assembly of polymeric systems of various chain architectures has been a prominent field of study, there is also interest in the concepts of chain exchange and the dynamics of self-assembly. To form the micro-phases seen in diblock and triblock copolymers, individual chains must exchange, overcoming entropic and enthalpic barriers to enter a favourable energetic state. Once micelles have formed within the system, chains are still able to exchange by core blocks overcoming an enthalpic barrier related to the segregation strength, characterised by the interaction strength ϵ . Experiments studying chain exchange have revealed a variety of factors that affect the chain exchange relaxation time, which is the average time it takes for a chain to exchange between micelles.

1.2.1 Experimental Observations

The kinetics of micelle formation have been studied experimentally for many different systems using a variety of experimental techniques such as size-exclusion chromatography[12, 13], fluorescence[14, 15, 16, 17], sedimentation[18, 19] and more recently time-resolved small-angle neutron scattering (TR-SANS)[5, 20, 21]. Research conducted by the Lodge group using TR-SANS has revealed many insights into the kinetics of chain exchange such as the hypersensitivity of chain exchange rate with respect to a polymers core block length[21, 20]. More recently, their work on triblock copolymers has shown a previously unpredicted significant dependence of chain exchange rate on corona block length[5].

TR-SANS can be used to study chain exchange through the use of contrast matching. A mixture of hydrogenated and perdeuterated squalane is designed and used to match the contrast of a 50/50 mixed micelle core composed of hydrogenated and deuterated core blocks. In particular, these experiments form micelle solutions of PS-PEP-PS (ABA) and PEP-PS-PEP (BAB) triblock copolymers where PS and PEP refer to polystyrene and polyethylene-*alt*-propylene, respectively. When the micelle cores are not mixed (pure hPS and dPS cores)

the mixture has maximum scattering contrast, which then decays to zero as the copolymers equilibrate and reach a state of 50/50 mixed cores.

The extent of chain mixing is then described by the relaxation function $R(t)$ which is defined by the relative changes in the dPS concentration in the micelles:

$$R(t) = \left(\frac{I(t) - I(\infty)}{I(0) - I(\infty)} \right)^{1/2}, \quad (1.1)$$

where $I(t)$ is the scattered intensity, integrated over q , recorded at time t . In these experiments, each triblock copolymer architecture is compared to a curve fit of the relaxation function $R(t)$ for an analogous PS-PEP diblock copolymer for each triblock architecture as shown in Figure 1.4.

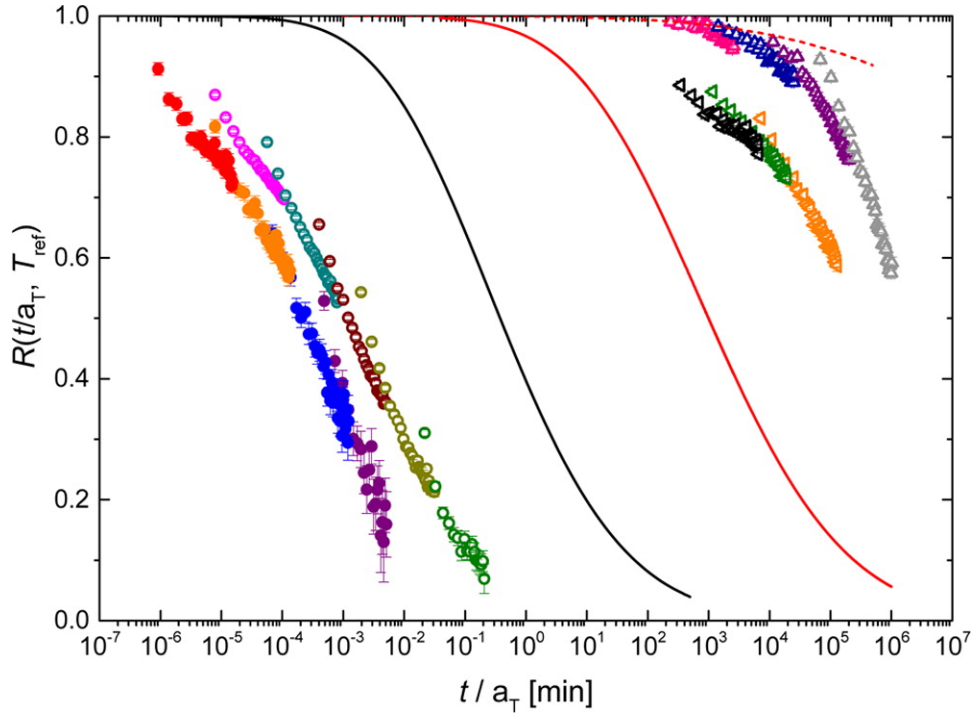


Figure 1.4: $R(t)$ master curves (or $R(t/a_T, T_{ref})$ vs t/a_T curves) of four triblock micelles (left to right: 1 vol % PEP-PS-PEP, 6 vol % PEP-PS-PEP, 0.25 vol % PS-PEP-PS, and 0.5 vol % PS-PEP-PS) and comparison to the diblock exchange model. The black line and red line are model fits of 1 vol % PS-PEP-1 and 1 vol % PS-PEP-2, respectively. The red dashed line is generated by the model assuming the two PS blocks in PS-PEP-PS extract independently. This figure is from Ref. [5]

The curves in Figure 1.4 allow us to make some general conclusions about the dependence

of chain exchange on architecture. The decrease in the speed of chain exchange for the PS-PEP-PS triblocks is expected as there is an additional core block for each triblock. The extra core block being required to extract from the micelle core should introduce a rate-limiting step in the chain exchange, leading to a decrease as seen. However, the large increase in the rate of chain exchange for the PEP-PS-PEP triblocks, relative to the corresponding PS-PEP-1 diblock, is a surprising result. Current theories [22, 20] describing relaxation kinetics of chain exchange only predict a dependence on core block length:

$$\tau(N) = \tau_R(N) \exp(E_a(N)/k_B T), \quad (1.2)$$

where E_a is the enthalpic penalty for exposing a core block to the corona of the micelle and $\tau_R(N)$ is the Rouse time for a polymer of length N . According to the results of Reference [5], the form of this energetic penalty can be expressed as $\frac{E_a}{k_B T} = \alpha \chi N_{core}$ where χ is the Flory-Huggins interaction parameter, and α is some $\mathcal{O}(1)$ constant. Previous work suggests that if the core block assumes a collapsed conformation of the PS block once it has been expelled from the core, then E_a scales as the surface energy of the micelle core $E_a \sim N^{2/3}$ [22].

Reference [5] provides possible mechanism for triblock chain exchange between micelles for both PEP-PS-PEP (BAB) and PS-PEP-PS (ABA) copolymers. Figure 1.5 shows the mechanisms for chain exchange between spherical micelles. For PEP-PS-PEP, the proposed mechanism only contains the steps of chain expulsion from a micelle core and insertion into a second core. However, there is an additional step for the PS-PEP-PS polymer as the second core block must be extracted from the core as well.

It is important to note here that these experiments are performed in a selective solvent, in this case squalane, whereas our simulations later in this work are performed in a melt. It is expected that some, if not all, architecture effects observed in this work should be carried over to the case of a triblock copolymer melt.

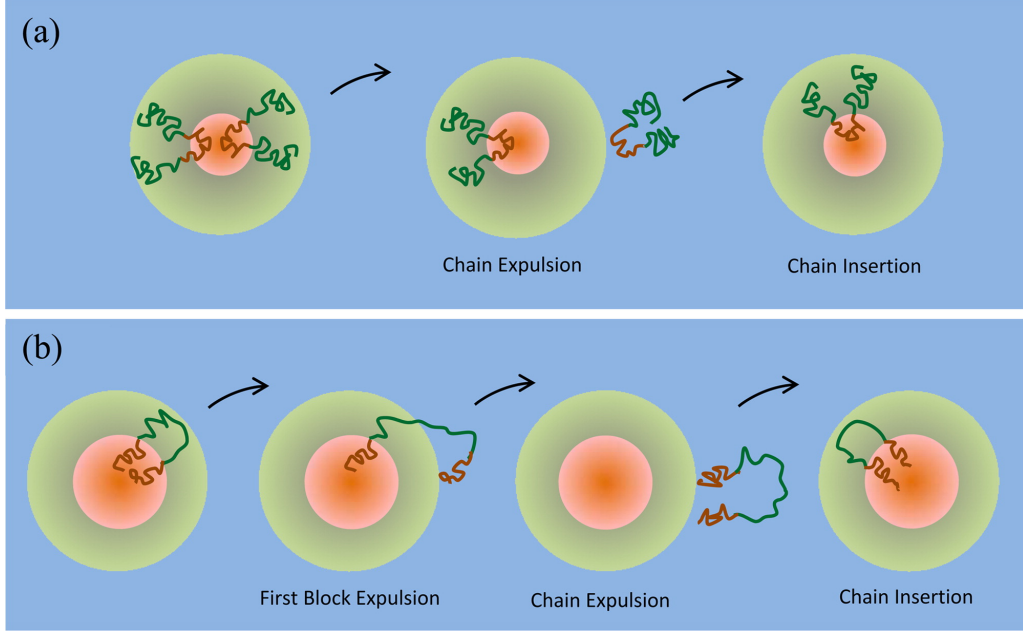


Figure 1.5: Schematic illustration of the process of chain exchange for two triblock architectures: (a) PEP-PS-PEP (BAB) triblocks and (b) PS-PEP-PS (ABA) triblocks. The relative micelle core sizes were determined by small-angle x-ray scattering experiments (SAXS). This figure is from Ref. [5].

1.2.2 Theoretical Methods

The study of polymeric systems theoretically has been dominated by the equilibrium self-consistent mean-field theory (SCFT), which has been used to identify the phase behaviour of copolymer architectures such as AB, ABA and BAB block copolymers [23, 24, 25]. However, this theory is an equilibrium theory, and it cannot address the dynamical problem of chain exchange. Multiple other computational techniques have been used to study polymer dynamics such as Monte Carlo (MC) [26, 27], dissipative particle dynamics (DPD) [28, 29, 30, 31], and single-chain mean-field (SCMF) simulations [32]. Here we present a brief discussion on some of these computational methods used to study polymer dynamics.

Monte Carlo methods are a broad class of simulation technique in which polymer dynamics are simulated by randomly generating configurations according to a defined set of rules such that generated chain configurations satisfy the chosen probability distribution. The MC algorithm then consists of using Boltzmann weighting to accept or reject new configurations.

Müller and Daoulas [26] employed different algorithms to reproduce Rouse dynamics as well as entangled polymer dynamics. Furthermore, Haliloglu and Mattice [27, 33] have used a simple Monte Carlo model to study the exchange rate of chains between micelles of diblock copolymers in a dilute solution as well as the mechanisms of chain exchange between micelles at dynamic equilibrium. Their results suggest that as the concentration of free chains, or unimers, decreases the chain exchange rate also decreases. They also note that the decrease in the unimer concentration also corresponds to an increase in the average aggregate size, establishing a connection between the chain exchange rate and micelle size.

Dissipative particle dynamics (DPD) has become a common method for simulating polymer dynamics. DPD[34, 35] combines aspects of the popular atomistic simulation techniques of Molecular Dynamics (MD) and Brownian Dynamics (BD) to produce a simulation technique that evolves according to dissipative and random forces while also being able to incorporate hydrodynamic effects, i.e. the system obeys the Navier-Stokes equation in long-time limit. The repulsive forces between particles in this method are often artificially soft repulsions which can lead to high fluid phase compressibility, loss of topological constraints and extremely high fluctuation effects [36].

DPD simulations have been used extensively in the literature to study the exchange rate of chains between micelles of diblock copolymers in dilute solutions. Polymer melts have not been as extensively studied, however DPD has been used to simulate a homopolymer melt which recovers predicted scaling laws for the homopolymer's end-to-end distance R , Rouse time τ_R and diffusion coefficient D as a function of chain length N [31]. Most simulation studies using DPD relevant to chain exchange kinetics have been limited to diblock copolymers in a dilute solution and are focused on describing the mechanisms involved in chain exchange.

References [29] and [30] established that DPD can be used to efficiently study the equilibrium properties, kinetics of micellization and chain exchange dynamics of diblock copolymer micelle solutions. The results of these simulations found that chain exchange is dominated

by the expulsion of single chains or small aggregates which is a first-order kinetic process characterized by a relaxation time τ that scales exponentially according to $\tau \sim \exp(0.67\chi N_A)$ where N_A is the length of the core-forming A block. Furthermore, these simulations found that chain exchange between micelles occurs via several kinetic mechanisms including unimer expulsion/insertion, small aggregate fragmentation/merging and micelle fusion/fission. For all polymer concentrations studied, unimer expulsion/insertion was found to be the dominant mechanism for chain exchange. However, the contribution of micelle fusion/fission to chain exchange increases as the polymer concentration increases while the contribution from unimer expulsion/insertion and small aggregate fragmentation/merging decreased. A surprising result from Reference [29] is that diblock chains with a longer corona block are found to exchange between micelles more rapidly as this increases the critical micelle concentration and decreases the micelle size implying that the potential barrier for chain expulsion is lower for chains with longer corona blocks.

Following the results found experimentally in Reference [5], DPD simulations [28] were performed comparing the equilibrium chain exchange rate of AB diblock solutions to symmetric and asymmetric BAB triblock solutions. It was found that both symmetric and asymmetric BAB triblocks exchange roughly 1 order of magnitude faster than diblocks in the same solvent. This result is previously unexplained by theory and is suggested to be caused by an increase in the density of corona beads near the micelle interface, resulting in larger stretching penalties and lower aggregation numbers (and therefore micelle size), as well as the looped core block spending more time near the micelle interface, resulting in a lower energy barrier between the core-corona interface.

While the above dynamical simulation methods are all viable techniques for studying the dynamics of chain exchange, dSCFT allows us to simulate large length-scales as well as long time-scales and makes use of more realistic interaction potentials than the soft core potentials used in DPD simulations, for example. As well, we have chosen to use dSCFT for our study as it is a dynamical analogue to the successful equilibrium SCFT.

1.3 Polymer Dynamics Theories

1.3.1 The Rouse Model

The Rouse model [37] was the first successful model describing the dynamics of polymers. Each chain in the model consists of N coarse-grained beads (not to be confused with physical monomers) which are connected by springs of average length b . These beads represent statistical segments of a physical polymer that do not (in our treatment for flexible chains) exhibit correlations in their orientation relative to other segments. Each bead has a friction coefficient ζ . The total friction experienced by a Rouse chain is the total contribution from each of the N beads $\zeta_R = N\zeta$. Then using the Einstein relation we can obtain the diffusion coefficient of the centre-of-mass of a Rouse chain:

$$D_0 = \frac{k_B T}{\zeta_R} = \frac{k_B T}{N\zeta}. \quad (1.3)$$

From the diffusion coefficient, the characteristic time for a chain to diffuse a distance on the order of its size R_g is given by the following relationship:

$$\tau_R \sim \frac{R_g^2}{D_0} \sim \frac{\zeta b^2}{k_B T} N^2 \sim \tau_0 N^2, \quad (1.4)$$

where $\tau_0 = \frac{\zeta b^2}{3\pi^2 k_B T}$ is the time scale for motion of individual beads on the chain. This characteristic time τ_R is referred to as the Rouse time and in this thesis is defined as $\tau_R \equiv \frac{\zeta b^2}{3\pi^2 k_B T} N^2$ and has significance to the dynamics of polymers. At time scales shorter than this characteristic time, but greater than the time scale for motion of individual beads τ_0 , the chain exhibits viscoelastic modes. For time scales larger than τ_R the chain motion is diffusive.

The viscoelastic modes that are observed within the intermediate regime of $\tau_0 < t < \tau_R$ are referred to as Rouse modes. These modes correspond to the relaxation on the scale of different length chain sections. Therefore, the p th mode corresponds to relaxation on the

scale of chain sections which contain N/p beads. The relaxation time associated with the p th mode is given by

$$\tau_p \approx \tau_0 \left(\frac{N}{p} \right)^2. \quad (1.5)$$

This can be thought of breaking the Rouse chain into p sections which relax independently with a relaxation time τ_p . During this relaxation time, chain sections containing N/p monomers will move a distance on the order of their size. From this we can write the mean-square displacement of the monomers in these chain sections as

$$\langle (\mathbf{R}_n(\tau_p) - \mathbf{R}_n(0))^2 \rangle \approx b^2 \frac{N}{p} \approx b^2 \left(\frac{\tau_p}{\tau_0} \right)^{1/2}, \quad (1.6)$$

where $\mathbf{R}_n(t)$ is the position vector of monomer n at a time t . From Equation (1.6) it is clear that we do not observe diffusive motion of individual beads, as the mean-square displacement is not linear in t , rather it increases as time to the one-half power for these intermediate time-scales:

$$\langle (\mathbf{R}_n(t) - \mathbf{R}_n(0))^2 \rangle \approx b^2 \left(\frac{t}{\tau_0} \right)^{1/2}. \quad (1.7)$$

1.3.2 Kramer's Transition State Theory

The main focus of this thesis is that of the chain exchange kinetics of block copolymers between spherical micelles. For chain exchange to occur, core monomers must expose themselves to the surrounding corona of the micelle. As the interaction between core and corona monomers is unfavourable, the system must pay an enthalpic penalty in order for a core monomer, and on a larger scale the entire core block, to be removed from the core and move into the corona. This problem is essentially that of Kramers problem of a particle trapped within a potential well [38], except now the "particle" is now the core block, but an extended object.

The original problem statement presented by Kramers has a particle moving within an external field of force while also experiencing Brownian forces due to a surrounding medium in thermodynamic equilibrium. Within the context of polymer chain exchange, the particle concerned is a core block and the potential well is a barrier formed by the enthalpic penalty for moving one species inside the micelle core consisting of monomers of the same species to the corona of the micelle which consists of monomers of a different species that have an unfavourable interaction with the core monomers. Similar to the particles in the original problem, our treatment of a polymer melt includes random Brownian forces whose fluctuations are defined by the fluctuation-dissipation theorem, as discussed in Section 2.1.

The main result presented in Reference [38], relates the “reaction velocity” k to the energetic barrier ΔE that the particle travels over. An overview of the calculation is presented in Appendix B, and it is found for such an activated process that

$$k \approx e^{-\Delta E/(k_B T)}. \quad (1.8)$$

In this work, we are concerned with the characteristic time τ associated with this activated process, which according to Equation (1.8) can be written as

$$\tau \approx e^{\Delta E/(k_B T)}. \quad (1.9)$$

We treat chain exchange in this work as an activated process where the core block has an enthalpic penalty ΔE associated with being exposed to the corona, and this chain exchange has a characteristic relaxation time given by Equation (1.9).

Chapter 2

Dynamical Self-Consistent Field Theory

In this chapter, we provide the reader with a background to the dynamical self-consistent field theory (dSCFT) developed by Grzetic [2] for diblock copolymers and the extension I have made to study the dynamics of chain extraction of AB, ABA and BAB block copolymer chain architectures.

The dynamical self-consistent field theory used in this work was originally developed within our group to simulate the interacting Rouse dynamics of diblock copolymer melts and binary homopolymer blends. The original formulation was made such that the method could be applied for a variety of systems aside from the binary homopolymer blend and diblock copolymer melt. In this work, we apply the theory to ABA and BAB triblock copolymer melts to study the effect of chain architecture on the dynamics of chain exchange in copolymer micelle phases. This theory is suitable for studying the dynamics of chain exchange as we maintain information about single chain dynamics while being able to access the long time-scales necessary to study relaxation. To modify the theory to apply to triblock copolymers, appropriate changes were made to the calculation of the mean density field as well as the application of the mean force field.

2.1 The Microscopic Model

As a starting point, we must construct a microscopic model for the dynamics of our many-body system. As we are concerned with the dynamics of polymeric systems, in particular polymer melts, we use the exactly-solvable, in the absence of interactions, Rouse model as it is a dynamical bead-spring analogue to the ideal chain model.

The model consists of n_P Rouse chains each with degree of polymerization N . We include in the model a non-bonded interaction force, \mathbf{F}_{int} , that acts between all pairs of beads in the system. Therefore we can mathematically describe this system with a set of coupled Langevin equations that describe the time evolution of the position $\mathbf{R}_n^{(l)}(t)$ of each bead in the system, where $n = 1, \dots, N$ and $l = 1, \dots, n_P$ are the bead and chain labels respectively:

$$\zeta \frac{d\mathbf{R}_n^{(l)}(t)}{dt} = \mathbf{F}_{spr,n}^{(l)} + \sum_{l',n'} \mathbf{F}_{int}(\mathbf{R}_n^{(l)}, \mathbf{R}_{n'}^{(l')}) + \mathbf{f}_n^{(l)}. \quad (2.1)$$

Each bead in the system experiences a drag force which is quantified by the monomeric friction coefficient ζ , a spring force $\mathbf{F}_{spr,n}^{(l)}$ which comes from bonds between neighbouring monomers on a chain, the non-bonded interaction force $\mathbf{F}_{int}(\mathbf{R}_n^{(l)}(t), \mathbf{R}_{n'}^{(l')}(t))$ and a random force $\mathbf{f}_n^{(l)}$. It is important to make the distinction here that the beads and spring described by the Rouse model do not represent physical monomers and the covalent bonds between them, rather they are “effective monomers” that model “Kuhn” segments of the polymer. The interaction between these segments behave like springs due to entropy favouring a coiled configuration over a stretched one. We can then describe the spring force as

$$\mathbf{F}_{spr,n}^{(l)}(t) = \frac{3k_B T}{b^2} \left(\mathbf{R}_{n+1}^{(l)}(t) - 2\mathbf{R}_n^{(l)}(t) + \mathbf{R}_{n-1}^{(l)}(t) \right), \quad (2.2)$$

for beads that not located at the ends of the chain. For the end beads the spring force is

$$\mathbf{F}_{spr,1}^{(l)}(t) = \frac{3k_B T}{b^2} \left(\mathbf{R}_2^{(l)}(t) - \mathbf{R}_1^{(l)}(t) \right), \quad (2.3)$$

$$\mathbf{F}_{spr,N}^{(l)}(t) = \frac{3k_B T}{b^2} \left(\mathbf{R}_{N-1}^{(l)}(t) - \mathbf{R}_N^{(l)}(t) \right). \quad (2.4)$$

The statistical segment length b characterizes the length of the “Kuhn” segments and is referred to as the Kuhn length. Due to the large degree of complexity in this theory when considering systems of binary species, we make the simplification that both species have the same Kuhn length $b_A = b_B = b$ and also the same monomeric friction coefficient $\zeta_A = \zeta_B = \zeta$.

The random force in our model is a Gaussian-distributed, zero-mean force that describes the effects of the fast degrees of freedom in our system which have been coarse-grained out. In principle, the random force $\mathbf{f}_n^{(l)}$ can be thought of as a thermostat for the system as the fluctuation-dissipation theorem relates the loss of kinetic energy through the drag force, to Brownian motion fluctuations which add energy to the system to maintain the temperature. For our system to relax to thermodynamic equilibrium after long times for a constant temperature T , the random force \mathbf{f}_n^l must satisfy

$$\langle f_{\alpha,n}^{(l)}(t) \rangle = 0, \quad (2.5)$$

$$\langle f_{\alpha,n}^{(l)}(t) f_{\alpha',n'}^{(l')}(t') \rangle = 2\zeta k_B T \delta_{\alpha\alpha'} \delta_{ll'} \delta_{nn'} \delta(t - t'), \quad (2.6)$$

where α labels the component of the force.

The last component of our microscopic model is the non-bonded interaction force. It is not required to specify a form of this interaction force field in the formulation of our dynamical self-consistent field theory, however in order to simulate this system we must choose an appropriate form. Systems of block copolymers have been observed to micro-phase separate and, as such, two important interactions should be considered. We require a short-range repulsive interaction so that beads do not overlap, enforcing our system to be incompressible. In phase separation, like monomers are grouped together so we also include a slightly longer-range attractive interaction for the interaction potential for like species. In order to model these two interactions, the popular choice of potential is the Lennard-Jones potential

$$V_{LJ}(r) = 4\epsilon \left[\left(\frac{\sigma}{r} \right)^{12} - \left(\frac{\sigma}{r} \right)^6 \right], \quad (2.7)$$

where ϵ specifies the depth of the attractive well and σ sets the range of the interaction. This potential, however, diverges as the distance between two beads in our system approaches zero. In our coarse-grained model, we discretize space in order to compute the force between beads of species α and β , $\mathbf{F}_{LJ}^{(\alpha\beta)}(\mathbf{r}) = -\nabla V_{LJ}^{(\alpha\beta)}(\mathbf{r})$. We regularize the interaction potential by shifting the potential by the term r_0 ,

$$V_{LJ}^{(\alpha\alpha)}(r) = 4\epsilon \left[\left(\frac{\sigma}{r+r_0} \right)^{12} - \left(\frac{\sigma}{r+r_0} \right)^6 \right]. \quad (2.8)$$

This renders the interaction potential, and the interaction force, finite, which is important for later calculations.

For unlike species of monomers, we want to have a purely repulsive interaction, so we model this interaction using the regularized version of the Weeks-Chandler-Andersen (WCA) Lennard-Jones potential

$$V_{WCA}^{(AB)}(r) = \begin{cases} 4\epsilon \left[\left(\frac{\sigma}{r+r_0} \right)^{12} - \left(\frac{\sigma}{r+r_0} \right)^6 + \frac{1}{4} \right], & r+r_0 \leq 2^{1/6}\sigma \\ 0, & r+r_0 > 2^{1/6}\sigma. \end{cases} \quad (2.9)$$

In general, these interaction potentials need to be characterized by their interaction strength ϵ which should depend on the species involved in the interaction. However, we can simplify our theory by using the same ϵ for all interactions which is sufficient to drive phase-separation of A- and B-type monomers. Murat et al. [39] have also shown that it is possible to observe phase separation of AB diblock copolymers in a melt using only the purely repulsive WCA potential with the condition that $\epsilon_{AB} > \frac{1}{2}(\epsilon_{AA} + \epsilon_{BB})$.

2.2 Dynamical Mean-Field Approximation

The microscopic model in the previous section outlines a many-chain interacting problem which in principle can be used to perform Brownian motion simulations. However, we are interested in applying a technique analogous to the successful equilibrium self-consistent field theory (SCFT) to our dynamical model. This dynamical self-consistent field theory (dSCFT) has been described in detail by Grzetic [1, 2, 10], therefore this thesis will only outline the formulation as well as the changes I made to apply the theory to triblock copolymers. The formulation presented in this section outlines the equations associated with a general triblock copolymer melt which can describe either the ABA or BAB architecture depending on the definition of the σ_n function, defined later, that is applied to the equations. For the BAB architecture, we introduce a set of monomer fraction parameters f_{B1}, f_A and f_{B2} to describe the fraction of the total monomers on each chain which resides in each block of the copolymer. We can similarly define a set of monomer fraction parameters f_{A1}, f_B and f_{A2} when using the ABA architecture. As these parameters are fractions, their sum must equal 1 for either architecture:

$$f_{B1} + f_A + f_{B2} = 1, \quad (2.10)$$

$$f_{A1} + f_B + f_{A2} = 1. \quad (2.11)$$

From the above equations we note that a symmetric copolymer architecture is defined by $f_{B1} = f_{B2}$ for BAB and by $f_{A1} = f_{A2}$ for ABA. The symmetric triblock architecture is the only situation we study.

Similar to the equilibrium SCFT, we start by constructing a dynamical partition function $Z(t|t_0)$ containing the appropriate statistical information from our model. To construct this partition function, we write out the functional integral $Z(t|t_0)$ over the space-time trajectories of all chains that satisfy the coupled Langevin equations given by Equation (2.1) with

$$\sum_{l',n'} \mathbf{F}_{int}(\mathbf{R}_n^{(l)}(t), \mathbf{R}_{n'}^{(l')}(t)) = \sum_{l'=1}^{n_P} \sum_{n'=1}^N \left[\sigma_n \sigma_{n'} \mathbf{F}_{int}^{(AA)}(\mathbf{R}_n^{(l)}(t), \mathbf{R}_{n'}^{(l')}(t)) + \sigma_n (1 - \sigma_{n'}) \mathbf{F}_{int}^{(AB)}(\mathbf{R}_n^{(l)}(t), \mathbf{R}_{n'}^{(l')}(t)) \right. \\ \left. + (1 - \sigma_n) \sigma_{n'} \mathbf{F}_{int}^{(BA)}(\mathbf{R}_n^{(l)}(t), \mathbf{R}_{n'}^{(l')}(t)) + (1 - \sigma_n)(1 - \sigma_{n'}) \mathbf{F}_{int}^{(BB)}(\mathbf{R}_n^{(l)}(t), \mathbf{R}_{n'}^{(l')}(t)) \right], \quad (2.12)$$

where σ_n depends on the polymer architecture and is defined as equal to 1 for beads in the A-block and 0 for beads in the B-block. Therefore, for a BAB copolymer, σ_n can be written as

$$\sigma_n = \begin{cases} 0, & 1 \leq n \leq f_{B1}N \\ 1, & f_{B1}N < n \leq (f_{B1} + f_A)N \\ 0, & (f_{B1} + f_A)N < n \leq N. \end{cases} \quad (2.13)$$

Similarly for an ABA copolymer architecture, σ_n is defined by

$$\sigma_n = \begin{cases} 1, & 1 \leq n \leq f_{A1}N \\ 0, & f_{A1}N < n \leq (f_{A1} + f_B)N \\ 1, & (f_{A1} + f_B)N < n \leq N. \end{cases} \quad (2.14)$$

The functional integral over all space-time trajectories that satisfy Equation (2.1) then is written as

$$Z(t|t_0) = \int \prod_l \left(\prod_n \{d\mathbf{R}_n^{(l)}(t_0)\} P_0(\{\mathbf{R}_n^{(l)}(t_0)\}, t_0) \right) \int \prod_{l,n} \left\{ D[\mathbf{R}_n^{(l)}(t')] \right. \\ \left. \times \delta \left[\frac{d\mathbf{R}_n^{(l)}(t')}{dt} - \frac{1}{\zeta} \mathbf{F}_{spr,n}^{(l)}(t') - \frac{1}{\zeta} \sum_{l',n'} \mathbf{F}_{int}(\mathbf{R}_n^{(l)}(t'), \mathbf{R}_{n'}^{(l')}(t')) - \frac{1}{\zeta} \mathbf{f}_n^{(l)}(t') \right] \right\}. \quad (2.15)$$

The delta function can then be transformed by invoking the Fourier-transform representation

$$\begin{aligned}
& \delta \left[\frac{d\mathbf{R}_n^{(l)}(t')}{dt} - \frac{1}{\zeta} \mathbf{F}_{spr,n}^{(l)}(t') - \frac{1}{\zeta} \sum_{l',n'} \mathbf{F}_{int}(\mathbf{R}_n^{(l)}(t'), \mathbf{R}_{n'}^{(l')}(t')) - \frac{1}{\zeta} \mathbf{f}_n^{(l)}(t') \right] \\
&= \int d\hat{\mathbf{R}}_n^{(l)}(t') \exp \left[i\hat{\mathbf{R}}_n^{(l)}(t') \cdot \left(\frac{d\mathbf{R}_n^{(l)}(t')}{dt} - \frac{1}{\zeta} \mathbf{F}_{spr,n}^{(l)}(t') \right. \right. \\
&\quad \left. \left. - \frac{1}{\zeta} \sum_{l',n'} \mathbf{F}_{int}(\mathbf{R}_n^{(l)}(t'), \mathbf{R}_{n'}^{(l')}(t')) - \frac{1}{\zeta} \mathbf{f}_n^{(l)}(t') \right) \right], \quad (2.16)
\end{aligned}$$

which then gives

$$\begin{aligned}
Z(t|t_0) &= \int \prod_l \left(\prod_n \{d\mathbf{R}_n^{(l)}(t_0)\} P_0(\{\mathbf{R}_n^{(l)}(t_0)\}, t_0) \right) \int \prod_{l,n} \left\{ D[\mathbf{R}_n^{(l)}(t')] D[\hat{\mathbf{R}}_n^{(l)}(t')] \right\} \\
&\quad \times \exp \left[\sum_{l,n} \int_{t_0}^t dt' i\hat{\mathbf{R}}_n^{(l)}(t') \cdot \left(\frac{d\mathbf{R}_n^{(l)}(t')}{dt} - \frac{1}{\zeta} \mathbf{F}_{spr,n}^{(l)}(t') \right. \right. \\
&\quad \left. \left. - \frac{1}{\zeta} \sum_{l',n'} \mathbf{F}_{int}(\mathbf{R}_n^{(l)}(t'), \mathbf{R}_{n'}^{(l')}(t')) - \frac{1}{\zeta} \mathbf{f}_n^{(l)}(t') \right) \right]. \quad (2.17)
\end{aligned}$$

This dynamical partition function can then be expressed in terms of collective fields that are relevant to physical properties of interest. In particular, we are interested in examining the bead density fields ρ_A and ρ_B as well the force fields $\boldsymbol{\psi}_A$ and $\boldsymbol{\psi}_B$ which evolve our system. Using exact transformations, we can rewrite the dynamical partition function in terms of the microscopic bead density operators

$$\hat{\rho}_A(\mathbf{r}, t) = \sum_{l=1}^{n_P} \sum_{n=1}^N \sigma_n \delta(\mathbf{r} - \mathbf{R}_n^{(l)}(t)), \quad (2.18)$$

$$\hat{\rho}_B(\mathbf{r}, t) = \sum_{l=1}^{n_P} \sum_{n=1}^N (1 - \sigma_n) \delta(\mathbf{r} - \mathbf{R}_n^{(l)}(t)) \quad (2.19)$$

and their corresponding vector response operators

$$\hat{\phi}_A(\mathbf{r}, t) = \sum_{l=1}^{n_P} \sum_{n=1}^N \sigma_n \hat{\mathbf{R}}_n^{(l)}(t) \delta(\mathbf{r} - \mathbf{R}_n^{(l)}(t)), \quad (2.20)$$

$$\hat{\phi}_B(\mathbf{r}, t) = \sum_{l=1}^{n_P} \sum_{n=1}^N (1 - \sigma_n) \hat{\mathbf{R}}_n^{(l)}(t) \delta(\mathbf{r} - \mathbf{R}_n^{(l)}(t)). \quad (2.21)$$

We can use these definitions to rewrite the following term in $Z(t|t_0)$:

$$\begin{aligned} & \sum_{l,n} \int_{t_0}^t dt' i \hat{\mathbf{R}}_n^{(l)}(t') \cdot \sum_{l',n'} \mathbf{F}_{int}(\mathbf{R}_n^{(l)}(t'), \mathbf{R}_{n'}^{(l')}(t')) \\ &= i \int d\mathbf{r} \int_{t_0}^t dt' \left\{ \hat{\phi}_A(\mathbf{r}, t') \cdot \sum_{l',n'} \left[\sigma_{n'} \mathbf{F}_{int}^{(AA)}(\mathbf{r}, \mathbf{R}_{n'}^{(l')}(t')) + (1 - \sigma_{n'}) \mathbf{F}_{int}^{(AB)}(\mathbf{r}, \mathbf{R}_{n'}^{(l')}(t')) \right] \right. \\ & \quad \left. + \hat{\phi}_B(\mathbf{r}, t') \cdot \sum_{l',n'} \left[\sigma_{n'} \mathbf{F}_{int}^{(BA)}(\mathbf{r}, \mathbf{R}_{n'}^{(l')}(t')) + (1 - \sigma_{n'}) \mathbf{F}_{int}^{(BB)}(\mathbf{r}, \mathbf{R}_{n'}^{(l')}(t')) \right] \right\} \\ &= i \int d\mathbf{r} \int_{t_0}^t dt' \left\{ \hat{\phi}_A(\mathbf{r}, t') \cdot \int d\mathbf{r}' \left[\mathbf{F}_{int}^{(AA)}(\mathbf{r}, \mathbf{r}') \hat{\rho}_A(\mathbf{r}', t') + \mathbf{F}_{int}^{(AB)}(\mathbf{r}, \mathbf{r}') \hat{\rho}_B(\mathbf{r}', t') \right] \right. \\ & \quad \left. + \hat{\phi}_B(\mathbf{r}, t') \cdot \int d\mathbf{r}' \left[\mathbf{F}_{int}^{(BA)}(\mathbf{r}, \mathbf{r}') \hat{\rho}_A(\mathbf{r}', t') + \mathbf{F}_{int}^{(BB)}(\mathbf{r}, \mathbf{r}') \hat{\rho}_B(\mathbf{r}', t') \right] \right\}. \end{aligned} \quad (2.22)$$

We have now introduced four microscopic collective field variables in $Z(t|t_0)$. We use the standard field theory technique of projection by insertion of a delta function into the functional integral to relate the microscopic collective fields to the coarse-grained collective field variables $\rho_\alpha(\mathbf{r}, t)$ and $\phi_\alpha(\mathbf{r}, t)$:

$$1 = \int D[\rho_\alpha] \delta[\rho_\alpha - \hat{\rho}_\alpha] \quad (2.23)$$

and

$$1 = \int D[\phi_\alpha] \delta[\phi_\alpha - \hat{\phi}_\alpha], \quad (2.24)$$

where α is the bead species and the functional integrals are over space and time. We invoke

the Fourier-transform representation of the delta functional, introducing the conjugate fields ω_α and ψ_α ,

$$\int D[\rho_\alpha] \delta[\rho_\alpha - \hat{\rho}_\alpha] = \int D[\rho_\alpha] D[\omega_\alpha] \exp \left[\int d\mathbf{r} \int_{t_0}^t dt' i\omega_\alpha(\mathbf{r}, t') (\rho_\alpha(\mathbf{r}, t') - \hat{\rho}_\alpha(\mathbf{r}, t')) \right] \quad (2.25)$$

and

$$\int D[\phi_\alpha] \delta[\phi_\alpha - \hat{\phi}_\alpha] = \int D[\phi_\alpha] D[\psi_\alpha] \exp \left[\int d\mathbf{r} \int_{t_0}^t dt' i\psi_\alpha(\mathbf{r}, t') (\phi_\alpha(\mathbf{r}, t') - \hat{\phi}_\alpha(\mathbf{r}, t')) \right]. \quad (2.26)$$

$Z(t|t_0)$ is then written as a functional integral over these dynamical coarse-grained collective field variables,

$$Z(t|t_0) = \int D[\rho_A] D[\rho_B] D[\omega_A] D[\omega_B] D[\psi_A] D[\psi_B] D[\phi_A] D[\phi_B] e^{-L[\rho_A, \rho_B, \omega_A, \omega_B, \psi_A, \psi_B, \phi_A, \phi_B]}, \quad (2.27)$$

where L is the effective action and has the form

$$\begin{aligned} L = & i \int d\mathbf{r} \int_{t_0}^t dt' \left[\frac{1}{\zeta} \phi_A(\mathbf{r}, t') \cdot \int d\mathbf{r}' \left[\mathbf{F}_{int}^{(AA)}(\mathbf{r}, \mathbf{r}') \rho_A(\mathbf{r}', t') + \mathbf{F}_{int}^{(AB)}(\mathbf{r}, \mathbf{r}') \rho_B(\mathbf{r}', t') \right] \right. \\ & + \frac{1}{\zeta} \phi_B(\mathbf{r}, t') \cdot \int d\mathbf{r}' \left[\mathbf{F}_{int}^{(BB)}(\mathbf{r}, \mathbf{r}') \rho_B(\mathbf{r}', t') + \mathbf{F}_{int}^{(BA)}(\mathbf{r}, \mathbf{r}') \rho_A(\mathbf{r}', t') \right] \\ & - \phi_A(\mathbf{r}, t') \cdot \psi_A(\mathbf{r}, t') - \phi_B(\mathbf{r}, t') \cdot \psi_B(\mathbf{r}, t') - \omega_A(\mathbf{r}, t') \rho_A(\mathbf{r}, t') - \omega_B(\mathbf{r}, t') \rho_B(\mathbf{r}, t') \Big] \\ & - n_P \ln Q([\omega_A, \psi_A, \omega_B, \psi_B], t). \end{aligned} \quad (2.28)$$

In Equation (2.28) the quantity $Q([\omega_A, \psi_A, \omega_B, \psi_B], t)$ is the exact dynamical partition function for a single chain under the influence of the fields $\omega_A(\mathbf{r}, t)$, $\psi_A(\mathbf{r}, t)$, $\omega_B(\mathbf{r}, t)$ and $\psi_B(\mathbf{r}, t)$. This partition function can be related to the probability of finding a chain in a configuration $\{\mathbf{r}_n\}$ at a time t , which is given by the single-chain configuration propagator $q(\{\mathbf{r}_n\}, t)$. Furthermore, we can define the single-chain configuration propagator in terms of the bead propagator $q_n(\mathbf{r}, t)$ which gives the probability of finding the n th bead at a position

\mathbf{r} at time t . Then the dynamical single-chain partition function is defined as

$$\mathcal{Q}([\omega_A, \boldsymbol{\psi}_A, \omega_B, \boldsymbol{\psi}_B], t) = \int \prod_n d\{\mathbf{r}_n\} q(\{\mathbf{r}_n\}, t) = \int d\mathbf{r} q_n(\mathbf{r}, t). \quad (2.29)$$

It is important to note that the single-chain configuration propagator and the bead propagator are conditional probability distributions in that they depend on the initial conditions we impose on the distribution of chain configurations.

Previous work in our group by Grzetic [10] has shown that the single-chain propagator satisfies a modified Smoluchowski equation:

$$\begin{aligned} \frac{\partial q(\{\mathbf{r}_n\}, t)}{\partial t} = & \frac{k_B T}{\zeta} \sum_n \nabla_{\mathbf{r}_n}^2 q(\{\mathbf{r}_n\}, t) - \frac{1}{\zeta} \sum_n \nabla_{\mathbf{r}_n} \cdot \left\{ \left[\mathbf{F}_{spr,n}(t) + \sigma_n \boldsymbol{\psi}_A(\mathbf{r}_n, t) + (1 - \sigma_n) \right. \right. \\ & \left. \left. \times \boldsymbol{\psi}_B(\mathbf{r}_n, t) \right] q(\{\mathbf{r}_n\}, t) \right\} - i \left[\sum_n \sigma_n \omega_A + (1 - \sigma_n) \omega_B(\mathbf{r}_n, t) \right] q(\{\mathbf{r}_n\}, t), \end{aligned} \quad (2.30)$$

where σ_n corresponds to a specific chain architecture and is defined in Equations (2.13) and (2.14) for BAB and ABA triblock architectures, respectively.

Equation (2.30), despite being a single-chain dynamical treatment, is still an exact formulation of the interacting many-chain problem as the chain now interacts with the fluctuating collective fields $\omega_A(\mathbf{r}, t)$, $\boldsymbol{\psi}_A(\mathbf{r}, t)$, $\omega_B(\mathbf{r}, t)$ and $\boldsymbol{\psi}_B(\mathbf{r}, t)$, which depend on the configuration of the system, instead of interacting directly with the other chains in the ensemble. We now take the saddle-point approximation of all the fluctuating fields such that they take their saddle-point dynamical configurations. Taking the functional derivative of the action $L[\rho_A, \rho_B, \omega_A, \omega_B, \boldsymbol{\psi}_A, \boldsymbol{\psi}_B, \phi_A, \phi_B]$ with respect to all fields and setting the derivatives equal to zero, we find that the fields $\omega_A(\mathbf{r}, t)$, $\phi_A(\mathbf{r}, t)$, $\omega_B(\mathbf{r}, t)$ and $\phi_B(\mathbf{r}, t)$ vanish by causality. Then the remaining fields, as well as the bead propagator satisfy the set of mean-field equations:

$$\rho_A(\mathbf{r}, t) = \frac{n_P}{Q} \sum_n \sigma_n q_{n,A}(\mathbf{r}, t), \quad (2.31)$$

$$\rho_B(\mathbf{r}, t) = \frac{n_P}{Q} \sum_n (1 - \sigma_n) q_{n,B}(\mathbf{r}, t), \quad (2.32)$$

$$\psi_A(\mathbf{r}, t) = \int d\mathbf{r}' \left(\mathbf{F}_{int}^{(AA)}(\mathbf{r}, \mathbf{r}') \rho_A(\mathbf{r}', t) + \mathbf{F}_{int}^{(AB)}(\mathbf{r}, \mathbf{r}') \rho_B(\mathbf{r}', t) \right), \quad (2.33)$$

$$\psi_B(\mathbf{r}, t) = \int d\mathbf{r}' \left(\mathbf{F}_{int}^{(BB)}(\mathbf{r}, \mathbf{r}') \rho_B(\mathbf{r}', t) + \mathbf{F}_{int}^{(BA)}(\mathbf{r}, \mathbf{r}') \rho_A(\mathbf{r}', t) \right). \quad (2.34)$$

Equation (2.30) describing the single-chain dynamics is now simplified to take the form describing the dynamics of a Rouse chain interacting in a self-consistent force-field $\psi(\mathbf{r}, t)$ that acts similarly to an “external” field:

$$\begin{aligned} \frac{\partial q(\{\mathbf{r}_n\}, t)}{\partial t} = & \frac{k_B T}{\zeta} \sum_n \nabla_{\mathbf{r}_n}^2 q(\{\mathbf{r}_n\}, t) - \frac{1}{\zeta} \sum_n \nabla_{\mathbf{r}_n} \cdot \left\{ \left[\mathbf{F}_{spr,n}(t) \right. \right. \\ & \left. \left. + \sigma_n \psi_A(\mathbf{r}_n, t) + (1 - \sigma_n) \psi_B(\mathbf{r}_n, t) \right] q(\{\mathbf{r}_n\}, t) \right\}. \end{aligned} \quad (2.35)$$

The single-chain dynamics described by Equations (2.31) through (2.35) are self-consistent in that the single-chain propagator evolves according to the force-fields $\psi_A(\mathbf{r}, t)$ and $\psi_B(\mathbf{r}, t)$ which are determined by the density fields $\rho_A(\mathbf{r}, t)$ and $\rho_B(\mathbf{r}, t)$, respectively, which are in turn described by the single-chain propagator. This self-consistency can be schematically shown to be a recursive loop which evolves the system in time. It is now important to note that while Equation (2.35) can be, in specific cases, iteratively solved using numerical methods, due to the high-dimensional nature of the chain configuration propagator the equation is too complicated to be solved directly.

We can, however, indirectly access the single-chain configuration propagator through the Langevin simulation of n_r chain replicas interacting with the mean force-field $\psi_n(\mathbf{r}, t)$. Each bead then evolves according to the set of Langevin equations

$$\zeta \frac{d\mathbf{R}_n(t)}{dt} = \mathbf{F}_{spr,n}(t) + \sigma_n \boldsymbol{\psi}_A(\mathbf{R}_n(t), t) + (1 - \sigma_n) \boldsymbol{\psi}_B(\mathbf{R}_n(t), t) + \mathbf{f}_n(t). \quad (2.36)$$

This ensemble is statistically equivalent to Equation (2.35) in the limit of infinite chain replicas. Therefore, the number of chain replicas in our ensemble is a tunable parameter that can be chosen to optimize the accuracy and efficiency of our computational method.

Since we are now using a set of Langevin equations to describe the single-chain dynamics, we must make changes to how we calculate the density mean-field. Effectively, we are replacing the single-chain configuration propagator $q(\{\mathbf{r}_n\}, t)$ with the set of chain replica configurations $\{\mathbf{R}_n^{(k)}\}$. Therefore, we can now calculate the density fields using the equations

$$\rho_A(\mathbf{r}, t) = \frac{n_P}{n_r} \sum_{k=1}^{n_r} \sum_{n=1}^N \sigma_n \delta(\mathbf{r} - \mathbf{R}_n^{(k)}(t)), \quad (2.37)$$

$$\rho_B(\mathbf{r}, t) = \frac{n_P}{n_r} \sum_{k=1}^{n_r} \sum_{n=1}^N (1 - \sigma_n) \delta(\mathbf{r} - \mathbf{R}_n^{(k)}(t)) \quad (2.38)$$

where k is the sum over chain replicas in the system. The leading coefficient n_P/n_r determines the weighting of each replica beads contribution. Similar to the recursive loop that could be used to evolve the single-chain configuration propagator which evolved according to a functional Smoluchowski equation, we can define a recursive loop that describes the time evolution of our chain replica Langevin simulation.

One of the benefits of this model in comparison to other dynamical mean-field theoretic treatments for polymer dynamics, is that this method is rigorously derived from the microscopic model defined in Section 2.1, not using phenomenological arguments. This model also has incredibly versatility as the mean-field treatment allows use to choose the collective fields such that we end up with a completely different mean-field theory. The choice of collective field variables should reflect the properties of the system that are of interest.

2.2.1 Dimensionless Mean-Field Equations for Triblock Copolymers

The mean-field equations presented above are given in a dimensionful form. Since we are using numerical methods to solve the time evolution of these equations, it is beneficial to rewrite them in a dimensionless form. This rescaling means we must choose characteristic scaling factors for length, time, force and energy. The characteristic length scale is chosen to be the Kuhn length b , and we call the time-scale τ and define it as the ratio of the friction coefficient to the spring constant

$$\tau = \frac{\zeta b^2}{3k_B T}. \quad (2.39)$$

Again, using the spring constant, we can define the force-scale by multiplying by the length-scale giving $\frac{3k_B T}{b}$, and multiply by this by the length-scale again to give the energy-scale $3k_B T$. We can now redefine all the quantities in our theory such that they are in their dimensionless form:

$$t \rightarrow \tau t, \mathbf{r} \rightarrow b\mathbf{r}, \psi(\mathbf{r}, t) \rightarrow \frac{3k_B T}{b} \psi(\mathbf{r}, t), \rho(\mathbf{r}, t) \rightarrow \frac{1}{b^3} \rho(\mathbf{r}, t), \epsilon \rightarrow 3k_B T \epsilon. \quad (2.40)$$

Therefore we can rewrite our theory using dimensionless quantities such that each bead evolves according to the follow set of Langevin equations:

$$\frac{d\mathbf{R}_n(t)}{dt} = \mathbf{F}_{spr,n}(t) + \sigma_n \psi_A(\mathbf{R}_n(t), t) + (1 - \sigma_n) \psi_B(\mathbf{R}_n(t), t) + \mathbf{f}_n(t). \quad (2.41)$$

Chapter 3

Simulation Details

In this chapter, we present the details of our numerical simulations. We consider a large parameter space, as our system is described by many variables such as chain degree of polymerization N , interaction strength ϵ and simulation box-size $L_x L_y L_z$. We perform extensive systematic simulations of block copolymer systems to determine the effect of polymer block sequence on chain exchange dynamics. The numerical implementation of the dynamical self-consistent field theory for diblock copolymers was previously outlined [10] and therefore the discussion here will be kept general. Our focus will be on the changes we made to implement the theory for different block sequences of copolymers. This chapter is divided into two parts. The first will describe the aforementioned changes and outline the general set-up of our numerical simulations. The second part discusses the technical details of the systematic studies performed.

3.1 Numerical Method

The numerical implementation of dSCFT is designed to run as a parallel simulation on P processors using the Message Passing Interface (MPI) to provide communication between the processes. The mean fields are calculated at grid points of our $L_x \times L_y \times L_z$ grid. Each processor simulates a subset of the chain ensemble consisting of n_r/P chain replicas. Since

each chain interacts only with the mean force-field we can divide the entire chain ensemble across the P processors to speed-up our simulations. We calculate the contribution of each sub-ensemble to the density field and then pass the contributions to each processor so that the ensembles are evolved properly. We also make use of the parallel nature of the problem to speed-up the calculation of the mean force field. The density field of the full ensemble is sent to each processor then the grid points are divided evenly across P processes into “slices” of the total grid for the calculation of the mean force-field so that each processor is calculating a portion of the force-field using the full ensemble density field. We impose some restrictions on some variables:

- P must be a power of 2 to optimize the communication routines.
- The total number of grid points, $L_x L_y L_z$, must be divisible by the number of processors P as our mean force-field routine requires the grid to be divided into subsections with an equal number of grid points.

Our numerical method involves (i) initializing the system of chain replicas, (ii) calculating and communicating the mean fields across processes, (iii) then evolving the system according to the mean-field Langevin equation using operator splitting. Subroutines for analysis and output are placed in the main time evolution loop either after or before the system is evolved.

3.1.1 Initialization

First, we initialize our systems variables, including physical properties such as chain length N as well as system variables like the dimensions (L_x, L_y, L_z) and the time-step Δt . Memory is also allocated for the various arrays required in our simulations. The initial position of each bead within our simulation is also initialized at this stage such that the chain replicas within the system have a Gaussian chain distribution:

$$P(\{\mathbf{R}_n\}) = \left(\frac{3}{2\pi b^2}\right)^{3N/2} \exp \left[-\sum_{n=1}^N \frac{3(\mathbf{R}_n - \mathbf{R}_{n-1})^2}{2b^2} \right]. \quad (3.1)$$

This is achieved by placing the first bead of each chain randomly within the simulation box and then performing a Gaussian random walk to place the remaining beads on the chain:

$$R_{\alpha,m}^{(l)} = R_{\alpha,m-1}^{(l)} + \frac{b}{\sqrt{3}}\mathcal{N}(0,1), \quad (3.2)$$

where α is the coordinate-axis, m is the bead index, l is the chain label and $\mathcal{N}(0,1)$ is a Gaussian-distributed random number centered at zero with unit variance that is generated using the standard Box-Muller method and the *ran1* random number generator [40]. We also calculate and initialize the mean force-field vertex coefficients as described in Section 3.1.3.

3.1.2 Calculation of the Density Field

For each time-step, the density field $\rho_{\alpha}(\mathbf{r}, t)$ for bead species α is calculated at each grid point in our simulation box so we refer to the density array $\rho_{i,j,k}^{(\alpha)}(t)$ where

$$\rho_{i,j,k}^{(A)}(t) = \frac{n_P}{n_r} \sum_{l=1}^{n_r} \sum_{n=1}^N \sigma_n \delta(\mathbf{r}_{i,j,k} - \mathbf{R}_n^{(l)}(t)), \quad (3.3)$$

$$\rho_{i,j,k}^{(B)}(t) = \frac{n_P}{n_r} \sum_{l=1}^{n_r} \sum_{n=1}^N (1 - \sigma_n) \delta(\mathbf{r}_{i,j,k} - \mathbf{R}_n^{(l)}(t)). \quad (3.4)$$

Equations (3.3) and (3.4) only calculate the density at grid points (i, j, k) within the simulation box, while replica beads evolve off-grid meaning that they may not necessarily lie on a grid point or even inside the simulation box. Therefore, if necessary, the periodic image of a bead is calculated by imposing periodic boundary conditions on the bead, which contributes to the density at the grid point to which it is closest.

3.1.3 Calculation of the Dynamical Mean Force-Field

Similar to the density field, the dynamical mean force-field $\boldsymbol{\psi}(\mathbf{r}, t)$ is also calculated on-grid, so we will refer instead to the mean force array $\boldsymbol{\psi}_{i,j,k}(t)$. The calculation of the mean force

array makes use of our parallel simulation environment by partitioning the grid spatially into P sections each containing $\frac{L_x L_y L_z}{P}$ grid points, where P is the number of processors. Each processor calculates its own sub-array which are then combined to form the total mean force array. At a given grid-point labelled by indices (i, j, k) , the force fields $\psi_{i,j,k}^{(A)}$ and $\psi_{i,j,k}^{(B)}$ are defined by

$$\psi_{i,j,k}^{(A)}(t) = \int d\mathbf{r}' \left(\mathbf{F}_{int}^{(AA)}(\mathbf{r}_{i,j,k}, \mathbf{r}') \rho_A(\mathbf{r}', t) + \mathbf{F}_{int}^{(AB)}(\mathbf{r}_{i,j,k}, \mathbf{r}') \rho_B(\mathbf{r}', t) \right), \quad (3.5)$$

$$\psi_{i,j,k}^{(B)}(t) = \int d\mathbf{r}' \left(\mathbf{F}_{int}^{(BB)}(\mathbf{r}_{i,j,k}, \mathbf{r}') \rho_B(\mathbf{r}', t) + \mathbf{F}_{int}^{(BA)}(\mathbf{r}_{i,j,k}, \mathbf{r}') \rho_A(\mathbf{r}', t) \right). \quad (3.6)$$

Since the density fields $\rho_A(\mathbf{r}', t)$ and $\rho_B(\mathbf{r}', t)$ are also discretized on-grid, therefore we employ a trilinear interpolation scheme to evaluate the density fields at a position $\mathbf{r}' = \mathbf{r}_{i',j',k'} + \Delta\mathbf{r}$, where $\Delta\mathbf{r} = (x_1, x_2, x_3)\Delta$:

$$\begin{aligned} \rho_\alpha(\mathbf{r}_{i',j',k'} + \Delta\mathbf{r}, t) &= \sum_{\sigma_1, \sigma_2, \sigma_3=0}^1 \rho_{i'+\sigma_1, j'+\sigma_2, k'+\sigma_3}^{(\alpha)}(t) f_{\sigma_1}(x_1) f_{\sigma_2}(x_2) f_{\sigma_3}(x_3) \\ &= \sum_{\sigma_1, \sigma_2, \sigma_3=0}^1 \rho_{i'+\sigma_1, j'+\sigma_2, k'+\sigma_3}^{(\alpha)}(t) C_{\sigma_1, \sigma_2, \sigma_3}(\Delta\mathbf{r}), \end{aligned} \quad (3.7)$$

where $f_0(x) = 1 - x$ and $f_1(x) = x$. We note here our use of periodic boundary conditions as the density arrays $\rho_{i'+\sigma_1, j'+\sigma_2, k'+\sigma_3}^{(\alpha)}(t)$ can have indices that are outside the boundaries of the lattice. When this occurs, we apply the modulo operation to the index to enforce periodic boundary conditions. The Equations (3.5) and (3.6) can then be written as

$$\begin{aligned} \psi_{i,j,k}^{(A)}(t) &= \sum_{i',j',k'} \int_{\mathbb{T}^3} d(\Delta\mathbf{r}) \left(\mathbf{F}_{int}^{(AA)}(\mathbf{r}_{i,j,k}, \mathbf{r}_{i',j',k'} + \Delta\mathbf{r}) \rho_A(\mathbf{r}_{i',j',k'} + \Delta\mathbf{r}, t) \right. \\ &\quad \left. + \mathbf{F}_{int}^{(AB)}(\mathbf{r}_{i,j,k}, \mathbf{r}_{i',j',k'} + \Delta\mathbf{r}) \rho_B(\mathbf{r}_{i',j',k'} + \Delta\mathbf{r}, t) \right), \end{aligned} \quad (3.8)$$

$$\begin{aligned} \psi_{i,j,k}^{(B)}(t) = & \sum_{i',j',k'} \int_{\square} d(\Delta \mathbf{r}) \left(\mathbf{F}_{int}^{(BB)}(\mathbf{r}_{i,j,k}, \mathbf{r}_{i',j',k'} + \Delta \mathbf{r}) \rho_B(\mathbf{r}_{i',j',k'} + \Delta \mathbf{r}, t) \right. \\ & \left. + \mathbf{F}_{int}^{(BA)}(\mathbf{r}_{i,j,k}, \mathbf{r}_{i',j',k'} + \Delta \mathbf{r}) \rho_A(\mathbf{r}_{i',j',k'} + \Delta \mathbf{r}, t) \right), \end{aligned} \quad (3.9)$$

where the integrals are over each unit cell (i', j', k') :

$$\int_{\square} d(\Delta \mathbf{r}) = \Delta^3 \int_0^1 dx_1 \int_0^1 dx_2 \int_0^1 dx_3. \quad (3.10)$$

Equations (3.8) and (3.9) contain sums over all grid points (i', j', k') in the simulation box. For grid points that are far from (i, j, k) , the value of the integral is zero. To decrease the computational cost of performing this integral, we truncate the integral to be over the volume of a sphere of radius $3b$ centered at $\mathbf{r}_{i,j,k}$. The truncation is accomplished by setting the value of the interaction forces to be zero for all distances $|\mathbf{r} - \mathbf{r}'| > 3b$.

Equations (3.8) and (3.9) introduce $\Delta \mathbf{r}$, which gives the relative position of a bead inside the given cell labelled by indices (i', j', k') . Figure 3.1 provides an illustration of the vector $\Delta \mathbf{r}$ inside of an arbitrary cell labelled by (i, j, k) .

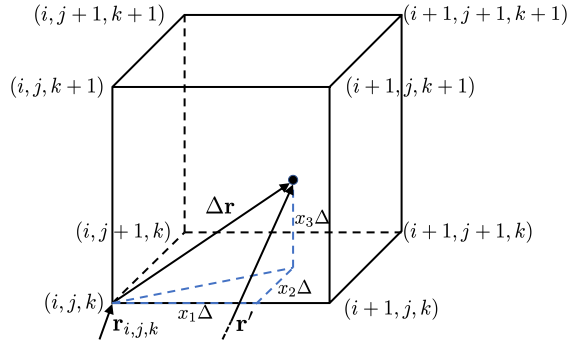


Figure 3.1: Diagram illustrating which vertex (i, j, k) is chosen to label a given cell along with the trilinear interpolation parameters x_1, x_2 and x_3 describing the positions of a bead relative to the cell vertex (i, j, k)

Equations (3.8) and (3.9) then can be written as

$$\begin{aligned} \psi_{i,j,k}^{(A)}(t) = \sum_{i',j',k'} \int_{\Delta\mathbf{r}} d(\Delta\mathbf{r}) & \left(\sum_{\sigma_1=0}^1 \sum_{\sigma_2=0}^1 \sum_{\sigma_3=0}^1 C_{\sigma_1,\sigma_2,\sigma_3}(\Delta\mathbf{r}) \left[\mathbf{F}_{int}^{(AA)}(\mathbf{r}_{i,j,k}, \mathbf{r}_{i',j',k'} + \Delta\mathbf{r}) \right. \right. \\ & \left. \left. \times \rho_{i'+\sigma_1,j'+\sigma_2,k'+\sigma_3}^{(A)}(t) + \mathbf{F}_{int}^{(AB)}(\mathbf{r}_{i,j,k}, \mathbf{r}_{i',j',k'} + \Delta\mathbf{r}) \rho_{i'+\sigma_1,j'+\sigma_2,k'+\sigma_3}^{(B)}(t) \right] \right), \end{aligned} \quad (3.11)$$

$$\begin{aligned} \psi_{i,j,k}^{(B)}(t) = \sum_{i',j',k'} \int_{\Delta\mathbf{r}} d(\Delta\mathbf{r}) & \left(\sum_{\sigma_1=0}^1 \sum_{\sigma_2=0}^1 \sum_{\sigma_3=0}^1 C_{\sigma_1,\sigma_2,\sigma_3}(\Delta\mathbf{r}) \left[\mathbf{F}_{int}^{(BB)}(\mathbf{r}_{i,j,k}, \mathbf{r}_{i',j',k'} + \Delta\mathbf{r}) \right. \right. \\ & \left. \left. \times \rho_{i'+\sigma_1,j'+\sigma_2,k'+\sigma_3}^{(B)}(t) + \mathbf{F}_{int}^{(BA)}(\mathbf{r}_{i,j,k}, \mathbf{r}_{i',j',k'} + \Delta\mathbf{r}) \rho_{i'+\sigma_1,j'+\sigma_2,k'+\sigma_3}^{(A)}(t) \right] \right). \end{aligned} \quad (3.12)$$

Equations (3.11) and (3.12) can be further simplified by noting that the time-dependent density fields no longer contain an explicit $\Delta\mathbf{r}$ dependence and can therefore be removed from the integrals:

$$\begin{aligned} \psi_{i,j,k}^{(A)}(t) = \sum_{i',j',k'} \sum_{\sigma_1,\sigma_2,\sigma_3=0}^1 & \left(\phi_{i'-i,j'-j,k'-k,\sigma_1,\sigma_2,\sigma_3}^{(AA)} \rho_{i'+\sigma_1,j'+\sigma_2,k'+\sigma_3}^{(A)}(t) \right. \\ & \left. + \phi_{i'-i,j'-j,k'-k,\sigma_1,\sigma_2,\sigma_3}^{(AB)} \rho_{i'+\sigma_1,j'+\sigma_2,k'+\sigma_3}^{(B)}(t) \right), \end{aligned} \quad (3.13)$$

$$\begin{aligned} \psi_{i,j,k}^{(B)}(t) = \sum_{i',j',k'} \sum_{\sigma_1,\sigma_2,\sigma_3=0}^1 & \left(\phi_{i'-i,j'-j,k'-k,\sigma_1,\sigma_2,\sigma_3}^{(BB)} \rho_{i'+\sigma_1,j'+\sigma_2,k'+\sigma_3}^{(B)}(t) \right. \\ & \left. + \phi_{i'-i,j'-j,k'-k,\sigma_1,\sigma_2,\sigma_3}^{(BA)} \rho_{i'+\sigma_1,j'+\sigma_2,k'+\sigma_3}^{(A)}(t) \right), \end{aligned} \quad (3.14)$$

where the indices $(i' - i, j' - j, k' - k)$ represent minimum separation distances on-grid and cannot give values that do not lie on a grid-point and the time-independent terms can be written out for a general bead species pair α and β as

$$\phi_{i'-i,j'-j,k'-k,\sigma_1,\sigma_2,\sigma_3}^{(\alpha\beta)} = \int_{\square} d(\Delta \mathbf{r}) C_{\sigma_1,\sigma_2,\sigma_3}(\Delta \mathbf{r}) \mathbf{F}_{int}^{(\alpha\beta)}(\mathbf{r}_{i,j,k}, \mathbf{r}_{i',j',k'} + \Delta \mathbf{r}). \quad (3.15)$$

While these sums contain many terms (184 terms for each cell and 8 terms for each vertex of a given cell), many of these terms are eightfold degenerate since a given grid point is shared by the 8 surrounding cells. The sums can be simplified to include only unique grid points by inserting the identity $1 = \sum_{i'',j'',k''} \delta_{i'',i'+\sigma_1} \delta_{j'',j'+\sigma_2} \delta_{k'',k'+\sigma_3}$. Equations (3.11) and (3.12) then become:

$$\begin{aligned} \psi_{i,j,k}^{(A)}(t) = & \sum_{i'',j'',k''} \sum_{\sigma_1,\sigma_2,\sigma_3=0}^1 \left(\phi_{i''-i,j''-j,k''-k,\sigma_1,\sigma_2,\sigma_3}^{(AA)} \rho_{i'',j'',k''}^{(A)}(t) \right. \\ & \left. + \phi_{i''-i,j''-j,k''-k,\sigma_1,\sigma_2,\sigma_3}^{(AB)} \rho_{i'',j'',k''}^{(B)}(t) \right), \end{aligned} \quad (3.16)$$

$$\begin{aligned} \psi_{i,j,k}^{(B)}(t) = & \sum_{i'',j'',k''} \sum_{\sigma_1,\sigma_2,\sigma_3=0}^1 \left(\phi_{i''-i,j''-j,k''-k,\sigma_1,\sigma_2,\sigma_3}^{(BB)} \rho_{i'',j'',k''}^{(B)}(t) \right. \\ & \left. + \phi_{i''-i,j''-j,k''-k,\sigma_1,\sigma_2,\sigma_3}^{(AB)} \rho_{i'',j'',k''}^{(A)}(t) \right). \end{aligned} \quad (3.17)$$

At this point, we note that the cell label index notation (i'', j'', k'') can be written as $(i + \Delta i, j + \Delta j, k + \Delta k)$. This transformation of index changes the summation over (i'', j'', k'') to be over $(\Delta i, \Delta j, \Delta k)$. We can explicitly enforce a truncation of the interaction forces by choosing the possible values of $(\Delta i, \Delta j, \Delta k)$. By invoking this alternate vertex labelling, we can write Equations (3.16) and (3.17) as sums over the allowed grid points defined by $(\Delta i, \Delta j, \Delta k)$:

$$\psi_{i,j,k}^{(A)}(t) = \sum_{\Delta i, \Delta j, \Delta k} \left(\Phi_{\Delta i, \Delta j, \Delta k}^{(AA)} \rho_{i+\Delta i, j+\Delta j, k+\Delta k}^{(A)}(t) + \Phi_{\Delta i, \Delta j, \Delta k}^{(AB)} \rho_{i+\Delta i, j+\Delta j, k+\Delta k}^{(B)}(t) \right), \quad (3.18)$$

$$\psi_{i,j,k}^{(B)}(t) = \sum_{\Delta i, \Delta j, \Delta k} \left(\Phi_{\Delta i, \Delta j, \Delta k}^{(BB)} \rho_{i+\Delta i, j+\Delta j, k+\Delta k}^{(B)}(t) + \Phi_{\Delta i, \Delta j, \Delta k}^{(AB)} \rho_{i+\Delta i, j+\Delta j, k+\Delta k}^{(A)}(t) \right), \quad (3.19)$$

where the coefficients $\Phi_{\Delta i, \Delta j, \Delta k}^{(\alpha\beta)}$ are given by

$$\Phi_{\Delta i, \Delta j, \Delta k}^{(\alpha\beta)} = \sum_{\sigma_1, \sigma_2, \sigma_3=0}^1 \phi_{\Delta i, \Delta j, \Delta k, \sigma_1, \sigma_2, \sigma_3}^{(\alpha\beta)}. \quad (3.20)$$

Equation (3.20) is calculated during our initialization routine as it does not require any future information about our system, only requires that the interaction force be calculated for a range of $3b$ as mentioned earlier. We also note, that the arrays $\Phi_{\Delta i, \Delta j, \Delta k}^{(\alpha\beta)}$ are spherically symmetric, which on a cubic grid is also a cubic symmetry. Therefore changing the sign of any index only changes the sign of the value stored in the array. These symmetries can be used to reduce the number of operations required to construct the array.

3.1.4 MPI Communication Routines

As previously discussed, our simulations run in parallel on P processors. While using multiple processors generally allows us to simulate larger systems faster than a single processor simulation, it introduces a complexity through the communication of data between processors. If the number of processors is large, we must pay close attention to how we exchange data between processes as it can have a significant impact on the efficiency of our simulation. Throughout the course of our simulation, there is a lot of information that must get passed between processes, such as density and mean force-field arrays which are calculated separately on each processor then combined and passed back to all processes. Naively, we could pass information from each processor to the main (rank 0) process, meaning that $P-1$ processes must send data to the main process. However, a given processor, in this case the

main process, can only receive data from one processor at a time. Therefore at each step of this communication stage, the other $P - 2$ processors are idle, waiting to send data or waiting until the remaining processors to send their data before resuming the simulation.

This is a sequential communication algorithm that is the basic send/receive algorithm available for communication. In a simple parallel program with only 2 processors this would be a sufficient algorithm to use without worrying about the impact on overall efficiency however, we typically use larger numbers of processors (8-32 processors) and therefore require a more optimized algorithm to perform communication between processors. In high-performance computing [41], a common algorithm used for communication routines is a so-called “tree-structured” algorithm, described schematically in Figure 3.2, which introduces a restriction on the number of processors such that P is a power of 2, however it only requires $\log_2 P$ steps to perform a gather (main process receives data from all other processes) or a scatter (main process data is sent to all other processes) communication routine.

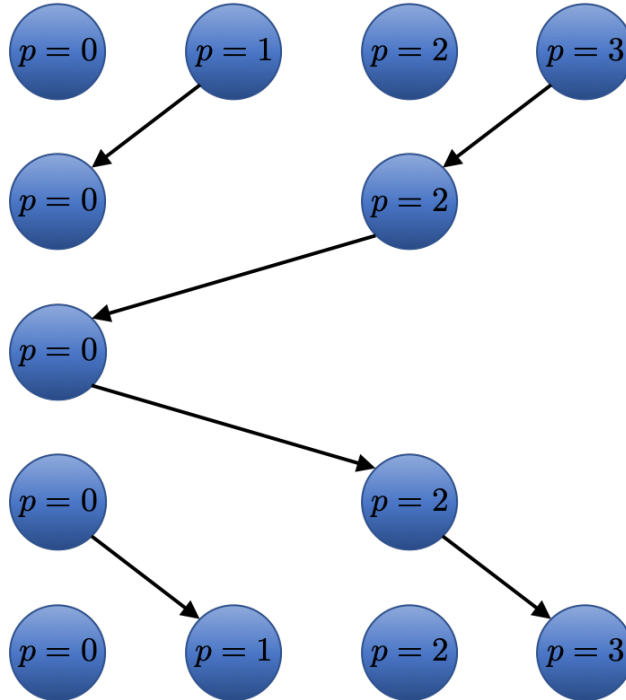


Figure 3.2: Schematic diagram of the tree-structured communication algorithm used to gather and scatter our mean field arrays for the case where $P = 4$.

3.1.5 Time Evolution Algorithm

Each bead in our simulation evolves according to Equation (2.41), which is the set of dimensionless Langevin equations.

The Langevin equation used in our simulation can be written using general operators

$$\frac{d\mathbf{R}_n(t)}{dt} = \mathbf{F}_{spr,n}(t) + \boldsymbol{\psi}_n(\mathbf{R}_n(t), t) + \mathbf{f}_n(t) = (\mathcal{A} + \mathcal{B} + \mathcal{C})\mathbf{R}_n(t), \quad (3.21)$$

where \mathcal{A} , \mathcal{B} and \mathcal{C} are operators associated with the spring-force, mean force-field and random force, respectively. Equation (3.21) has an exact solution

$$\mathbf{R}_n(t + \Delta t) = e^{(\mathcal{A} + \mathcal{B} + \mathcal{C})\Delta t} \mathbf{R}_n(t). \quad (3.22)$$

Using the operator scheme described in Section 3.1.5, Equation (3.21) is split into three equations which are applied sequentially at each time step. This is equivalent to approximating the solution to the Langevin equation as

$$\mathbf{R}_n(t + \Delta t) = e^{\mathcal{A}\Delta t} e^{\mathcal{B}\Delta t} e^{\mathcal{C}\Delta t} \mathbf{R}_n(t). \quad (3.23)$$

We solve this differential equation using numerical schemes, in which we solve the differential equation in three sequential steps, one for each operator on the right-hand side of Equation (2.41), where the solution to each equation is used as the initial condition for the subsequent equation:

$$\frac{d\mathbf{R}_n}{dt} = \boldsymbol{\psi}(\mathbf{R}_n, t) \quad (3.24)$$

$$\frac{d\mathbf{R}_n}{dt} = \mathbf{F}_{spr,n}(t) \quad (3.25)$$

$$\frac{d\mathbf{R}_n}{dt} = \mathbf{f}_n(t). \quad (3.26)$$

The advantage to using this scheme for our Langevin equation is that we can use different evolution schemes, as appropriate, for each operator. In particular, we are able to solve the second step exactly using Rouse modes, see Section 3.1.5.2.

3.1.5.1 Application of the Dynamical Force-Field

We apply the first-order Euler method to solve Equation (3.24) which evolves the system using the dynamical mean force-field according to

$$\mathbf{R}_n(t + \Delta t) = \mathbf{R}_n(t) + \Delta t \boldsymbol{\psi}(\mathbf{R}_n(t), t). \quad (3.27)$$

As discussed in Section 3.1.3, we only store the mean force-field at grid points while bead positions \mathbf{R}_n evolve off-grid and can evolve outside of the simulation box. Therefore, we interpolate the value of the mean force-field at the bead's image position using the same trilinear interpolation scheme used to interpolate the density fields in Section 3.1.3. Similar to the density field calculation in Section 3.1.2, a periodic image of the bead in the simulation box is generated, if necessary, then the mean force-field at the bead image position $\mathbf{r} = \mathbf{r}' + \Delta \mathbf{r}$ where $\mathbf{r}' = (i, j, k)\Delta$ and $\Delta \mathbf{r} = (x_1, x_2, x_3)\Delta$ is given by

$$\boldsymbol{\psi}_\alpha(\mathbf{r}, t) = \sum_{\sigma_1=0}^1 \sum_{\sigma_2=0}^1 \sum_{\sigma_3=0}^1 \boldsymbol{\psi}_{i+\sigma_1, j+\sigma_2, k+\sigma_3}^{(\alpha)}(t) f_{\sigma_1}(x_1) f_{\sigma_2}(x_2) f_{\sigma_3}(x_3) \quad (3.28)$$

where x_1 , x_2 and x_3 are the positions of the bead relative to the cell labelled by indices (i, j, k) and are defined by

$$\begin{aligned}
x_1 &= \frac{\Delta \mathbf{r}_x}{\Delta}, \\
x_2 &= \frac{\Delta \mathbf{r}_y}{\Delta}, \\
x_3 &= \frac{\Delta \mathbf{r}_z}{\Delta}.
\end{aligned} \tag{3.29}$$

3.1.5.2 Rouse Modes and the Spring Force

Equation (3.25) can be solved exactly using Rouse modes as they diagonalize the spring force matrix $A_n^{(m)}$ which is related to the spring force operator by

$$\mathbf{F}_{spr,n}(t) = \sum_m A_n^{(m)} \mathbf{R}_m(t), \tag{3.30}$$

where $A_n^{(m)}$ is an $N \times N$ tridiagonal matrix whose elements are determined by the dimensionless form of Equations (2.2) to (2.4) and can be written as:

$$A = \begin{pmatrix} -1 & 1 & 0 & 0 & 0 \\ 1 & -2 & 1 & 0 & 0 \\ 0 & 1 & \ddots & \ddots & 0 \\ 0 & 0 & \ddots & -2 & 1 \\ 0 & 0 & 0 & 1 & -1 \end{pmatrix}$$

The spring force matrix can then be diagonalized by performing a transformation to Rouse modes $\mathbf{X}_p(t)$:

$$\mathbf{X}_p(t) = \sum_n \phi_p^{(n)} \mathbf{R}_n(t), \tag{3.31}$$

where $\phi_p^{(n)}$ is the n th component of the p th orthonormal eigenvector of the spring force matrix and is given by

$$\phi_0^{(n)} = \frac{1}{\sqrt{N}} \quad (3.32)$$

$$\phi_p^{(n)} = \sqrt{\frac{2}{N}} \cos\left(\frac{\pi p(n + 1/2)}{N}\right), p = 1, \dots, N - 1. \quad (3.33)$$

Equation (3.25) becomes exactly solvable after the transformation to Rouse modes, which evolve according to

$$\frac{d\mathbf{X}_p}{dt} = -\lambda_p \mathbf{X}_p, \quad (3.34)$$

where λ_p are the eigenvalues of the diagonalized spring force matrix and are given by

$$\lambda_p = 2 \left[1 - \cos\left(\frac{\pi p}{N}\right) \right]. \quad (3.35)$$

Integrating Equation (3.31) for one time-step gives the solution

$$\mathbf{X}_p(t + \Delta t) = \mathbf{X}_p(t) e^{-\lambda_p \Delta t} \quad (3.36)$$

The dimensionless relaxation time τ_p associated with the p th Rouse mode can be determined from the right-hand side of Equation (3.36) by taking the inverse of the eigenvalue λ_p . The dimensionful relaxation time τ_p is given by

$$\tau_p = \frac{1}{2 \left[1 - \cos\left(\frac{\pi p}{N}\right) \right]} \tau = \frac{\zeta b^2}{6k_B T \left[1 - \cos\left(\frac{\pi p}{N}\right) \right]}, \text{ for } p > 0, \quad (3.37)$$

where $\tau = \zeta b^2 / (3k_B T)$ is the time-scale defined in Section 2.2.1. The $p = 0$ mode corresponds to centre of mass diffusion, which does not evolve at this stage as the random noise, which describes the centre of mass diffusive motion, is applied during the next operator splitting step. Here we note that we want our numerical method to resolve the fastest relaxation mode, which has a relaxation time

$$\tau_{N-1} = \frac{1}{2 \left[1 - \cos \left(\frac{\pi(N-1)}{N} \right) \right]} \tau. \quad (3.38)$$

In the limit of infinitely long chains, $N \rightarrow \infty$, $\tau_{N-1} \rightarrow \frac{\tau}{4}$. To resolve the fastest relaxation mode, we choose $\Delta t = \frac{\tau}{5}$ as it is less than $\frac{\tau}{4}$. To perform the above transformations from an ensemble of bead positions to Rouse modes, Equation (3.31) and then back to an ensemble of bead positions after evolving the Rouse modes in time via Equation (3.36), we make use of the fact that the Rouse modes eigenvectors are shifted cosines, allowing us to make use of fast cosine transforms [40, 42] to perform the transformations. We also generalize our algorithm for arbitrary chain length N (the previous implementation was limited to N being a power of 2) using padded discrete Fourier transforms as described in Appendix A.

3.1.5.3 Integration of the Noise Term

Integrating Equation 3.26 gives the solution

$$\mathbf{R}_n(t + \Delta t) = \mathbf{R}_n(t) + \int_t^{t+\Delta t} \mathbf{f}_n(t') dt'. \quad (3.39)$$

As $\mathbf{f}_n(t)$ is a random, Gaussian force, it follows that $\mathbf{R}_n(t + \Delta t) - \mathbf{R}_n(t) = \Delta \mathbf{R}_n(t)$ is also random and Gaussian. This allows us to characterize $\Delta \mathbf{R}_n(t)$ by its first and second moments, $\langle \Delta R_{n,\alpha}(t) \rangle$ and $\langle \Delta R_{n,\alpha}(t) \Delta R_{m,\beta}(t) \rangle$ using the first and second moments of the noise term $\mathbf{f}_n(t)$ which have the dimensionless (see Section 2.2.1) form:

$$\langle f_{n,\alpha}(t) \rangle = 0, \quad (3.40)$$

$$\langle f_{n,\alpha}(t) f_{n',\alpha'}(t') \rangle = \frac{2}{3} \delta_{\alpha\alpha'} \delta_{nn'} \delta(t - t'). \quad (3.41)$$

The first moment of $\Delta \mathbf{R}_n(t)$ is given by

$$\langle \Delta R_{n,\alpha}(t) \rangle = \int_t^{t+\Delta t} \langle f_{n,\alpha}(t') \rangle dt' = 0, \quad (3.42)$$

and the second moment is given by

$$\begin{aligned}
\langle \Delta R_{n,\alpha}(t) \Delta R_{m,\beta}(t) \rangle &= \int_t^{t+\Delta t} \int_t^{t+\Delta t} \langle f_{n,\alpha}(t') f_{m,\beta}(t'') \rangle dt' dt'' \\
&= \int_t^{t+\Delta t} \int_t^{t+\Delta t} \frac{2}{3} \delta_{\alpha\beta} \delta_{nm} \delta(t' - t'') dt' dt'' \\
&= \frac{2}{3} \delta_{\alpha\beta} \delta_{nm} \Delta t.
\end{aligned} \tag{3.43}$$

To implement this in our numerical procedure, we generate an uncorrelated random number at each time step which satisfies Equations (3.42) and (3.43). Bead positions in our simulation are therefore evolved at this step by

$$R_{n,\alpha}(t + \Delta t) = R_{n,\alpha}(t) + \sqrt{\frac{2\Delta t}{3}} \mathcal{N}(0, 1) \tag{3.44}$$

where $\mathcal{N}(0, 1)$ is a random number generated using a Box-Muller transformation that is characterized by the moments $\langle \mathcal{N}(0, 1) \rangle = 0$ and $\langle \mathcal{N}(0, 1)^2 \rangle = 1$.

3.1.5.4 Operator Splitting Error

Our numerical solution to the mean-field equations include approximations which introduce errors depending on the magnitude of the time step Δt . In particular, the use of operator splitting on the Langevin equation introduces a global error that scales linearly with Δt . A full, rigorous treatment of the error introduced by operator splitting is covered in Ref. [10]. Here, we simply present the results of this error analysis.

The error introduced by this scheme can then be observed by expanding the right-hand sides of Equations (3.22) and (3.23) in powers of Δt . The expansions yield results that differ in $\mathcal{O}(\Delta t^2)$ terms, introducing a local error of order Δt^2 which corresponds to a global error $\delta \mathbf{R}_n(t)$ of $\mathcal{O}(\Delta t)$. Furthermore, the methods used to solve Equations (3.24)-(3.26) can also introduce error. Equation (3.24) is solved exactly through the use of Rouse modes. Equation

(3.25), however, is solved using an Euler scheme which is not exact and introduces a global error in $\mathbf{R}_n(t)$ of $\mathcal{O}(\Delta t)$. Equation (3.26) is not solved exactly, however, the error introduced is a sampling error that has no Δt dependence.

3.1.6 BCC Ordering Field

In Chapter 4, we present results on the chain exchange between BCC-ordered micelles as well as chain diffusion in the BCC phase of diblock and triblock copolymer melts. An ordering field is initially applied to our system for $\sim 10\tau_R$ to ensure that the BCC phase is free of defects and that the BCC unit cell is aligned with the axes of the simulation box. The ordering field is then removed and the system is allowed to equilibrate an additional $\sim 20\tau_R$ before taking chain exchange and diffusion measurements.

The ordering field is applied to the system as a contribution to the mean force-field $\psi(\mathbf{r}, t)$. The BCC ordering fields $\psi_\alpha^{(bcc)}(\mathbf{r}, t)$ for a bead species α is calculated using Equations (3.5) and (3.6), but the density fields are replaced by a “single-mode” approximation of the density of the BCC phase for each species $\rho_A^{(bcc)}(\mathbf{r}, t)$. The two-species BCC ordering density fields with a BCC period of L_0 can be generated using 12 reciprocal lattice vectors $\mathbf{G}_i^{(bcc)}$ according to

$$\begin{aligned}\rho_A^{(bcc)}(\mathbf{r}, t) &= f_A + b_1 \sum_{i=1}^{12} \cos\left(q_0 \mathbf{G}_i^{(bcc)} \cdot \mathbf{r}\right) \\ \rho_B^{(bcc)}(\mathbf{r}, t) &= 1 - \rho_A^{(bcc)}(\mathbf{r}, t),\end{aligned}\tag{3.45}$$

where $q_0 = \frac{2\pi}{\sqrt{2}L_0}$ is the wave vector, b_1 is the amplitude of the modulations and the set of

reciprocal lattice vectors $\mathbf{G}_i^{(bcc)}$ are given by:

$$\begin{aligned}\mathbf{G}_1^{(bcc)} &= \left(\frac{1}{\sqrt{2}}, \frac{1}{\sqrt{2}}, 0 \right), & \mathbf{G}_2^{(bcc)} &= \left(\frac{1}{\sqrt{2}}, \frac{-1}{\sqrt{2}}, 0 \right), \\ \mathbf{G}_3^{(bcc)} &= \left(\frac{1}{\sqrt{2}}, 0, \frac{1}{\sqrt{2}} \right), & \mathbf{G}_4^{(bcc)} &= \left(\frac{1}{\sqrt{2}}, 0, \frac{-1}{\sqrt{2}} \right), \\ \mathbf{G}_5^{(bcc)} &= \left(0, \frac{1}{\sqrt{2}}, \frac{1}{\sqrt{2}} \right), & \mathbf{G}_6^{(bcc)} &= \left(0, \frac{1}{\sqrt{2}}, \frac{-1}{\sqrt{2}} \right), \\ \mathbf{G}_{i+6}^{(bcc)} &= -\mathbf{G}_i^{(bcc)}, & \text{for } 1 \leq i \leq 6.\end{aligned}$$

3.2 Analysis and Routines

This section concerns the analysis algorithms implemented to calculate chain extraction relaxation times, preferred BCC period, and diffusion coefficients. Since these algorithms are mainly used to sample statistics at various timesteps they do not affect runtime significantly and therefore we are not concerned with their optimization.

3.2.1 Estimation of Equilibrium BCC Period

It is important to ensure that our simulations are performed as close to equilibrium as possible, to avoid spurious effects and interpretations of our results. As well, we wish to make comparisons with other theories and experiments that are at equilibrium. For the system to be in equilibrium, the proper simulation box size must be chosen to allow the BCC ordered phase to be completely relaxed (i.e. as little deformation in the spherical micelles as possible). In most mean-field theories, finding this equilibrium box size is a trivial process, simply computing the free energy of different system sizes and finding the free energy minimum allows easy calculation of the preferred BCC period. However, since in our dSCFT we do not have direct access to the free energy of our system, we need to find an alternative way to determine the equilibrium BCC period.

Using rudimentary methods, we are able to estimate the equilibrium BCC period of our

systems. The first method explored is derived from epitaxial arguments relating the lamellar period to the BCC period. This method was used in Reference [10] to estimate the period used to construct ordering fields for the block copolymer phases. According to epitaxy, the equilibrium lamellar spacing is related to the equilibrium BCC period, $L_0^{(LAM)} = L_0^{(BCC)}/\sqrt{2}$. We note that the assumption that this relationship holds is not perfect, and can introduce an error in our estimated equilibrium period up to as much as 10% [43].

To apply the epitaxial relationship, we must have access to the lamellar equilibrium spacing, $L_0^{(LAM)}$. We can estimate this equilibrium spacing by setting up a system in a box with dimensions (L_x, L_y, L_z) and applying an lamellar ordering field with n layers. We note that the lamellar ordering field aligns the lamellar normal with the y -axis, forcing the system to have a lamellar period of L_y/n . If this period is equal to the true equilibrium period $L_y/n = L_0^{(LAM)}$ then the free energy should be at a minimum. If L_y/n is offset from $L_0^{(LAM)}$ far enough then the system should transition to a more stable state with $(n - 1)$ or $(n + 1)$ layers depending on the direction of the offset. Then by plotting the lengths at which the transitions first occur for various values of n and taking the average of the two transitions we can then determine the estimated equilibrium period by taking the slope of these averaged transitions. Reference [10] provides an in-depth explanation of this method and used this method for the diblock copolymer melt at $\epsilon N = 0.256$ with $f_A = 0.5$ and found $L_0^{(LAM)} = 14b$, which corresponds to an equilibrium BCC period of $L_0 = 19.8b$. While this method is well laid-out for determining the lamellar period, what are the appropriate values of ϵN and f_A that should be used to properly estimate the BCC period is still an open question. That is, the equilibrium period is dependent on ϵN , therefore we should take care to find the lamellar period at a value of ϵN that the copolymer melt will order into a stable BCC phase. Further, the BCC phase is not stable at $f_A = 0.5$ where the LAM phase is stable. Therefore when using lamellar epitaxy it is unclear if we should consider the metastable lamellar phase that forms for $f_A = 0.2$ rather than $f_A = 0.5$. These open questions must be considered before this method can be used to accurately determine the

equilibrium BCC period.

We also note that the method of varying the number of lamellar layers has an analogous BCC method in which one varies the number of unit cells in the simulation along a single axis and observes where the transitions from n unit cells to $(n + 1)$ and $(n - 1)$ unit cells occur. Using this method, we were unsuccessful in finding accurate transitions due to the presence of defects and the appearance of other phases (typically the HEX phase) as the box was stretched.

Equilibrium SCFT is also capable of calculating the equilibrium BCC period, by minimizing the free energy with respect to the unit cell size. However, this requires a mapping between our interaction strength ϵ and the Flory-Huggins interaction parameter χ . Reference [10] provides a mapping between the two parameters by mapping the dSCFT phase diagram for an AB diblock copolymer melt onto that calculated by SCFT [23]. This mapping, $\chi \approx 60\epsilon$ then provides an approximate method for choosing the equilibrium BCC period. This mapping holds well for the AB diblock copolymer melt, however it remains to be seen if this mapping is just as accurate for the ABA and BAB triblock copolymer melts. Therefore this mapping may introduce some additional error for the triblock copolymer melts. Tables 3.1, 3.2 and 3.3 show the values for L_0 calculated using SCFT as well as the values used in our simulations that are presented in Chapter 4. The values for L_0 used in Chapter 4 do not significantly differ from those calculated using SCFT, with the largest percent difference between values being $\sim 23.6\%$.

ϵN	χN	$L_0^{(SCFT)}$	L_0	% difference
0.4	24	4.52	4.96	9.7%
0.5	30	4.77	*	20.7%
0.6	36	5.00	*	15.2 %
0.7	42	5.13	*	12.3%
0.8	48	5.38	5.76	7.1%
0.9	54	5.55	*	3.8%
1.0	60	5.73	*	0.5%

Table 3.1: Table of equilibrium period data for the AB diblock copolymer melt. The first two columns are the interaction strength ϵN and the remapped Flory-Huggins interaction parameter χN . The third column is the equilibrium BCC period (in units of R_g) calculated using SCFT at χN . The fourth column contains the values used in simulations found in Chapter 4, where the asterisk means that the value of $5.76R_g$ was used for the period. The final column gives the percent difference between the $L_0^{(SCFT)}$ and L_0 values.

ϵN	χN	$L_0^{(SCFT)}$	L_0	% difference
0.8	48	3.32	3.40	2.4%
0.9	54	3.40	*	0.0%
0.92	55.2	3.42	*	0.6%
0.94	56.4	3.44	*	1.2%
0.96	57.6	3.45	*	1.4%
0.98	58.8	3.47	*	2.0%
1.0	60	3.48	*	2.3%

Table 3.2: Table of equilibrium period data for the ABA triblock copolymer melt. The first two columns are the interaction strength ϵN and the remapped Flory-Huggins interaction parameter χN . The third column is the equilibrium BCC period (in units of R_g) calculated using SCFT at χN . The fourth column contains the values used in simulations found in Chapter 4, where the asterisk means that the value of $3.40R_g$ was used for the period. The final column gives the percent difference between the $L_0^{(SCFT)}$ and L_0 values.

ϵN	χN	$L_0^{(SCFT)}$	L_0	% difference
0.7	42	3.30	*	23.6%
0.8	48	3.41	*	19.6%
0.9	54	3.50	*	16.6%
1.0	60	3.59	4.08	13.6%
1.1	66	3.67	*	11.1%
1.2	72	3.73	*	9.4%
1.3	78	3.79	*	7.7%
1.4	84	3.86	*	5.7%

Table 3.3: Table of equilibrium period data for the BAB triblock copolymer melt. The first two columns are the interaction strength ϵN and the remapped Flory-Huggins interaction parameter χN . The third column is the equilibrium BCC period (in units of R_g) calculated using SCFT at χN . The fourth column contains the values used in simulations found in Chapter 4, where the asterisk means that the value of $4.08R_g$ was used for the period. The final column gives the percent difference between the $L_0^{(SCFT)}$ and L_0 values.

We note, that despite investigating the lamellar epitaxy method we have sparse results for this method. The values for L_0 that we use in Chapter 4 were calculated using a method that was intended to take advantage of the periodicity of the system having identical core volumes at equilibrium for any number of unit cells. By applying a relative strain, we expected that the core volume, out of equilibrium, would differ when increasing the number of unit cells in the system. It can be shown, however, that the core volume will scale the same outside of equilibrium regardless of the relative strain applied, which can be seen in Figure 3.3 as the data for two and three unit cells collapses onto the curve for a single unit cell average core volume. Also plotted in Figure 3.3, is the theoretical result for the average micelle core volume in a highly segregated melt $V_{core} = L_0^3 f_A / 2$. The core volumes calculated in these simulations are found to be smaller than the highly segregated melt due to the presence of unimers in the system, meaning that the system is not perfectly segregated, but very well segregated. We note that the values we calculated using this method are purely artificial

despite giving seemingly reasonable values. The results using these equilibrium periods are presented in Chapter 4 and appear to yield qualitatively accurate data. However, future work will be devoted to deriving a physically accurate and efficient method for calculating the equilibrium BCC period using dSCFT.

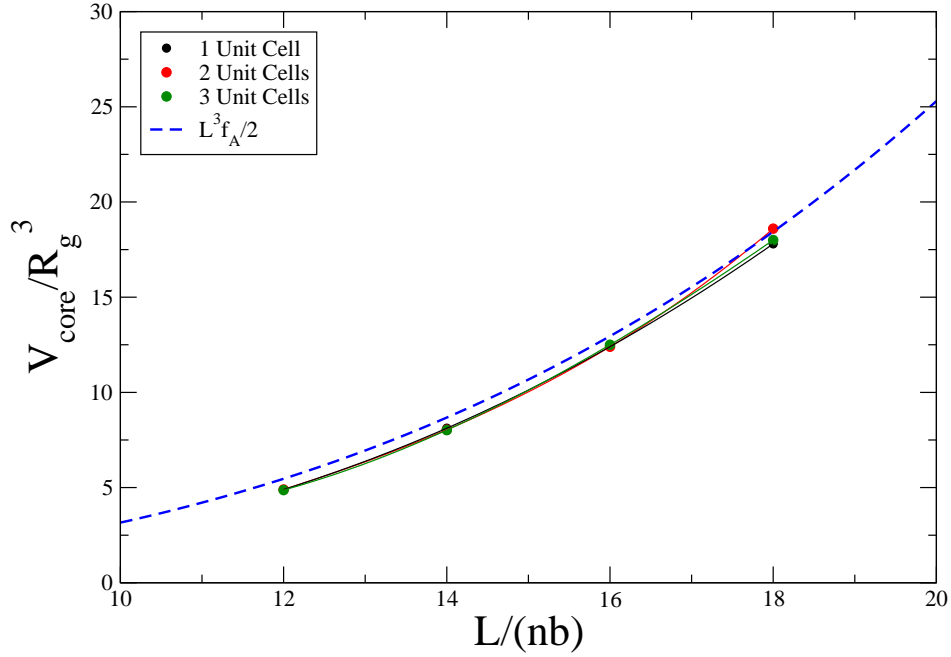


Figure 3.3: Micelle core volume of BAB copolymers as a function of L/n where n is the number of unit cells in the system along the (100) axis. The data collapses onto the curve for a single unit cell and follows a similar trend to the theoretical prediction of the average micelle core volume in a highly segregated melt (shown in blue).

We have examined, on a preliminary basis, further methods for determining the equilibrium period such as the polymer contribution to the stress tensor. Further investigations into a thermodynamic route, possibly involving the stress tensor, for calculating L_0 without the use of equilibrium SCFT constitutes future work for this project.

3.2.2 Chain Labelling

In Section 1.2.1, chain exchange was described in the context of TR-SANS experiments [5]. The rate of chain exchange in these experiments were measured using a relaxation function that described the extent of mixing between hydrogenated and deuterated polystyrene micelle cores. For our simulations to produce relaxation functions, we require a way to measure how well-mixed our cores become as a function of time. We use the so-called "micelle hybridization" method used by Li and Dormidontova [29] to characterize chain mixing between micelles. This method labels micelles (and all chains forming the micelles) using a binary labelling scheme such that half of the micelles are labelled as 0 and half as 1.

Before labels can be assigned to micelles, we must first identify the micelles in our system. We use a micelle counting routine that loops over all grid points (i, j, k) within our simulation box and checks if the compositional order parameter $\rho_{i,j,k}(t) = \rho_{i,j,k}^{(A)}(t) - \rho_{i,j,k}^{(B)}(t)$ is above a threshold density $\rho_{threshold} = (\rho_{max} - \rho_{min})/2$, where ρ_{max} and ρ_{min} are the maximum and minimum values of the compositional order parameter, respectively. The compositional order parameter $\rho_{i,j,k}(t)$ is used as a measure of which species of beads is most likely to be found at a given grid point (i, j, k) . For values of $\rho_{i,j,k}(t) > \rho_{threshold}$, the micelle core-forming A species are more likely to be found, and vice-versa. At each grid point, if $\rho_{i,j,k}(t)$ is above the threshold density, we perform the same check on all neighbouring grid points. This check is then performed recursively for all neighbours of any site that is above the threshold until there are no more sites that pass the check. All the sites in this recursive loop that are above the threshold are labelled as a single, unique micelle core. Every site that has been checked already is labelled as "checked" so that sites are not visited more than once in the algorithm. This is then repeated until all sites in the simulation are checked and all unique micelle cores are identified.

Once we have identified the micelles, we label the micelles as either 0 or 1. In the context of the TR-SANS experiments, we can consider 0-labelled micelles as hydrogenated cores and 1-labelled micelles as deuterated. We achieve a 50% mix of hydrogenated and deuterated

micelles by randomly selecting an unlabelled micelle and alternately labelling micelles as 0 or 1.

After a micelle core is labelled, the chain-replicas that form the aggregate associated with that micelle core are given the micelle core label. Our labelling scheme for chain-replicas is accomplished by calculating the chain-replicas core block centre of mass and associating this centre of mass with a grid point. That is, we only calculate the centre of mass of the core block, not the entire chain. Bead positions evolve off-grid and can be located outside of the simulation box, therefore we cannot always associate the absolute position of the centre of mass with a grid point. We take the periodic image of the centre of mass which is guaranteed to be located within the simulation box and associate it with the grid point (i, j, k) to which it is closest. We then assign the chain the same micelle core label as this grid point. If the grid point does not have a label (i.e. there is no micelle core at this location), the chain-replica is treated as a unimer. We then assign labels to these unimers such that roughly half of the chain replicas in our system are labelled 0, and the other half are labelled 1. This is done to eliminate statistical discrepancies when calculating the extent of mixing in our system as described in Section 3.2.3.

3.2.3 Calculation of chain extraction relaxation time

One of the main purposes of this thesis is to describe the effects of chain architecture on change exchange kinetics. Therefore quantifying the relaxation time of the chain extraction mechanism is an important calculation. The relaxation time is related to the relaxation function of our system which describes the extent of chain mixing at a given time t . Li and Dormidontova [29] have performed DPD simulations to study chain exchange kinetics and use a "hybridization" labelling technique to calculate the relaxation function $R(t)$. In our simulations we use the chain labelling scheme outlined in Section 3.2.2. The relaxation function $R(t)$ is given by

$$R(t) = 4 \left\langle \sum_{micelles} \left[\left(\frac{N_r(t)}{N(t)} - \frac{1}{2} \right)^2 \frac{N(t)}{N_{total}} \right] \right\rangle, \quad (3.46)$$

where the sum is over all micelles in the system. $N_r(t)$ is the number of chains that are labelled 1 that are associated with the given micelle, $N(t)$ is the total number of chains associated with the micelle and N_{total} is the total number of chains in the ensemble. At $t = 0$ this relaxation function is identically unity as all chains associated with a given micelle at $t = 0$ will have the same label, i.e. $N_r/N = 0$ or 1 exactly. At long times the term $N_r(t)/N(t)$ should be approximately $\frac{1}{2}$, meaning that the relaxation function should plateau at a value close to zero. The long time plateau value will depend on various factors such as the presence of unimers, the micelle size distribution and a mismatch in the number of hydrogenated and deuterated chains, i.e. if initially there is not a perfect 50/50 mix of the two types of labelled chains. These factors can be taken into account by calculating the contrast function $C(t)$:

$$C(t) = \left(\frac{R(t) - R(\infty)}{R(0) - R(\infty)} \right)^{1/2}, \quad (3.47)$$

where $R(\infty)$ is the plateau at long times, which is calculated by averaging over long time values. In our simulations, we average over approximately the final $15\tau_R$ to calculate this average.

3.2.4 Aggregate Equilibrium Properties

To properly characterize our system we must calculate equilibrium properties of the micelles formed. From equilibrium properties such as the aggregation number and micelle core volume we can observe how well segregated our micelles are which can be related to chain exchange kinetics.

Following the labelling scheme in Section 3.2.2, we determine the aggregation number of each micelle by calculating the centre of mass, and its periodic image if necessary, of each

replica chain's core block and associating it with the nearest grid point. The replica chain is then given the same label as the grid-point as determined by the algorithm in Section 3.2.2. Once every replica chain has a label, we loop through all chains and increment the aggregation number of the appropriate micelle. This method also accounts for unimers in the system as a grid-point can be labelled 0, meaning the chain is associated with the B-rich domain outside of the micelle cores. The aggregation numbers calculated in this way are the aggregation number of replica chains in our system. The number of physical chains in each micelle can then be calculated as each replica chain contributes $1/\langle N_b \rangle$ to the aggregation number. In our simulations, we have chosen $\langle N_b \rangle = 60$ to optimize our simulations according to Reference [10].

As the energy barrier associated with core block extraction is related to the size of the micelle, we calculate the volume of each micelle core as part of our micelle identification algorithm. The micelle core volume V_{core} is the sum of the all unit cells of size Δ^3 that pass the criterion $\rho > \rho_{threshold} = (\rho_{max} - \rho_{min})/2$ as outlined previously.

The stability and segregation of our micelles can be observed by calculating these properties for various values of our interaction strength and serve as the basis for interpretation of dynamical results found in the next chapter.

Chapter 4

Results

The techniques and analysis outlined in the previous section allows us to use dSCFT to study chain exchange kinetics of the asymmetric AB diblock copolymer, and the corresponding symmetric ABA and BAB triblock copolymers. In this section, we present results of extensive simulations of dense polymeric melts for each of these architectures. First, we characterize the equilibrium properties of our systems. Then we examine dynamical properties which relate to the problem of chain exchange between spherical micelles formed in the body-centred cubic (BCC) microphase.

The environment (i.e. micelle size, intermicellar distance, aggregation number) in which the chains evolve depends on the chain architecture. As such, we also present results for blends consisting of a majority of diblock copolymer with a small amount of one architecture of the triblock copolymers also within the system. The goal of these simulations is to make a more direct comparison to the diblock case in a constant environment, which is essentially the AB background, such that only the triblock chain architecture should have an effect on the triblock chain kinetics. This way we eliminate any effects created by the different micelle environments that exist in the pure melts. Not only can we compare the triblock copolymers to the AB diblock copolymer background, we can also compare triblock chain architectures directly as the constant AB diblock background is the same for both cases.

4.1 Equilibrium Properties

Characterizing equilibrium properties such as the phase diagram, micelle aggregation number and unimer fraction allows us to ensure that our system is forming equilibrium structures, in particular the BCC phase. We are concerned with equilibrium chain exchange between spherical micelles so we will focus on a region of phase space where the BCC phase is formed. For the asymmetric AB diblock, symmetric ABA and symmetric BAB triblocks, the equilibrium BCC phase will form at a core monomer fraction of $f_A = 0.2$. All subsequent data presented, unless otherwise noted, are for chains with this core monomer fraction.

4.1.1 AB Diblock Copolymer Melt

Figure 4.1 shows a slice of the phase diagram for asymmetric AB diblock simulations at a core monomer fraction of $f_A = 0.2$. Each datapoint in Figure 4.1 is a single simulation. Each simulation is initialized in the disordered phase, then a BCC ordering-field is applied for $\approx 10\tau_R$, as discussed in Section 3.1.6. The ordering field is then turned off and the system is allowed to evolve for an additional $\approx 15\tau_R$ before we collect data for the relaxation function and centre-of-mass chain diffusion of the system. We then allow the system to evolve for long times, roughly $\approx 250\tau_R$. The final phase of the system can then be determined by observing the compositional order parameter $\rho_{i,j,k}(t) = \rho_{i,j,k}^{(A)}(t) - \rho_{i,j,k}^{(B)}(t)$. Examples of the final phases observed are shown in Figure 4.2. The order-disorder transition (ODT) between the disordered phase (DIS) and the BCC phase is roughly located at $\epsilon N \approx 0.4$. This result agrees with the data presented in Ref. [10] which gives an ODT at $\epsilon N \approx 0.4$ for a core monomer fraction of $f_A = 0.1875$. It is possible to find a more precise ODT, however this is not within the scope of our research. A more extensive phase diagram, covering a larger range of core monomer fractions and phases, for the asymmetric AB diblock obtained from this dSCFT is presented in Reference [10].

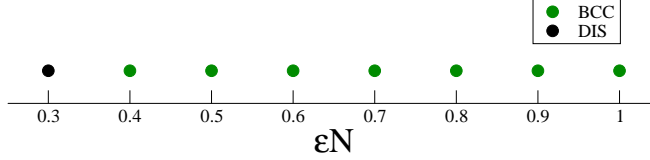


Figure 4.1: Slice of the phase diagram for asymmetric AB diblocks with chain length $N = 60$ and $f_A = 0.2$. Each simulation was performed in a simulation box of size $L = 36.4b$ with BCC period $L_0 = 18.2b$, the equilibrium period when $\epsilon N = 0.8$.

Following Section 3.2.1, the equilibrium BCC period used in our simulations for $\epsilon N = 0.8$ is $L_0 = 18.2b$. This value was used to determine the phase diagram for all values of ϵN that were simulated. To quantify how much the equilibrium BCC period changes with interaction strength we calculated the equilibrium period at the ODT segregation strength $\epsilon N = 0.4$ using SCFT and found a $\sim 16\%$ decrease in the equilibrium period. We have chosen to use a single BCC period for all segregation strengths simulated by our method despite this shift, and the interpretations of the results are made with this mind. We can judge the accuracy of our results by comparing our equilibrium BCC period values to those calculated using SCFT. The estimated conversion between χ and ϵ values is a linear mapping of the AB diblock copolymer melt phase diagram in Reference [10] to the SCFT AB copolymer melt phase diagram presented in [23], giving the approximate relationship $\chi \approx 60\epsilon$. For $\epsilon N = 0.8$ ($\chi N = 48$), we found $L_{SCFT} = 17.0b$ compared to our value of $L_0 = 18.2$, a 7.1% difference. We also found for $\epsilon N = 0.4$ ($\chi N = 24$) that $L_{SCFT} = 14.3b$, compared to our value used of $L_0 = 15.7b$, a 9.8% difference.

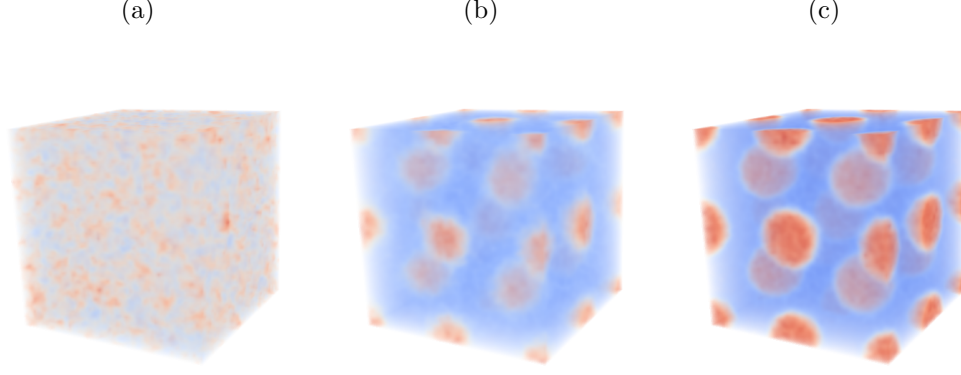


Figure 4.2: Compositional order parameters $\rho_A - \rho_B$ of AB diblock simulations after evolution for $\sim 250\tau_R$ for various values of ϵN showing (a) the DIS phase at $\epsilon N = 0.3$, (b) a weakly segregated BCC phase at $\epsilon N = 0.4$ and (c) a strongly segregated BCC phase at $\epsilon N = 1.0$. The red regions in the diagrams are A-rich domains, while the blue regions are B-rich.

The average aggregation number N_{agg} of BCC spherical micelles is plotted in Figure 4.3 as a function of interaction strength ϵN . Close to the ODT, the aggregation number is small, then increases rapidly as ϵN increases into the stable BCC region. At large values of ϵN the aggregation number begins to reach a plateau, as we hold the BCC period fixed as we increase ϵN . It would be expected that N_{agg} would continue to increase as we increase ϵN , however the number of chains in our simulations is fixed, as are the number of micelles, leading to a plateau in the aggregation number as the number of unimers decreases. N_{agg} will plateau to a lower bound of 50 chains per micelle as we have fixed the number of chains in our system. This lower bound is sufficient for our simulations and can be compared to the results in References [29] [30] and [28]. References [29] and [30] use DPD simulations to calculate an average aggregation number of $N_{agg} = 31 \pm 4$ determined from a number-average aggregation number distribution for an AB diblock with $N = 12$ and $f_A = 0.33$ at a segregation strength of $\chi N \approx 51$ (estimated as $\epsilon N \approx 0.86$). Ref. [28] also used DPD simulations and found $N_{agg} \approx 20$ for AB diblocks with $N = 18$ and $f_A = 0.25$ at a segregation strength of $\chi N \approx 96$ ($\epsilon N \approx 1.6$).

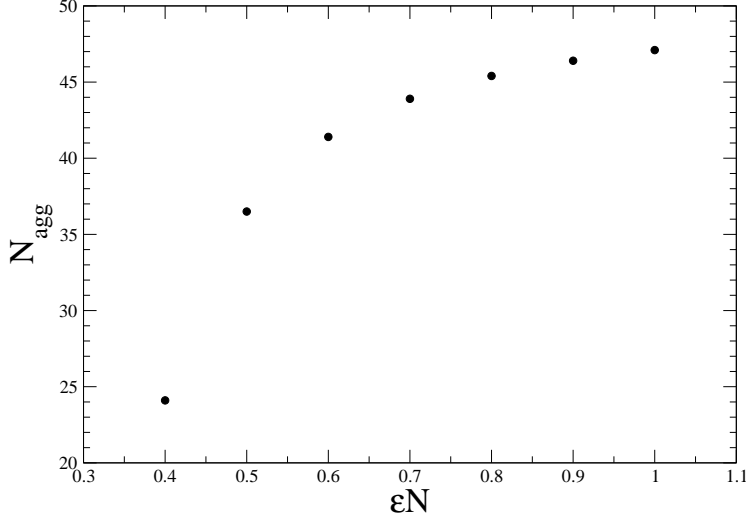


Figure 4.3: Average aggregation number for micelles formed in the BCC phase for asymmetric AB diblocks with chain length $N = 60$ and core monomer fraction $f_A = 0.2$. Each simulation was performed in a box of size $L = 36.4b$ and $L_0 = 18.2b$.

Not all chains in our system are associated with a micelle core at any given time, according to the association criterion discussed in Section 3.2.2. These chains are referred to as unimers and are associated with the B-rich regions of our system. Figure 4.4 shows the fraction of chains in our system that are not associated with a micelle, f_{unimer} . At the smallest value of ϵN , f_{unimer} is fairly significant, showing that $\sim 52\%$ of chains in our simulation unassociated with micelle cores. As ϵN increases, the number of chains that are not associated with a micelle decreases rapidly to values below 10%. The data in Figures 4.3 and 4.4 can be considered measures of how well our system is segregated. Values of ϵN that have a small aggregation number and a large unimer fraction can be considered weakly segregated as chains are just as likely to form micelles as they are to be located in a micelle corona. This means that the enthalpic penalty for a core block to be exposed to the corona is small, allowing for chains to exchange between micelle cores at a fast rate. This result makes sense since the value ϵ is the depth of the attractive potential well for like bead species. Therefore for large values of ϵN , we would expect the micelles to be more segregated as the potential

well is deeper.

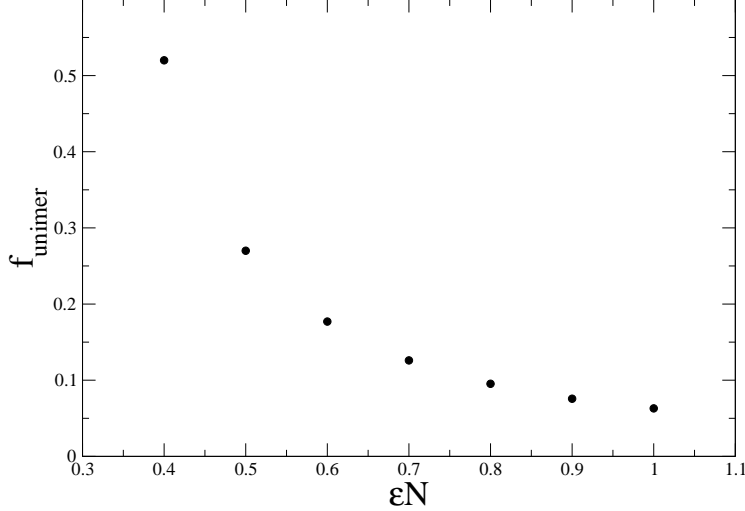


Figure 4.4: Fraction of unimers present in simulations of asymmetric AB diblocks with chain length $N = 60$ and core monomer fraction $f_A = 0.2$. Each simulation was performed in a box of size $L = 36.4b$ and $L_0 = 18.2b$.

Figure 4.5 shows the micelle core volume V_{core} scaled by the average aggregation number N_{agg} as a function of segregation strength ϵN . The inset graph shows the micelle core volume in units of R_g^3 . As expected, the average micelle core increases its volume as they become more segregated, reaching a plateau at high segregation strengths. We expect to observe a correlation between the average aggregation number and the average micelle core volume. In fact, for micelles in a highly selective solvent, where the core-corona boundary is strongly segregated, the micelle core volume should follow the relationship $V_{\text{core}} \sim N_{\text{agg}} N_A b^3$ [22]. Therefore at high segregation strengths in our melts, we would expect to see the same behaviour. For our strongest segregation strength $\epsilon N = 1.0$, the ratio of the core volume to the aggregation number gives us a value of $V_{\text{core}}/(N_{\text{agg}} b^3) = 12.6$ instead of the predicted value of $N_A = 12$. The 5% disagreement between these values can be attributed to the fact that we simulate a melt of polymers that contain a non-zero number of unimers. According to our unimer fraction at this value of ϵN we have ~ 51 unimers in our system, which

corresponds to roughly 0.64 core beads per micelle not inside of a micelle core, which is roughly the difference in our measured and theoretical values for N_A . As well, how we define the association of a chain to a micelle can introduce some error. A chain is defined as associated with a micelle if its core block centre of mass lies within the micelle core, therefore “intruder chains” that have a centre of mass outside the core-corona boundary but have some beads within the micelle core will contribute to the volume of the core but aren’t counted in the aggregation number calculation. This error, however, becomes less likely at higher segregation strength as the interface between the core and corona is much sharper than at low segregation strengths.

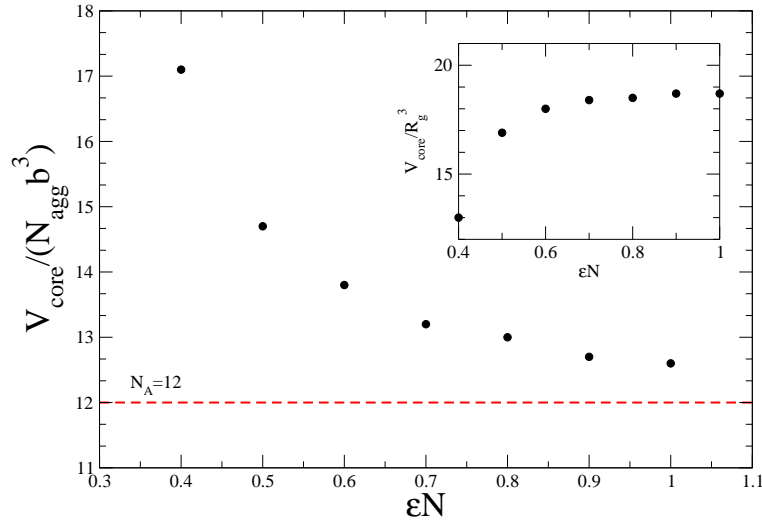


Figure 4.5: Average micelle core volume V_{core} scaled by $N_{agg} b^3$ as a function of segregation strength ϵN for asymmetric AB diblocks with chain length $N = 60$ and core monomer fraction $f_A = 0.2$. The inset graph shows V_{core} as a function of ϵN , without any scaling. Each simulation was performed in a box of size $L = 36.4b$ and $L_0 = 18.2b$.

4.1.2 ABA Triblock Copolymer Melt

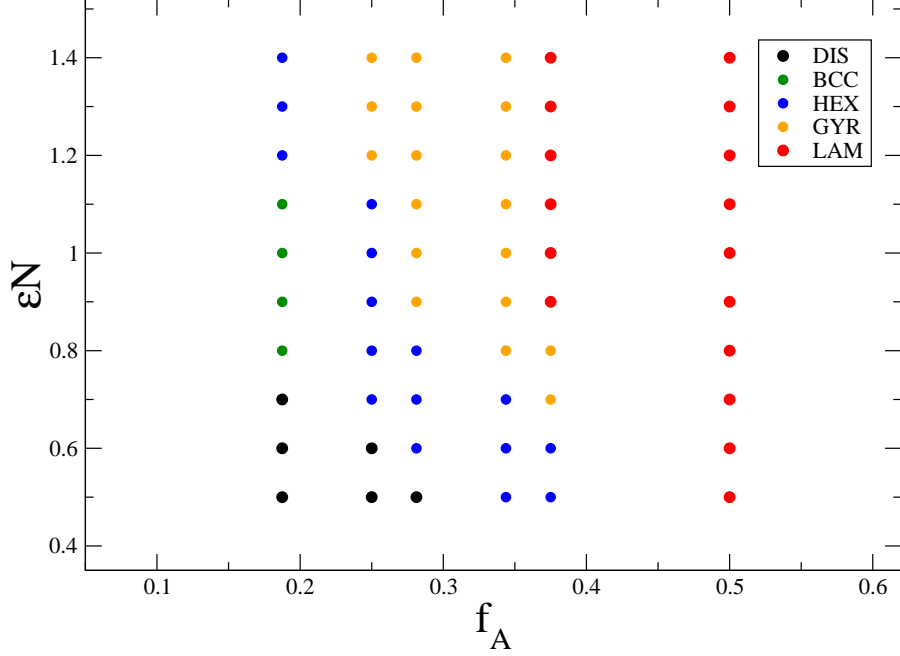


Figure 4.6: ABA triblock phase diagram for chains of length $N = 64$ and box length $L = 32b$. We observe the usual block copolymer body-centered cubic (BCC), gyroidal (GYR), Hexagonally-packed cylinder (HEX) and lamellar (LAM) phases. The BCC unit cell period at $\epsilon N = 0.8$, $f_A = 0.2$ is simulated using $L_0 = 15.2b$.

In Figure 4.6, The results of extensive simulations of ABA triblock copolymers are plotted to show the phase diagram. Each simulation was initialized in a disordered phase and then quenched instantaneously, without the use of ordering fields, to different target values of the interaction strength ϵN , then the system was allowed to evolve for long times, $\sim 200\tau_R$. By examining the difference in the monomer density fields, $\rho_A - \rho_B$, we can identify which phase the system entered at the end of the simulation. We note here that each simulation in Figure 4.6 was performed for the same BCC period and not adjusted for changing segregation strength. Therefore, the transitions between phases may not be exact, yet are accurate enough to determine a range of segregation strengths where the BCC phase is stable. Using

a fixed period can also introduce defects into the phases observed as the box size is not necessarily commensurate for the phase. For example, we have observed the HEX phase to exhibit spiralling cylinders when simulated in a box with equal length sides.

As seen in Figure 4.6, we observe all the classical phases observed for the diblock copolymer. While we are capable of ordering the system in each of these phases, the phase we are concerned with in this work is the BCC region at $f_A = 0.2$ which is shown by the green data points at $f_A = 0.2$. From these simulations, we can see that for ABA triblock copolymers there is a large region of BCC when the core monomer fraction is $f_A = 0.2$. The ODT between the DIS and BCC phase is estimated by this data to be at $\epsilon N = 0.8$, roughly twice the ODT for asymmetric AB diblocks with the same $f_A = 0.2$. This trend is observed using equilibrium SCFT as well as shown in Ref. [23] where the ODT for symmetric ABA triblocks ($\chi N \approx 20$) is double that of asymmetric AB diblocks ($\chi N = 40$) at $f_A = 0.2$. We also note that using equilibrium SCFT calculations we found the equilibrium BCC period to be $L_{SCFT} = 15.2b$ at $\epsilon N = 0.8$ ($\chi N = 48$), which is in agreement with the value we used in our simulations.

We also characterize the average micelle aggregation number N_{agg} and the fraction of unassociated core blocks for values of ϵN that fall in the region $0.8 \leq \epsilon N \leq 1.0$ where the BCC phase is formed. Figures 4.7 and 4.8 exhibit the expected trends of increasing N_{agg} and decreasing unassociated core block fraction as the segregation strength increases, respectively. This allows us to see how well our micelles are segregated across our simulation box. For the values of ϵN simulated, the system is not strongly segregated as $\approx 30\%$ of the core blocks in the system are unassociated with a micelle when the segregation strength is at its highest value.

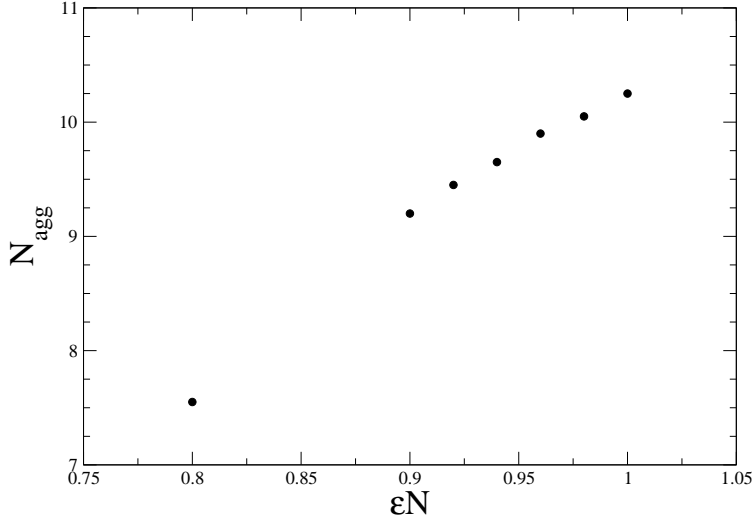


Figure 4.7: Average chain aggregation number of micelles formed in the BCC phase for symmetric ABA triblocks with chain length $N = 120$ and core monomer fraction $f_A = 0.2$. Each simulation was performed in a box of size $L = 30.4b$ and $L_0 = 15.2b$.

Being weakly segregated (i.e having a non-negligible unimer fraction) should allow the core blocks to extract from micelle cores at a faster rate than in a highly segregated system. We also note here that the fraction of unassociated core blocks for ABA triblocks as a function of ϵN decreases at a slower rate than both the AB diblock and BAB triblock unimer fractions, see Figure 4.12. For an increase in ϵN of 0.2 past the estimated ODT, the fraction of core blocks that are unassociated drops by $\approx 40\%$. While both the AB and BAB unimer fractions drops by $\approx 60\%$ for the same increase in ϵN . This suggests that while we are well into the stable BCC region for all chain architectures, the spherical micelles formed by the ABA chains are less stable than comparable AB and BAB micelles.

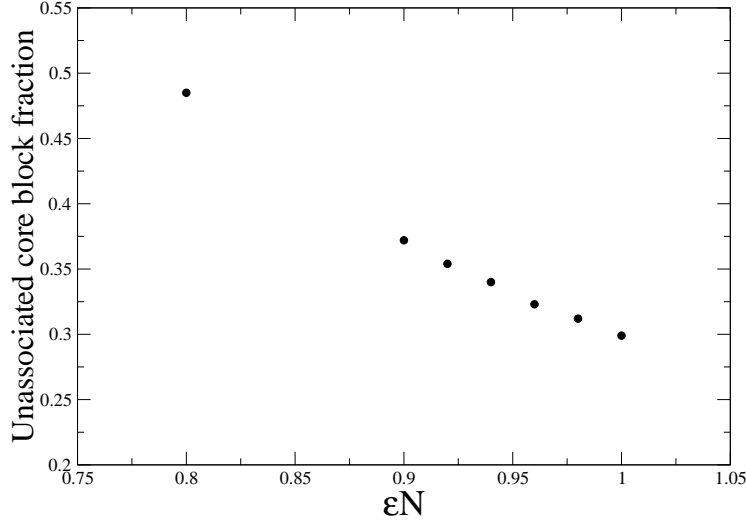


Figure 4.8: Fraction of unassociated core blocks present in simulations of symmetric ABA triblocks with chain length $N = 120$ and core monomer fraction $f_A = 0.2$. Each simulation was performed in a box of size $L = 30.4b$ and $L_0 = 15.2b$.

In Figure 4.9 the average micelle core volume V_{core} scaled by R_g is plotted as a function of segregation strength. We note here that since $N = 120$, the ABA R_g is a different scaling than the R_g used for both AB and BAB copolymers that have $N = 60$. As expected, as the segregation strength increases, so does the core volume. We also note here, that the average micelle core for the ABA triblocks are much smaller than that of the AB diblocks. As a result, we would expect for the enthalpic penalty of exposing a core block to the corona to be lower than the AB case. This follows from Reference [38] where the rate of chain exchange over a barrier for an activated process is proportional to $e^{-F/k_B T}$ where $F = F_{core} + F_{corona} + F_{interface}$ is the free-energy profile of the barrier between the core and corona [22]. The free energy profile of the barrier created at the core-corona interface is dependent on two terms: the free energy of the interface and the free energy of the corona [22]. The free energy of the core-corona interface is proportional to the surface area of the core-corona interface and therefore goes like $F_{interface} \sim R_{core}^2 \sim V_{core}^{2/3}$. Therefore it is reasonable to expect a faster rate of chain exchange for ABA triblocks as the micelle cores are smaller, leading to a smaller barrier

associated with exposing a core block to the corona.

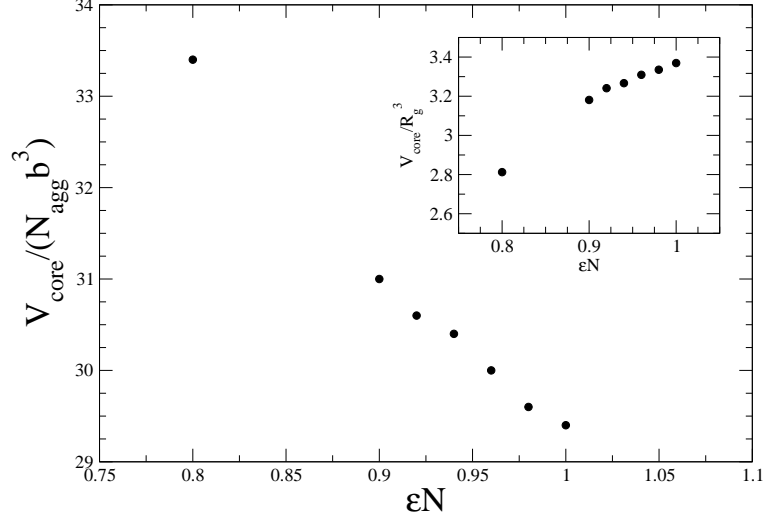


Figure 4.9: Average micelle core volume V_{core} scaled by $N_{agg}b^3$ as a function of segregation strength ϵN for symmetric ABA triblocks with chain length $N = 120$ and core monomer fraction $f_A = 0.2$. The inset graph shows V_{core} as a function of ϵN , without any scaling. Each simulation was performed in a box of size $L = 30.4b$ and $L_0 = 15.2b$.

4.1.3 BAB Triblock Copolymer Melt

Figure 4.10 shows a slice of the phase diagram for symmetric BAB triblock copolymers at a core monomer fraction of $f_A = 0.2$. The ODT between the DIS and BCC phase is roughly found at $\epsilon N = 0.7$ which is greater than the ODT for AB diblocks, but smaller than the ODT for ABA triblocks.

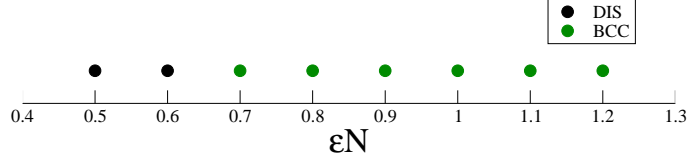


Figure 4.10: Slice of the phase diagram of symmetric BAB triblocks with chain length $N = 60$ and core monomer fraction $f_A = 0.2$. Each simulation was performed in a box of size $L = 25.8b$ with BAB triblock BCC period $L_0 = 12.9b$.

Comparison of the ratios of the ODTs of each architecture from equilibrium SCFT show us that our ODT values found using dSCFT are reasonable. Using SCFT calculations we found that, $(\chi N)_{ODT,ABA}/(\chi N)_{ODT,AB} \approx 2$ and $(\chi N)_{ODT,BAB}/(\chi N)_{ODT,AB} \approx 1.6$ at $f_A = 0.2$ while from our estimated values: $(\epsilon N)_{ODT,ABA}/(\epsilon N)_{ODT,AB} \approx 2$ and $(\epsilon N)_{ODT,BAB}/(\epsilon N)_{ODT,AB} \approx 1.75$. We also calculated the equilibrium BCC period using SCFT and found $L_{SCFT} = 11.4b$ for $\epsilon N = 1.0$ ($\chi N = 60$), corresponding to a 13.1% difference from the value used in our simulations.

We can characterize our BAB micelles in the same way we characterized AB and ABA micelles. Figure 4.11 shows the average aggregation number of micelles in the system as a function of segregation strength. The aggregation number increases as the segregation strength is increased, however for a given value of ϵN the aggregation number is larger than that of the ABA micelles but smaller than AB diblock micelles. Similar to the trend observed for the other chain architectures, we see the aggregation number begin to plateau at large segregation strengths.

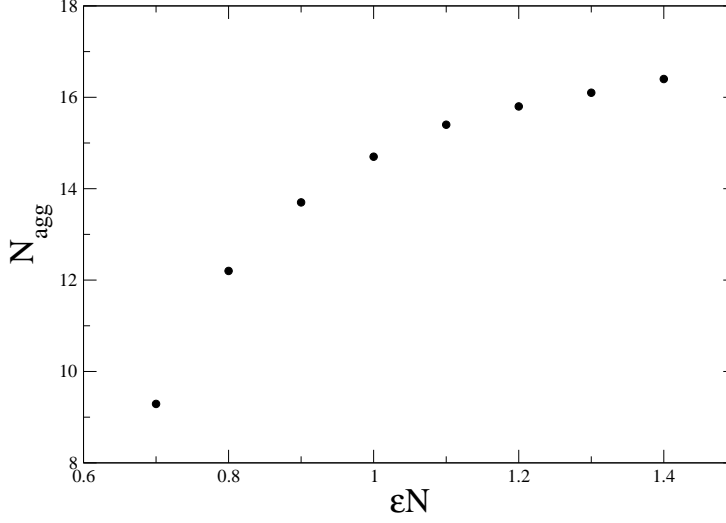


Figure 4.11: Average aggregation number of micelles formed in the BCC phase for symmetric BAB diblocks with chain length $N = 60$ and core monomer fraction $f_A = 0.2$. Each simulation was performed in a box of size $L = 25.8b$ with BCC period $L_0 = 12.9b$.

We expect to see similar results for the fraction of unimers present in our system as we saw for AB and ABA in Figures 4.4 and 4.8, respectively. Figure 4.12 does give the expected result where the unimer fraction f_{unimer} starts at a very high value for a weakly-segregated system and decreases rapidly until reaching a plateau at high values of ϵN .

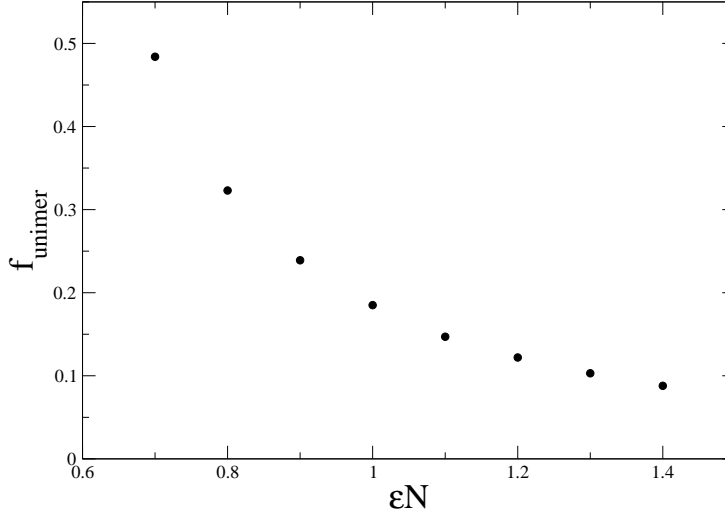


Figure 4.12: Fraction of unimers present in simulations of symmetric BAB diblocks with chain length $N = 60$ and core monomer fraction $f_A = 0.2$. Each simulation was performed in a box of size $L = 25.8b$ with BCC period $L_0 = 12.9b$.

As expected from our previous results, Figure 4.13 shows the average micelle core volume V_{core} increasing with segregation strength until reaching a plateau at strong segregation strengths. We would again expect the relationship $V_{\text{core}} \sim N_{\text{agg}} N_A b^3$ to hold when the system is highly segregated with a sharp boundary between the core and corona. For our highest segregation strength $\epsilon N = 1.4$, the ratio $V_{\text{core}}/(N_{\text{agg}} b^3) = 12.5$, which is again close to the expected value of $N_A = 12$. This result is unsurprising as the presence of "intruder" chains as mentioned above will contribute to the volume but not to the aggregation number as well as the presence of unimers in the system.

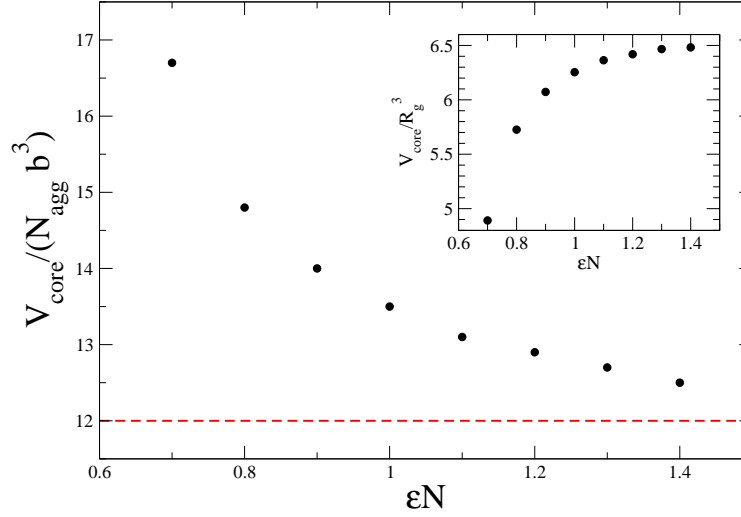


Figure 4.13: Average micelle core volume V_{core} scaled by $N_{agg}b^3$ as a function of segregation strength ϵN for symmetric BAB triblocks with chain length $N = 60$ and core monomer fraction $f_A = 0.2$. The inset graph shows V_{core} as a function of ϵN , without any scaling. The red dashed line shows the theoretical value of $V_{core}/N_{agg}b^3 = N_A = 12$ for strongly segregated systems. Each simulation was performed in a box of size $L = 25.8b$ with BCC period $L_0 = 12.9b$.

For BAB triblocks, we have also examined the potential for a general N dependence on the chain exchange kinetics and therefore we want to characterize the equilibrium properties for changing values of chain length N at fixed ϵN . Figure 4.14 shows the cross-section of average A-monomer densities along a one-dimensional slice in the (100) direction for the three chain lengths studied. We examine this monomer density profile to see if there is a change in the sharpness of the profile which may be associated with a change in the relaxation time associated with chain exchange as discussed previously and in Reference [22]. From Figure 4.14, the monomer density profiles for our simulations appear similar, from which we would expect to have little change in the chain exchange kinetics by varying the chain length of our triblocks, aside from the trivial overall scaling of the time-scale characterized by the Rouse time $\tau_R \sim N^2$.

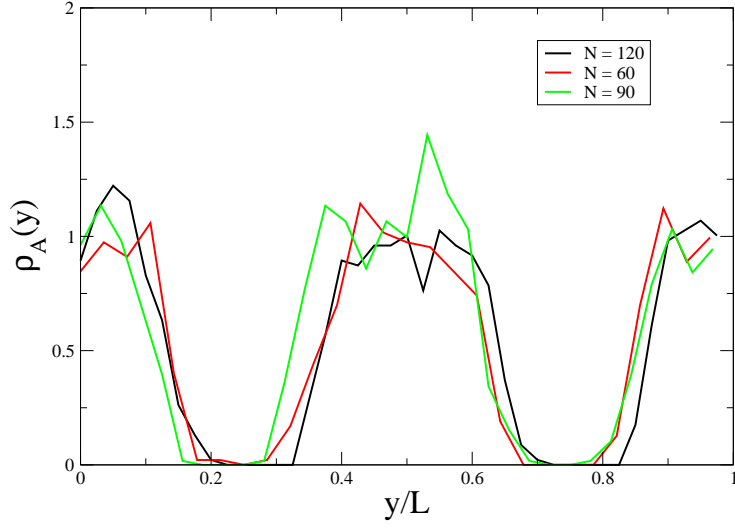


Figure 4.14: Cross-section through micelle centroids of average A-monomer densities in one-dimension along the (100) axis for varying chain lengths of BAB copolymers with $f_A = 0.2$ and fixed $\epsilon N = 1.2$. Box size $L = 2L_0$ is adjusted in the BCC phase for each chain length according to the scaling of $L_0 \sim N^{1/2}$ starting from $L_0 = 12.9b$ for $N = 60$.

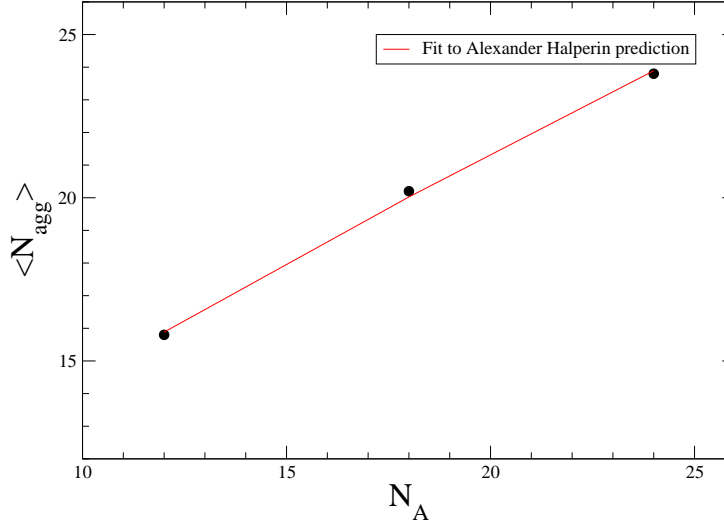


Figure 4.15: Average micelle aggregation number as a function of core block size for BAB chains of fixed core monomer fraction $f_A = 0.2$ at $\epsilon N = 1.2$. Each simulation was performed in a simulation box that is scaled according to $L_0 \sim N^{1/2}$, at $N_A = 12$ we have $L_0 = 12.9b$. Fit curve is plotted according to the predictions made in Reference [22] which predicts $N_{agg} \sim N_A^{4/5}$. A linear scaling $N_{agg} \sim N_A$ also provides an adequate fit as well due to the small number of data points.

As we are interested in the dependence of dynamic properties on chain degree of polymerization, we should also carefully examine the equilibrium properties to ensure that the system is behaving appropriately as we make changes to the chain length. Reference [22] has described the equilibrium properties of dilute diblock copolymer micelles in a highly selective solvent. While our system is a melt of triblock copolymer micelles, we have calculated that our aggregation number follows the same trends as predicted for the so-called "starlike" micelles where the corona block is longer than the core block. Figure 4.15 shows how the aggregation number of BAB micelles change as we increase the core block length at fixed $\epsilon N = 1.2$ and compare it to the scaling calculated in Reference [22].

It is also important to adjust our system size as we increase the chain length, while keeping a fixed number of unit cells in the simulation box. If this is not done, then our micelles will become stressed and their size will not be equal to the equilibrium micelle core

size in the stable BCC phase. From simple ideal chain scaling theory, as we increase N , we expect the core volume of our micelles to increase and also, by extension, the system size L .

To ensure that we are adjusting our box size appropriately we apply a simple scaling that states that the equilibrium BCC period should scale like $L_0 \sim R_g \sim \sqrt{N}$. In a well-segregated melt at fixed f_A and fixed number of unit cells, we can expect the volume of a micelle to follow $V_{core} = \frac{n_P N f_A b^3}{N_{mic}}$, where the number of polymers $n_P = \frac{L^3}{N b^3}$. Therefore the micelle core volume should scale like $V_{core} \sim L^3 \sim N^{3/2}$ for fixed N_{mic} . We plot this scaling in 4.16 and see that our results for the average micelle core agree with the predicted scaling relationship.

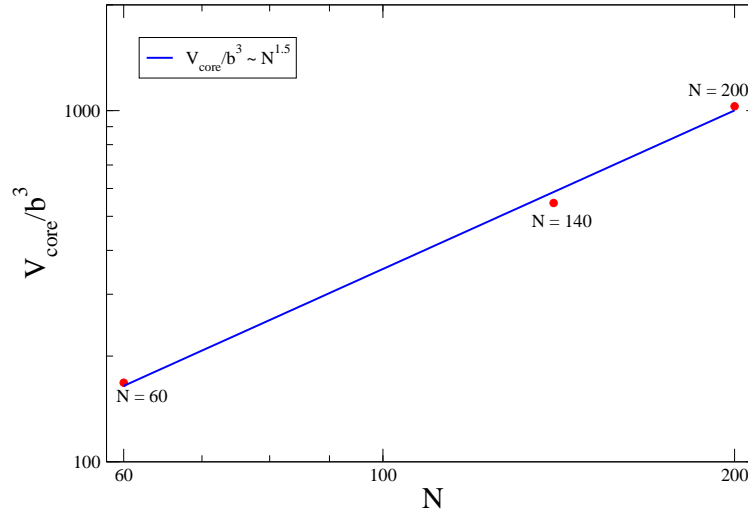


Figure 4.16: Scaling of BAB micelle core volume with chain length. The equilibrium period is varied according to the scaling $L_0 \sim N^{1/2}$ and we recover the predicted scaling of core size with chain length $V_{core} \sim N^{3/2}$. For each simulation, the chains have a constant core monomer fraction $f_A = 0.2$ and segregation strength $\epsilon N = 1.2$.

4.1.4 AB/ABA Copolymer Blends

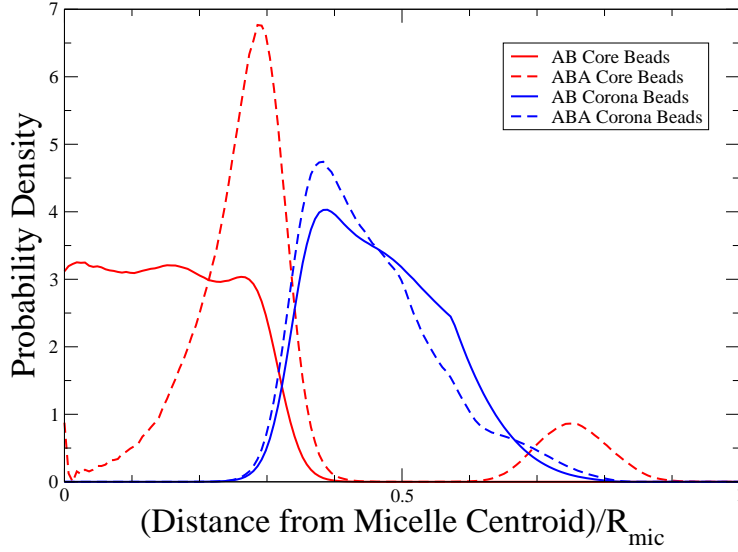
Using triblocks as tracer molecules allows for comparisons between the tracer molecule and the AB diblock that forms the micelle as it removes any ambiguity in the dynamics created

by different equilibrium properties of the micelles for melts of different block copolymer architectures that we observed in Sections 4.1.1 to 4.1.3. Figure 4.17 shows the radial distribution of the density of core and corona beads of AB and ABA copolymers relative to the micelle closest to the chain centre-of-mass for two different blends of AB diblocks and ABA triblocks. Figure 4.17a shows the distribution for chains of equal length N and core monomer fraction f_A , so each core block of the ABA copolymers is half of the length of the AB diblock core block. Figure 4.17b shows the distribution for the blend where the ABA triblocks are twice the length of the AB diblocks, $N_{ABA} = 120$. The core blocks of this ABA triblock are each equal in length to that of the AB diblocks in the blend. We also note that the radial probability distributions presented are individually normalized to unity, so that all features can be easily seen. In reality, the blends only contain a small amount of the tracer triblock, and if we were to normalize the entire dataset, the triblock distributions would be barely visible.

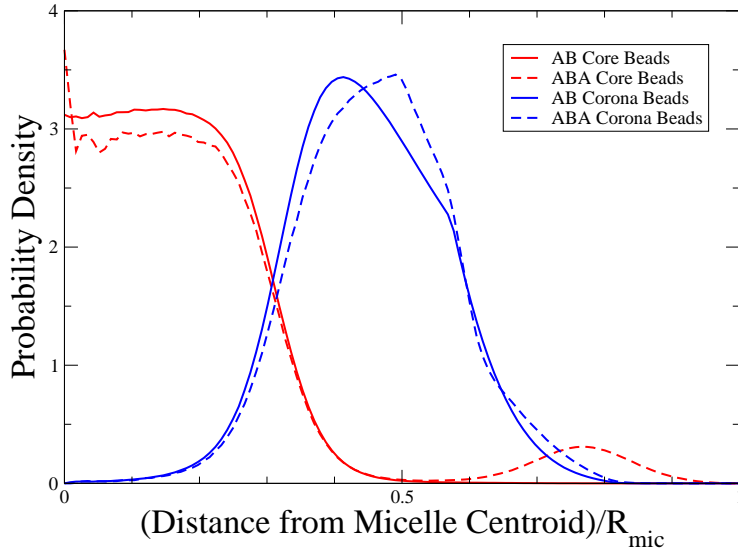
In both Figures 4.17a and 4.17b there is a bump in the probability density at the inter-micellar distance. This small bump is a result of core block bridging, where one core block is inserted in a micelle and the other is inserted in a neighbouring micelle. We also observe that for Figure 4.17a the probability of finding ABA beads close to the centre of the micelle core is very small. This is a result of the ABA core blocks in this blend being half of the length of the AB diblock core blocks which form the micelle core. When the core block lengths are the same, see Figure 4.17b where $N = 60$, the probability of finding ABA core beads inside the micelle core is relatively constant. The probability of finding an ABA core bead inside the micelle core is slightly lower than finding an AB core bead inside the core. This is because of the ABA core blocks bridging between micelles.

In both cases we observe a shoulder in the probability of finding a corona bead roughly halfway between micelles. This shoulder appears because we plot the probability of finding a bead at a distance from the micelle that is closest to the chains centre of mass. We would then expect a dip in the probability at $(1/2)R_{mic}$, which serves as a cut-off for how far away

a chain's centre of mass can be relative to the closest micelle. Beads can still be found past this cut-off as the cut-off only restricts the centre of mass, not individual beads.



(a) ABA triblocks with $N = 60$



(b) ABA triblocks with $N = 120$

Figure 4.17: Radial probability density distribution of beads relative to the micelle closest to its chain centre of mass. The distance from the micelle core is scaled by intermicellar distance $R_{mic} = \frac{\sqrt{3}}{2}L_0$. These blends consist of 5%, by number, ABA triblock copolymers with total core monomer fraction $f_A = f_{A1} + f_{A2} = 0.2$ with degree of polymerization (a) $N = 60$, (b) $N = 120$. Both cases have core monomer fraction $f_A = 0.2$ in a constant array of BCC-ordered micelles formed by AB diblocks ($f_A = 0.2$, $\epsilon N = 1.2$). These simulations were performed in a single BCC unit cell with period $L_0 = 18b$, corresponding to the equilibrium AB diblock period for $\epsilon N = 0.8$ used in Section 4.1.1.

4.1.5 AB/BAB Copolymer Blends

Figure 4.18 shows the radial density distribution for BAB tracer (5% by number) triblocks and AB diblocks that form BCC-ordered spherical micelles. The tracer triblocks have the same degree of polymerization N and core monomer fraction f_A as the AB diblocks, however the corona blocks of the BAB copolymers then are half the length of the corona blocks of the AB copolymers. The key feature in Figure 4.18 is that despite being the same length, the core blocks don't penetrate to the centre of the micelle as they are forced to loop through the core because of the second corona block junction which lies on the surface of the micelle core. Because of the looping, the BAB chains are forced to be closer to the micellar interface than the AB chains, which, as we later see, will allow the BAB core blocks to extract from the core more readily than the AB core blocks.

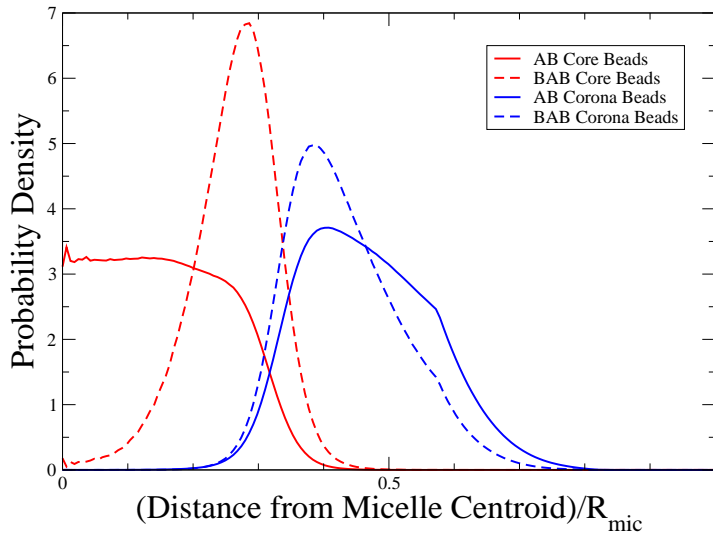


Figure 4.18: Radial probability density distribution of beads relative to the micelle closest to its chain centre of mass. This blend consists of 5%, by number, BAB triblock copolymers in a constant array of BCC-ordered micelles formed by AB diblocks. Both the tracer triblocks and the diblocks have degree of polymerization $N = 60$, core monomer fraction $f_A = 0.2$ and segregation strength $\epsilon N = 1.2$. This simulation was performed in a single BCC unit cell with period $L_0 = 18b$, corresponding to the equilibrium AB diblock period for $\epsilon N = 0.8$ used in Section 4.1.1.

Another feature we note is that BAB corona beads on average are closer to the core-corona interface than the AB corona beads. This can be explained by the looping of the core block as well as the shortened BAB corona blocks. Reference [28] shows a similar distribution for B_1AB_2 and AB_1B_2 tracer triblock core beads in an array of micelles formed by AB diblocks. For B_1AB_2 triblocks, we see the same behaviour as the density of core beads is negligible at the centre of the micelle core, here and in Reference [28].

4.2 Dynamical Properties

In this section, we present the results of our simulations that pertain to the dynamics of chain exchange for the various chain architectures studied.

4.2.1 AB Diblock Copolymer Melt

For each chain architecture (AB, ABA or BAB) studied, we calculate the chain relaxation time as a function of segregation strength. Figure 4.19 shows the contrast function $C(t)$, Equation (3.47), for various segregation strengths for AB diblock copolymers. The details of how $C(t)$ is calculated were presented in Section 3.2.3. From Figure 4.19, we can see that as ϵN is increased, the decay rate of $C(t)$ decreases, corresponding to an increase in the relaxation time. Extracting the relaxation time from these curves is accomplished by fitting the exponential region (the linear region of the log-linear plot in Figure 4.19) of the data to a single exponential $C(t) \sim \exp(-t/\tau)$. The exponential region is chosen by dropping the first $\sim 10\tau_R$ such that the initial non-exponential decay is not considered. We also exclude the late time data, in this case $t \gg 50\tau_R$, when the chains are fully mixed and $C(t)$ fluctuates about this final state. The chain exchange relaxation time τ for each of these curves is then extracted and plotted as a function of ϵN .

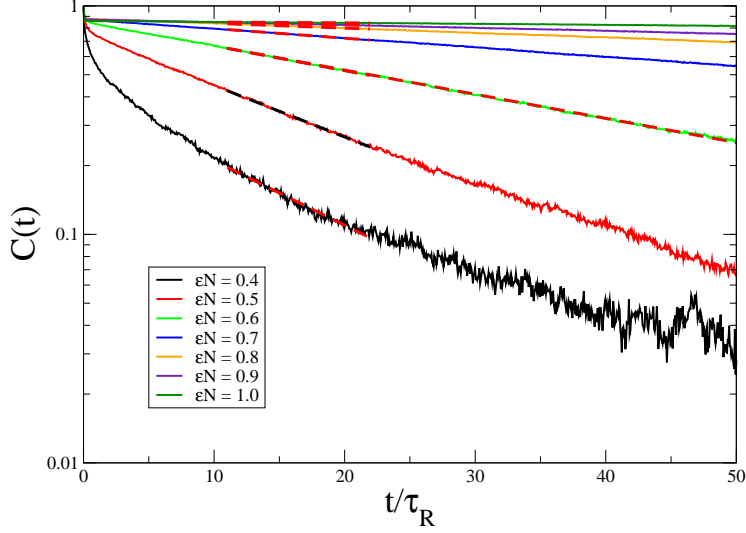


Figure 4.19: Log-linear plot of the contrast function $C(t)$ as a function of time (in units of Rouse time τ_R) of asymmetric AB diblocks with chain length $N = 60$ and core monomer fraction $f_A = 0.2$ for various segregation strengths ϵN . Each simulation was performed in a box of size $L = 36.4b$ with $L_0 = 18.2b$.

The extracted relaxation times are shown in Figure 4.20 as a function of ϵN . The final result is an exponential (linear when plotted using a log scale) curve in ϵN that is expected according to the current theory [20],

$$\frac{\tau(N)}{\tau_R(N)} = \exp(\alpha_\tau f_A \epsilon N), \quad (4.1)$$

which implies that the chain exchange relaxation time $\tau(N)$ is exponentially dependent on the segregation strength $\epsilon N_{core} = \epsilon N f_A$. The physical significance of this exponential relationship is that removing the core block from the micelle core is an activated process. That is, it is essentially Kramer's barrier hopping problem discussed in Section B. The blue data point at $\epsilon N = 0.4$ in Figure 4.20 shows the relaxation time when the system's BCC period is corrected from $L_0 = 18.2$ to $L_0 = 15.7b$ for $\epsilon N = 0.4$ using the method outlined in 3.2.1. The overestimations made at weak segregation strength are expected as we don't decrease the BCC period, therefore the micelles become stretched and therefore have a slower

relaxation time as chain extraction rate is proportional to $e^{-F/(k_B T)}$ and the free-energy F increases with micelle core size $F_{interface} \sim V_{core}^{2/3}$ as discussed in Section 4.1. From our fit to the data we can extract the dimensionless constant α_τ which characterizes how the quickly the relaxation increases as a function of ϵN . From the AB diblock simulation we find that the constant is $\alpha_\tau \approx 49.2$. We will compare this value later to the values found for each of the triblock architectures.

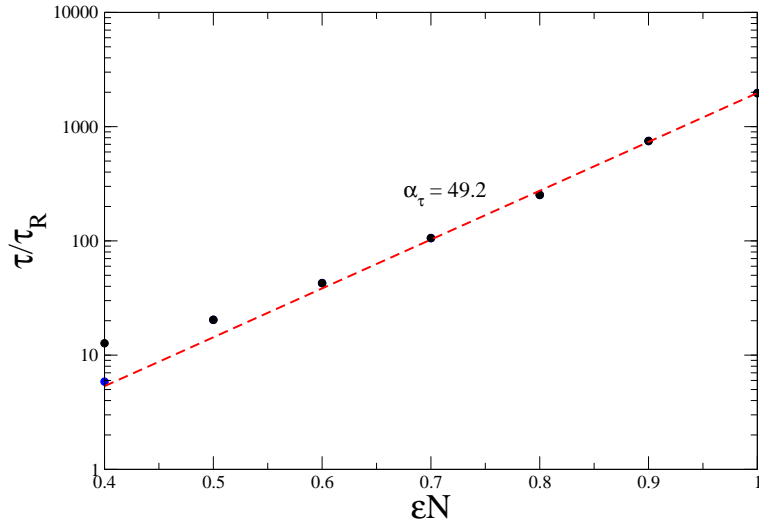


Figure 4.20: Relaxation time as a function of segregation strength ϵN for AB diblock copolymers with fixed core monomer fraction $f_A = 0.2$ and fixed degree of polymerization $N = 60$. τ scales exponentially with increasing interaction strength ϵ . Data points at weak segregation strength are overestimations due to a mismatch in the simulation box size and the preferred BCC period. Each simulation was performed in a box of size $L = 36.4b$ and $L_0 = 18.2b$, corresponding to the BCC period used for $\epsilon N = 0.8$, with the exception of the blue datapoint which has a BCC period of $L_0 = 15.7$, the equilibrium period used for $\epsilon N = 0.4$.

Another way to characterize the rate at which chains move throughout the system is by calculating the chain self-diffusion coefficient. Chain self-diffusion along any axis should obey the following equation for 1D diffusive motion:

$$\langle \Delta R_\alpha(t)^2 \rangle = 2D_\alpha t, \quad (4.2)$$

where $\alpha = x, y$ or z , $\Delta R_\alpha(t) = R_{cm,\alpha}(t) - R_{cm,\alpha}(0)$ represents the change in the chain centre of mass position along the α axis and D_α is the diffusion coefficient for the given axis and can be calculated from the slope of the MSD data. We note that the BCC phase is isotropic and therefore the diffusion coefficient along any axis is given by $D_\alpha = D$. We can determine if AB diblocks in the BCC phase are undergoing diffusive motion by observing the MSD plots given in Figure 4.21. From the phase diagram slice presented in Figure 4.1, our system is in the disordered phase at $\epsilon N = 0.3$ where motion is purely diffusive, $D = D_0 = \frac{k_B T}{N \zeta}$. This purely diffusive behaviour can be seen as the MSD data for $\epsilon N = 0.3$ is a straight line whose slope is $2D_0$. We note that as ϵN is increased such that our system is in the BCC phase, there is a suppression of the diffusive motion at long time scales while at short time scales $t < \tau_R$ the curves follow the purely diffusive behaviour observed at $\epsilon N = 0.3$. At short times, the motion of the chains is on length-scales that are much smaller than the radius of the micelle core (ranging between $1.45R_g$ and $1.65R_g$ for the values of ϵN that we simulate) allowing for the chain to diffuse freely in any direction for this length-scale as the core block does not have to pay the enthalpic penalty associated with exposing the core block to the corona.

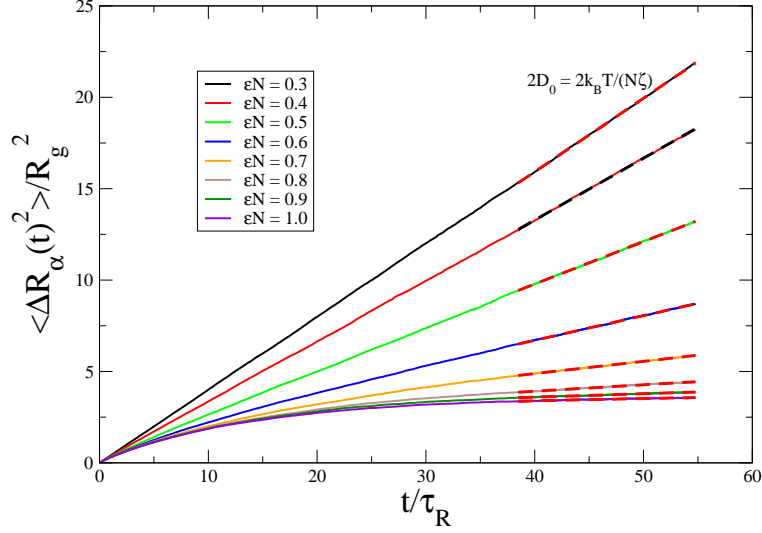


Figure 4.21: Mean-squared displacement curves of AB diblocks with chain length $N = 60$ and core monomer fraction $f_A = 0.2$ for various segregation strengths ϵN . Each simulation was performed in a box of size $L = 36.4b$ and $L_0 = 18.2b$.

At long times, where the motion of the chains is on length-scales greater than the micelle core radius ($\Delta R_\alpha > 1.65R_g$), our chains diffuse by "hopping" over the energy barrier associated with exposing a core block to the corona. This is now Kramers barrier-hopping problem as described in Section B and discussed in Reference [38]. At these length-scales, the motion is still diffusive but is exponentially suppressed, as we show in Figure 4.22, by the height of the energy barrier. The diffusion coefficient in this regime is proportional to the hopping rate and therefore has an exponential dependence on the barrier,

$$\frac{D}{D_0} \sim \exp(-\alpha_D f_A \epsilon N). \quad (4.3)$$

We can observe this exponential suppression by taking the slope of our MSD data at long times in the linear regime (where chain motion is diffusive) and plotting the diffusion coefficient as a function of ϵN . This is done in Figure 4.22, where we plot on a log-linear scale the diffusion coefficient relative to the disordered phase diffusion coefficient D_0 as a function

of ϵN .

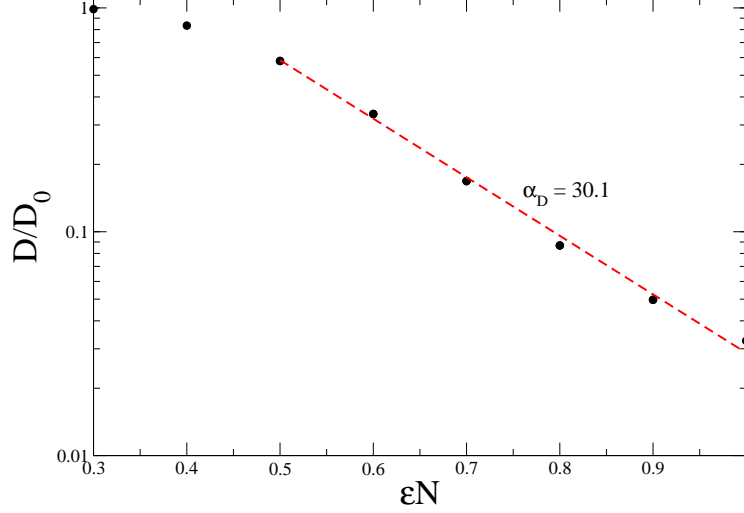


Figure 4.22: Diffusion coefficients as a function of segregation strength ϵN for the BCC phase of asymmetric AB diblock copolymers with chain length $N = 60$ and $f_A = 0.2$. Exponential suppression of the diffusion coefficients is observed. Each simulation was performed in a box of size $L = 36.4b$ and $L_0 = 18.2b$.

4.2.2 ABA Triblock Copolymer Melt

Figure 4.23 shows the chain exchange relaxation times extracted from exponential fits to the contrast function $C(t)$ following the same procedure as outlined in Section 4.2.1. The data shows an exponential fit with a much smaller slope than found for AB diblocks with the same core monomer fraction $f_A = 0.2$, that is $\alpha_{\tau,ABA} = 8.4$ compared to $\alpha_{\tau,AB} = 49.2$. According to the theory and results presented in Reference [5], this is an unexpected result as ABA triblocks should exchange at a much slower rate than AB diblocks. However, the data presented in Figure 4.23 shows the core block exchange relaxation time as opposed to the chain exchange relaxation time. The algorithm used to track core blocks in our simulations treats each core block as a separate identity, meaning that each chain contains two labels, one for each core block. The extent of chain mixing is then dependent on the label of the core

blocks compared to its associated micelle. We also note that this discrepancy can be further attributed to the possibility of one core block dangling outside of the micelle core while the other core block is anchored to the micelle, increasing the rate of core block expulsion [5]. Furthermore, the micelles in our ABA simulations are on average much smaller than those found in the AB diblock simulations, see Sections 4.1.1 and 4.1.2. According to Kramers barrier-hopping problem, the rate of hopping is proportional to the exponential of the free energy of the barrier, which is directly related to the size of the micelle core as discussed previously in Section 4.1. Therefore, we would expect a significant increase in the chain exchange rate as the ABA micelles are much smaller than the AB micelles.

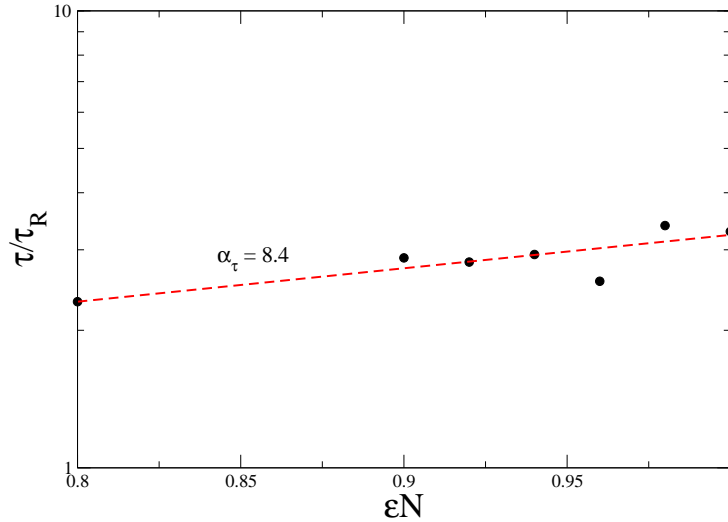


Figure 4.23: Relaxation time as a function of segregation strength ϵN for ABA triblock copolymers with fixed core monomer fraction $f_A = 0.2$ and fixed degree of polymerization $N = 120$

Similar to the fast chain exchange rate found from the contrast function for ABA, we find the diffusion coefficients experience a much smaller suppression than that for the AB diblocks, $\alpha_{D,ABA}/\alpha_{D,AB} \approx 0.2$. This can be seen in Figure 4.24, and can be explained by the difference in each architectures equilibrium properties as discussed previously.

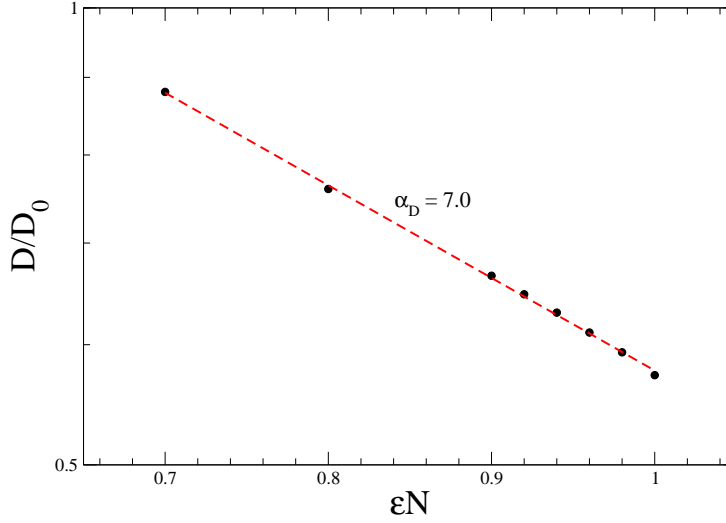


Figure 4.24: Diffusion coefficients as a function of segregation strength ϵN for the BCC phase of symmetric ABA triblock copolymers. Exponential suppression of the diffusion coefficients is observed.

4.2.3 BAB Triblock Copolymer Melt

For BAB triblocks, we also test for a general chain length dependence of chain exchange relaxation time at constant segregation strength. According to Equation (4.1) there should be no N dependence if ϵN is held constant. That is, by decreasing ϵ while increasing N we should observe a constant chain exchange relaxation time. Following the scaling relationships presented in Section 4.1.3 we appropriately adjust the BCC period L_0 for each value of chain length N .

The extracted results for τ as a function of chain degree of polymerization are plotted in Figure 4.25 which shows that despite the prediction of Equation (4.1), we do see the relaxation time increase as the degree of polymerization increases. This, however, does not necessarily imply that Equation (4.1) is incorrect, it may be asymptotic. Figure 4.25 could potentially reach a plateau for larger values of N which might suggest that there are finite chain length effects that become negligible at large enough chain lengths.

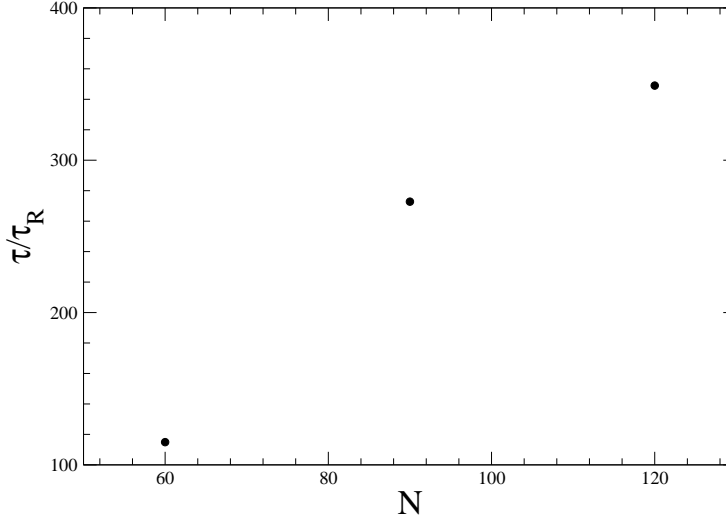


Figure 4.25: Relaxation times for BAB copolymers with $f_A = 0.2$ and $\epsilon N = 1.2$ in the BCC phase extracted from an exponential fit to the corresponding contrast function. Surprisingly we see a dependence of the relaxation time on the degree of polymerization N which is not predicted by Equation (4.1). Each simulation is performed in a box containing 8 unit cells that is adjusted in size from $L_0 = 12.93b$ for chains with $N = 60$ according to the scaling $L_0 \sim N^{1/2}$.

Equation (4.1) also predicts an exponential relationship between τ and the segregation strength ϵN , which we observed for AB and ABA copolymers. Figure 4.26 shows the chain exchange relaxation time for BAB copolymers as a function of segregation strength. All simulations were performed with a BCC period of $L_0 = 12.93b = 4.1R_g$. Near the ODT, we see an overestimation of the chain exchange relaxation time due to the BCC period not being optimized, which stretches the micelles leading to an increase in the relaxation time.. The effect however is small and the exponential dependence is still observed around $\epsilon N = 1.2$.

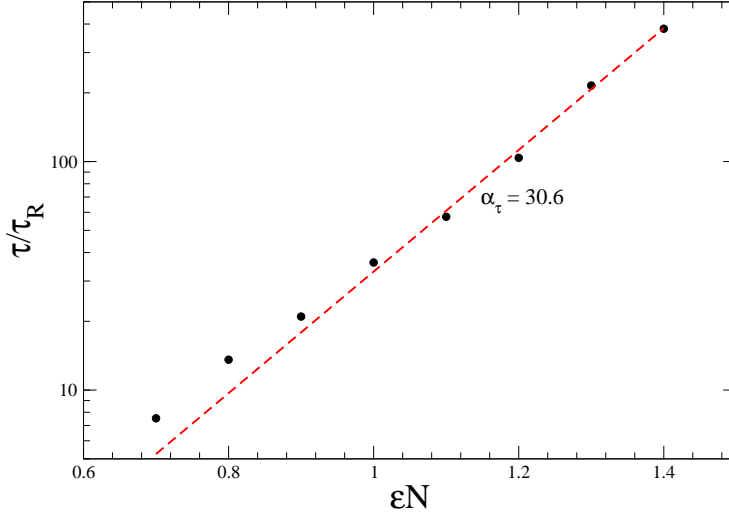


Figure 4.26: Relaxation time as a function of segregation strength ϵN for BAB triblock copolymers with fixed core monomer fraction $f_A = 0.2$ and fixed degree of polymerization $N = 60$. τ scales exponentially with increasing interaction strength ϵ . We suspect data points at weak segregation strength, based on our experience with AB diblocks, are overestimations due to a mismatch in the simulation box size and the preferred BCC period. Each simulation was performed in a box of size $L = 25.8b$ with BAB triblock BCC period $L_0 = 12.9b$.

Figure 4.27 shows the diffusion coefficients extracted from a linear fit to late-time MSD data plotted as a function of ϵN . As expected, we observe an exponential suppression of the diffusion coefficient as we increase the segregation strength. Compared to AB diblocks, we see a smaller degree of suppression, $\alpha_{\tau,BAB}/\alpha_{\tau,AB} \approx 0.7$, as well the normalized diffusion coefficients are greater for each value of ϵN meaning that BAB copolymers are diffusing faster throughout the system at any given ϵN . This can again be explained by the difference in the equilibrium properties of the two architectures. The average micelle core for BAB copolymers is smaller than the average AB micelle core, as shown in Figures 4.13 and 4.5, leading to faster chain diffusion. As well we note that the degree of suppression of D for ABA copolymers is much smaller than that for BAB copolymers, as BAB micelles are, according to our micelle structure results, larger than ABA micelles.

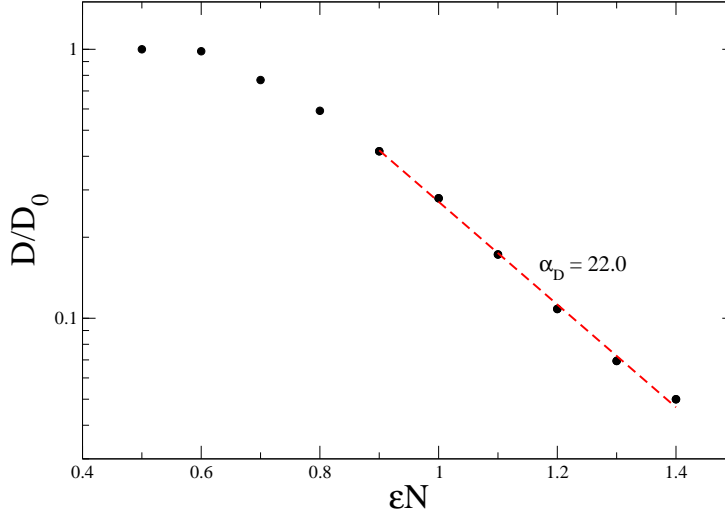


Figure 4.27: Diffusion coefficients as a function of segregation strength ϵN for the BCC phase of symmetric BAB triblock copolymers with $N = 60$ and $f_A = 0.2$. Exponential suppression of the diffusion coefficients is observed. Each simulation was performed in a box of size $L = 25.8b$ with BAB triblock BCC period $L_0 = 12.9b$.

4.2.4 AB/ABA Copolymer Blends

A direct comparison between the diffusion coefficients of AB diblocks and ABA diblocks in a blend allow us to make direct comparisons between chain exchange rates for the different chain architectures studied. As both copolymers are evolving inside the system, the micelle structure is the same for both copolymers and is determined by the AB diblock copolymers as they make up the majority of the blend. Therefore the only effect on chain diffusion should come from the difference in chain architecture, not the equilibrium structure. We note that we can compare the diffusion coefficient of ABA triblocks to AB triblocks at segregation strengths where ABA triblocks don't normally order into BCC spheres (see Figure 4.6) as the majority AB diblocks determine the BCC ordering of the blend. Figure 4.28 shows the diffusion coefficients of a blend consisting of 95% by number AB diblock copolymers with chain length $N = 60$ and 5% by number ABA triblock copolymers with chain length

$N = 120$. Both copolymers have a core monomer fraction of $f_A = 0.2$, such that the individual ABA core blocks are equal in length to that of the AB copolymers at $N_A = 12$. For all values of ϵN , the diffusion coefficient of the tracer ABA polymers are suppressed to a greater extent than the AB diffusion coefficients, $\alpha_{D,ABA}/\alpha_{D,AB} \approx 1.9$. As the diffusion coefficient is proportional to the rate of hopping, as shown by Barrat and Fredrickson [44], ABA core blocks extract from the micelle core at a slower rate than AB diblocks while evolving in the same environment. As the core blocks for both copolymer architectures have the same length, Equation (4.1) would suggest that both architectures have the same chain exchange relaxation time and therefore the same rate of extraction. The presence of the second core block in ABA triblocks introduces a rate-limiting step in that both core blocks need to extract before a chain can exchange between micelles and diffuse. This result of slower chain exchange for ABA triblocks was also observed in TR-SANS experiments [5] for copolymers forming spherical micelles in a selective solvent. We note that we did not directly measure the chain exchange relaxation time for the tracer ABA triblocks as they only make up 5% of the blend.

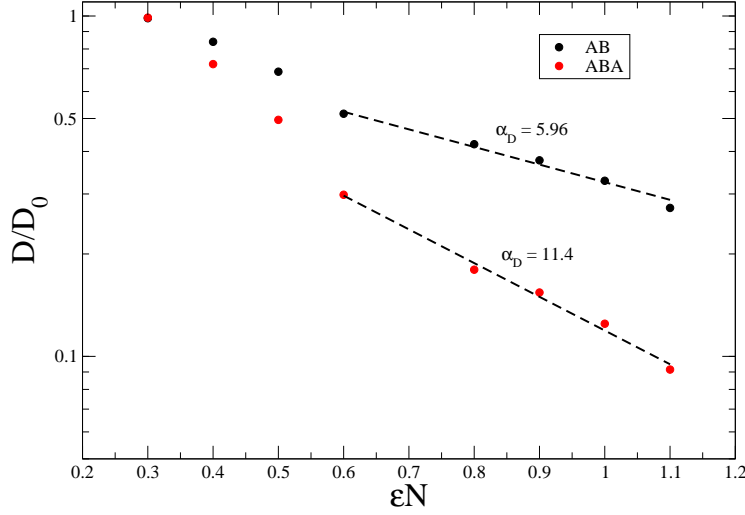


Figure 4.28: Diffusion coefficients as a function of segregation strength ϵN for 5% by number ABA triblocks of length $N = 120$ in a constant array of BCC-ordered spherical micelles formed by AB diblocks of length $N = 60$. Both copolymers have the same core monomer fraction $f_A = 0.2$, and therefore the same core block length for both copolymers. We note that the longer overall chain length of the ABA copolymers is normalized out of the dynamics by scaling the diffusion coefficients by $D_0 = \frac{k_B T}{N \zeta}$.

4.2.5 AB/BAB Copolymer Blends

Figure 4.29 shows the results of tracer diffusion simulations on a blend of 95% AB diblocks and 5% BAB triblocks, both with chain length $N = 60$ and core monomer fraction $f_A = 0.2$. For every value of ϵN in the ordered BCC phase, the degree of suppression of BAB diffusion coefficients is less than that of the AB diblocks, $\alpha_{D,BAB}/\alpha_{D,AB} \approx 0.75$. Therefore, BAB chains are exchanging between micelles at a faster rate than the AB diblocks. The current theory, Equation (4.1) states that BAB triblocks should have the same chain exchange relaxation time as AB diblocks, meaning that the rate of chain exchange should be equal as well. However, the BAB triblocks are observed to be faster, which can be explained by what we observe in Figure 4.18. In this figure, we see that BAB core beads are more likely to be closer to the micelle interface due to the looping of the core block, and therefore are

more readily able to extract from the micelle core. Again, we note that we can compare the diffusion coefficient of BAB triblocks to AB triblocks at segregation strengths where BAB triblocks don't order into BCC spheres (see Figure 4.10) as the majority AB diblocks determine the BCC ordering of the overall blend.

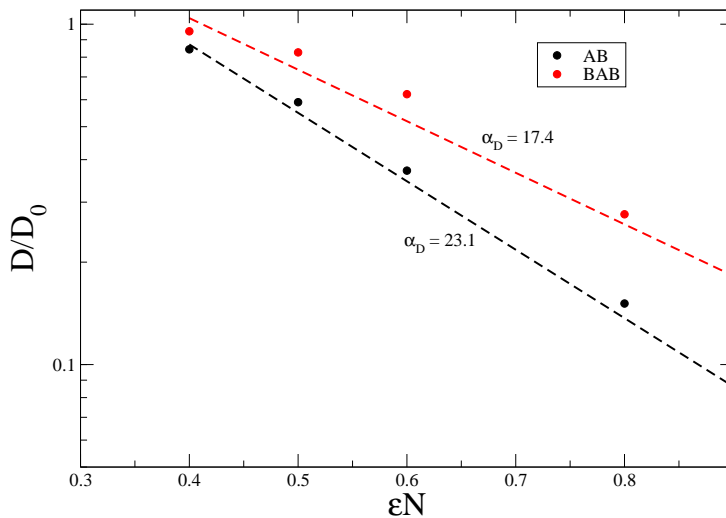


Figure 4.29: Tracer diffusion coefficients as a function of segregation strength ϵN for 5% by number BAB triblocks in a constant array of BCC-ordered spherical micelles formed by AB diblocks. Both copolymers have the same core monomer fraction $f_A = 0.2$ and overall chain length $N = 60$.

Chapter 5

Conclusion

The dynamical self-consistent field theory developed by Grzetic et al. has been extended to melts of symmetric ABA and BAB triblock copolymers and used to computationally study the kinetics of equilibrium chain exchange between BCC-ordered micelles for AB, ABA and BAB block copolymer melts. We have also generalized the computational method used for evolving Rouse modes for any value of chain length N through the use of a padded mixed-radix FFT to allow for systematic variations of chain length without the restriction of $N = 2^k$ where k is a positive integer. We have also extended dSCFT from a melt of a single species of block copolymer to the case of a blend of multiple species of block copolymers, in particular AB/ABA and AB/BAB blends.

Using dSCFT we have characterized several equilibrium properties for the systems studied including micelle size, average aggregation number and unimer fraction. Micelle properties have been well-characterized for all architectures studied. In particular, the aggregation numbers and segregation have been well-characterized as they have a strong bearing on the exchange kinetics. The BCC period values used in Chapter 4 were the result of an ad hoc approach that lacks physical interpretation, however the values should give qualitatively accurate results. The quantitative results however, may vary. In fact, from the equilibrium periods calculated using SCFT, I believe that our results for chain exchange relaxation times

are skewed to higher values as we used equilibrium periods that stretch our micelles, leading to an increase in the core-corona interface surface area. As such, future work can be done to accurately and efficiently determine L_0 using a thermodynamic route such that L_0 can be easily determined for every chain length N and segregation strength ϵN studied.

We have identified a potential method for future work to calculate the equilibrium BCC period using dSCFT, that is similar to the method used in equilibrium SCFT. Equilibrium SCFT calculates the free energy at three different periods and fits a parabola to the result and calculates the minimum free energy and its corresponding equilibrium period. Similarly, we propose that we can instead minimize the effective action L in the limit of long times, given by Equation (2.28), using the same procedure. The effective action is a function of the equilibrium period and therefore the largest contribution to the dynamical partition function should correspond to the period that minimizes the action at late times. The long time limit of dSCFT can be shown to converge to equilibrium SCFT [45], therefore calculating the action at long times of our simulation for at least three different periods near the correct value should allow us to perform the same procedure used in SCFT to calculate the period.

Phase diagrams for AB, ABA and BAB polymer melts have been calculated using dSCFT. The AB diblock phase diagram reproduces the previous phase diagram calculated using dSCFT in Reference [10], while all three phase diagrams are in accord with literature results [23, 24, 25]. We have found, similar to SCFT calculations, that at $f_A = 0.2$ ABA triblocks transition from the DIS phase to the BCC phase at a segregation strength that is twice that of the AB copolymer melt ODT segregation strength. The ODT segregation strength for the BAB copolymer melt is found to be between the ODT segregation strengths for AB and ABA melts, a result that is also seen in SCFT calculations. While this work focuses on the BCC phase as well as the order-disorder transition between the DIS and BCC phases, finding the phase boundary between the BCC and HEX phases is a future step in identifying the entire stable BCC region.

Micelles formed in the ABA triblock copolymer melt are found to have a smaller core

volume V_{core} and smaller average aggregation number when compared to the micelles formed by AB diblocks at the same core monomer fraction $f_A = 0.2$. We note here that, for the purpose of comparison, each core block studied (ABA or BAB) is the same length as that of the AB core block studied. As well, by comparing the fraction of unimers present in both the ABA and AB melts, the ABA micelles are found to have weaker segregation than the AB micelles, suggesting that the ABA micelles are less stable. Similar to the trends found for the ODT segregation strengths, we find that BAB micelles have an average aggregation number N_{agg} that is intermediate to the aggregation numbers found for AB and ABA micelles.

We have additionally studied equilibrium properties of the BAB copolymer melt at a fixed segregation strength ϵN and core monomer fraction f_A while adjusting the chain length of the polymer. We have observed appropriate scaling relationships for the average aggregation number and micelle core volume as a function of chain length. The interfacial profile of the BCC-ordered micelles in the BAB melt do not appear to be significantly influenced by a change in chain length at a fixed segregation strength.

We have also characterized properties of exchange dynamics for our melts and blends. For the AB, ABA and BAB melts, we have computed the contrast function $C(t)$ that measures the extent of chain exchange in the melt using dSCFT. For each melt, the chain exchange relaxation time τ is extracted from exponential fits to $C(t)$ curves for various segregation strengths that order the melts into the BCC phase. As predicted by the current theory of core block expulsion from a micelle core being an activated process, we observed an exponential dependence of the relaxation time associated with chains moving on the length scale of the intermicelle separation for AB, ABA and BAB copolymers melts. The AB diblock copolymer melt is found to have the largest relaxation times relative to the AB ODT segregation strength while the ABA melt has the smallest.

Further evidence of chain exchange being an activated process can be seen by the exponential suppression of the diffusion coefficient with increasing interaction strength in the diffusive motion regime at time scales at which chains are exchange between micelles. Ac-

According to Kramers barrier hopping problem, the rate of particle exchange across a barrier is related to the exponential of the energetic barrier. As the diffusion coefficients are proportional to this rate, we expect this exponential suppression and is evidence supporting chain exchange being an activated process. In particular, we can also see how the suppression varies for AB, ABA and BAB copolymer architectures. The current theory on chain exchange as an activated process only states that the relaxation time associated with chain exchange depends on the interaction strength ϵ and the length of the core block N_A of the polymer. However, we observe a smaller degree of exponential suppression for both ABA and BAB triblocks than that of AB diblocks despite having the same core block length. The results for both the centre-of-mass diffusion coefficients and the chain exchange relaxation times are an indication of a connection between equilibrium structure and chain exchange kinetics, as they follow the trends found for the equilibrium micelle properties relating to the stability of the micelles.

Due to the differences in equilibrium micelle properties in pure melts of AB, ABA and BAB copolymers, it is difficult to make a comparison between chain exchange kinetics with reference to the different architectures. Therefore, to eliminate the effect of variations in micelle size and segregation on comparisons between chain architectures, we performed tracer simulations where a small amount of tracer triblocks were placed in an array of AB diblocks forming BCC-ordered spherical micelles. The micellar structure of AB/ABA and AB/BAB blends were observed through the use of a bead probability density distribution for both core and corona blocks. The key differences between the two micellar structures for the $N = 120$ ABA tracer triblocks and $N = 60$ BAB tracer triblocks are that the ABA triblocks are bridging between two neighbouring micelles while the BAB tracer copolymers are localized to the surface of the micelle core, which has implications on the chain exchange dynamics.

For our blends we characterize the dynamics by calculating the centre-of-mass diffusion coefficients of both the tracer triblocks as well as the diffusion coefficients of the majority AB diblocks. As the micelle ordering is determined by the AB diblock, we expect that any

difference in the diffusion coefficients can be attributed to architecture differences. We find that the diffusion coefficient for the tracer ABA triblocks are suppressed to a greater extent than the AB diblocks. The prefactor α_D for the ABA triblock is roughly twice that of the AB diblock. We interpret this result as a direct consequence of the presence of the second core block in the ABA triblock. For the AB/BAB blend, we find that the tracer BAB triblocks experience a smaller suppression of the diffusion coefficients with increasing ϵN compared to the AB diblocks in the blend. We interpret this result as a consequence of the BAB core block looping through the micelle core. This looping localizes the BAB core block to the micelle core-corona interface, lowering the energetic barrier for expulsion from the core.

Appendix A

Discrete Cosine Transform

In order to evolve our ensemble of polymers using the Langevin equation as discussed within this thesis, we can diagonalize the spring force operator and solve the equation using Rouse modes. Previously, the numerical method took advantage of a fast cosine transform described in Numerical Recipes which required the degree of polymerization N to be a power of 2. However, we are interested in studying systematically how our system properties are affected by chain properties such as N . Therefore it is useful to use a transform method that can be solved efficiently for a dataset of arbitrary length. Such mixed-radix routines have been designed in several open-source packages such as the widely used GSL library. Another complication is that the GSL transform package does not contain the required cosine transform that is required by our equation. It is possible to make use of the mixed-radix fast Fourier transforms to achieve the appropriate cosine transform.

To start, we will define the $2N$ -point discrete Fourier transform (DFT) of a dataset $y(n)$:

$$Y(k) = \sum_{n=0}^{2N-1} y(n) W_{2N}^{nk}, \quad (\text{A.1})$$

where W_M is defined as

$$W_M = e^{2\pi i/M}. \quad (\text{A.2})$$

Next, we consider a dataset $x(n)$ of size N . In our simulations this dataset is the position of a replica chain's beads along one axis. The N -point discrete cosine transform (DCT) can be derived from the DFT of a $2N$ -point even extension of $x(n)$. Let $y(n)$ be the $2N$ -point even extension of $x(n)$:

$$y(n) = \begin{cases} x(n), & 0 \leq n \leq N-1 \\ x(2N-n-1), & N \leq n \leq 2N-1. \end{cases} \quad (\text{A.3})$$

We can now replace $y(n)$ in Equation A.1 with Equation A.3 such that

$$Y(k) = \sum_{n=0}^{N-1} x(n) W_{2N}^{nk} + \sum_{n=N}^{2N-1} x(2N-n-1) W_{2N}^{nk}. \quad (\text{A.4})$$

The second summation in Equation A.4 can be rewritten as a summation over the same indices as the first summation by changing the summation variable using $n = -m + 2N - 1$ which then gives

$$Y(k) = \sum_{n=0}^{N-1} x(n) W_{2N}^{nk} + \sum_{m=0}^{N-1} x(m) W_{2N}^{-mk} W_{2N}^{2Nk} W_{2N}^{-k}. \quad (\text{A.5})$$

Writing the W_{2N} 's as separate terms here makes it clear that we can make some simplifications. The first simplification is noting that $W_{2N}^{2N} = 1$ and therefore $W_{2N}^{2Nk} = 1^k = 1$. Next we can write this equation as a single summation by factoring out $W_{2N}^{-k/2}$ as follows:

$$Y(k) = W_{2N}^{-k/2} \sum_{n=0}^{N-1} x(n) [W_{2N}^{nk} W_{2N}^{k/2} + W_{2N}^{-nk} W_{2N}^{-k/2}]. \quad (\text{A.6})$$

The term inside the square brackets can in turn be written as a single cosine term

$$Y(k) = 2W_{2N}^{-k/2} \sum_{n=0}^{N-1} x(n) \cos \frac{\pi(2n+1)k}{2N}, \quad (\text{A.7})$$

and therefore

$$Y(k) = 2W_{2N}^{-k/2} \text{Re} \left[W_{2N}^{k/2} \sum_{n=0}^{N-1} x(n) W_{2N}^{nk} \right]. \quad (\text{A.8})$$

The summation in Equation A.8 is exactly the $2N$ -point DFT of $x(n)$ with N zeros appended as $x(n)$ was originally defined as a dataset of size N . Finally, we define the DCT $C(k)$ as

$$C(k) = \sum_{n=0}^{N-1} x(n) \cos \frac{\pi(2n+1)k}{2N}, \quad (\text{A.9})$$

and form a simple relationship between $Y(k)$ and $C(k)$:

$$C(k) = W_{2N}^{k/2} \frac{Y(k)}{2}. \quad (\text{A.10})$$

Appendix B

Kramers' Barrier Hopping Problem

In this appendix, we present an overview of the calculations associated with the rate of particle exchange as presented in Reference [38] and as such we use notation similar to that used in the original article.

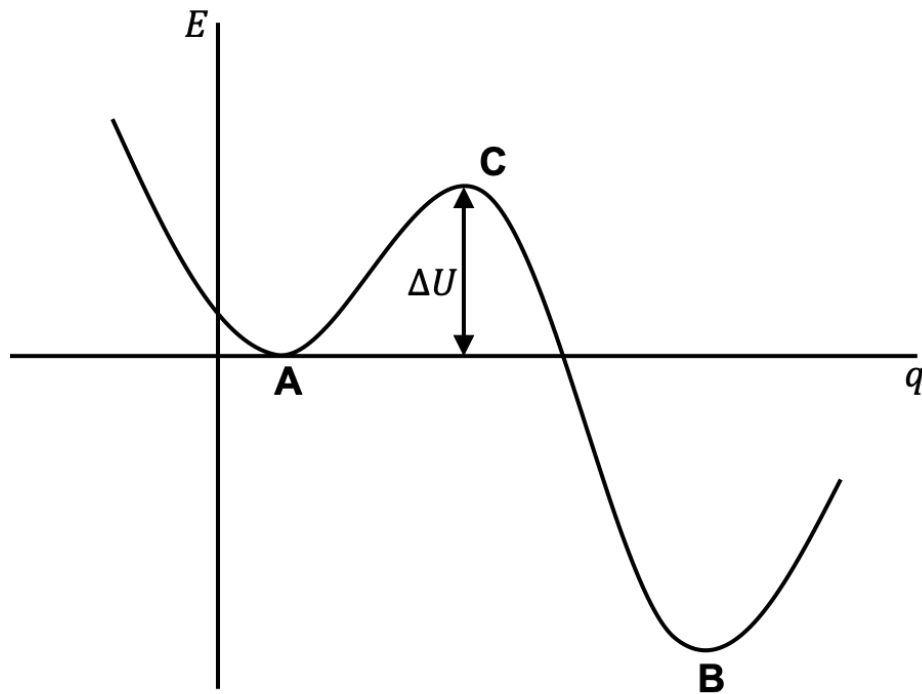


Figure B.1: Illustration of Kramers transition state problem of a particle trapped in a potential field with a smooth barrier.

The problem, illustrated in Figure B.1, states that a particle is originally located at A inside the potential well defined by the potential function U . The height of the potential barrier ΔE is large relative to $k_B T$ such that the process of a particle moving over the barrier to the bound state at B is slow. As the process is slow, at any moment it can be compared to stationary diffusion for which a diffusion current can be written as

$$J = -\frac{k_B T}{\zeta} e^{-U/(k_B T)} \frac{\partial}{\partial q} (\rho e^{U/(k_B T)}), \quad (\text{B.1})$$

where q is the position coordinate of the system, ζ is the friction coefficient and ρ is the density. The probability in unit time that a particle that is originally at A will overcome the energy barrier and escape to the state at B is given by the reaction velocity:

$$k = \frac{J}{n_A}, \quad (\text{B.2})$$

where n_A is the number of particles bound to state A . In particular, the problem is concerned with the transition between the two points A and B so the diffusion current can be written as:

$$J = \frac{k_B T |\rho e^{U/(k_B T)}|_B^A}{\int_A^B \zeta e^{U/(k_B T)} dq}. \quad (\text{B.3})$$

To evaluate this integral, particles are assumed to be equilibrated such that they are Boltzmann distributed at position A and correspond to a quasi-stationary diffusion of a quasi-infinite supply of Boltzmann-distributed particles from position A to B . Then, as there are effectively no particles at position B with the majority of particles located near A the current density becomes

$$J = \frac{k_B T}{\zeta} \rho_A \left[\int_A^B e^{U/(k_B T)} dq \right]^{-1}, \quad (\text{B.4})$$

where ρ_A is the density of particles near A . The integral in the current density can be

approximated by assuming that the main contribution to the integral comes from a small region around the potential barrier at C . Then approximating the potential function as a harmonic oscillator with frequency ω'

$$U_C = \Delta E - \frac{1}{2}(2\pi\omega')^2(q - q_C)^2, \quad (\text{B.5})$$

The integral can be approximated:

$$\int_A^B e^{U/(k_B T)} dq \approx e^{\Delta E/(k_B T)} \int_{-\infty}^{\infty} e^{-(2\pi\omega')^2(q - q_C)^2} dq = \frac{1}{\omega'} \sqrt{\frac{k_B T}{2\pi}} e^{\Delta E/(k_B T)}. \quad (\text{B.6})$$

Similarly, one can approximate the number of particles near A , n_A by assuming that U at this point can be approximated by another harmonic oscillator with frequency ω . Then,

$$n_A = \int_{-\infty}^{\infty} \rho_A e^{-(2\pi\omega)^2 q^2/(2k_B T)} dq = \frac{\rho_A}{\omega} \sqrt{\frac{k_B T}{2\pi}}. \quad (\text{B.7})$$

Substituting the results in Equation B.6 and B.7 yields the following relationship for the reaction velocity:

$$k \approx \frac{2\pi\omega\omega'}{\zeta} e^{-\Delta E/(k_B T)}. \quad (\text{B.8})$$

Therefore, the rate of chain exchange is proportional to the exponential of the energy barrier associated with hopping.

Bibliography

- [1] D. J. Grzetic, R. A. Wickham, and A.-C. Shi, J. Chem. Phys. **140**, 244907 (2014).
- [2] D. J. Grzetic, *Polymer Dynamics: A Self-Consistent Field-Theoretic Approach*, Master's thesis, University of Guelph, Guelph, Ontario, Canada (2011).
- [3] K. Kataoka, A. Harada, and Y. Nagasaki, Adv. Drug Delivery Rev. **47**, 113 (2001).
- [4] G. Gaucher, M.-H. Dufresne, V. P. Sant, N. Kang, D. Maysinger, and J.-C. Leroux, J. Controlled Release **109**, 169 (2005).
- [5] J. Lu, F. S. Bates, and T. P. Lodge, Macromolecules **48**, 2667 (2015).
- [6] F. C. Frank and J. S. Kasper, Acta Cryst. **11**, 184 (1958).
- [7] W. Jiang, Y. Qiang, W. Li, F. Qiu, and A.-C. Shi, Macromolecules **51**, 1529 (2018).
- [8] N. Xie, W. Li, F. Qiu, and A.-C. Shi, ACS Macro Lett. **3**, 906 (2014).
- [9] K. Kim, A. Arora, R. M. Lewis III, M. Liu, W. Li, A.-C. Shi, K. D. Dorfman, and F. S. Bates, PNAS **115**, 847 (2018).
- [10] D. J. Grzetic, *Connecting Structure Evolution and Chain Diffusion in Dense Polymeric Systems using Dynamical Self-Consistent Field Theory*, Ph.D. thesis, University of Guelph, Guelph, Ontario, Canada (2015).
- [11] R. Spencer, *Diblock Copolymer Micelle Structure and Dynamics near the Order-Disorder Transition*, Ph.D. thesis, University of Guelph, Guelph, Ontario, Canada (2014).

- [12] P. Špaček, J. Appl. Polym. Sci. **32**, 4281 (1986).
- [13] P. Špaček and M. Kubin, J. Appl. Polym. Sci. **30**, 143 (1985).
- [14] Y. Wang, C. M. Kausch, M. Chun, R. P. Quirk, and W. L. Mattice, Macromolecules **28**, 904 (1995).
- [15] R. S. Underhill, J. Ding, V. I. Birss, and G. Liu, Macromolecules **30**, 8298 (1997).
- [16] J. van Stam, S. Creutz, F. C. De Schryver, and R. Jérôme, Macromolecules **33**, 6388 (2000).
- [17] K. Prochazka, D. Kiserow, C. Ramireddy, Z. Tuzar, P. Munk, and S. E. Webber, Macromolecules **25**, 454 (1992).
- [18] M. Tian, A. Qin, C. Ramireddy, S. E. Webber, and P. Munk, Langmuir **9**, 1741 (1993).
- [19] M. Pacovská, K. Prochazka, Z. Tuzar, and P. Munk, Polymer **34**, 4585 (1993).
- [20] S.-H. Choi, F. S. Bates, and T. P. Lodge, Phys. Rev. Lett. **104**, 047802 (2010).
- [21] J. Lu, S.-H. Choi, F. S. Bates, and T. P. Lodge, ACS Macro Lett. **1**, 982 (2012).
- [22] A. Halperin and S. Alexander, Macromolecules **22**, 2412 (1989).
- [23] M. W. Matsen, J. Chem. Phys. **113**, 5539 (2000).
- [24] M. W. Matsen, Eur. Phys. J. E **36** (2013).
- [25] M. W. Matsen, Macromolecules **45**, 2161 (2012).
- [26] M. Muller and K. Daoulas, J. Chem. Phys **129**, 164906 (2008).
- [27] T. Haliloglu, I. Bahar, B. Erman, and W. L. Mattice, Macromolecules **29**, 4764 (1996).
- [28] A. J. Peters and T. P. Lodge, Macromolecules **50**, 6303 (2017).

- [29] Z. Li and E. E. Dormidontova, *Soft Matter* **7**, 4179 (2011).
- [30] Z. Li and E. E. Dormidontova, *Macromolecules* **43**, 3521 (2010).
- [31] N. A. Spenley, *Europhys. Lett.* **49**, 534 (2000).
- [32] F. A. G. Daza, J. B. Avalos, and A. D. Mackie, *Langmuir* **33**, 6794 (2017).
- [33] T. Haliloglu and W. L. Mattice, *Chem. Eng. Sci.* **49**, 2851 (1994).
- [34] P. J. Hoogerbrugge and J. M. V. A. Koelman, *Europhys. Lett.* **19**, 155 (1992).
- [35] P. Español and P. Warren, *Europhys. Lett.* **30**, 191 (1995).
- [36] V. Ganesan and V. Pryamitsyn, *J. Chem. Phys.* **118**, 4345 (2003).
- [37] P. E. Rouse, *J. Chem. Phys.* **21**, 1272 (1953).
- [38] H. A. Kramers, *Physica* **7**, 284 (1940).
- [39] M. Murat, G. S. Grest, and K. Kremer, *Macromolecules* **32**, 595 (1999).
- [40] W. H. Press, B. P. Flannery, S. A. Teukolsky, and W. T. Vetterling, *Numerical Recipes: The Art of Scientific Computing* (Cambridge University Press, Cambridge, 1986).
- [41] P. S. Pacheco, *Parallel Programming with MPI* (Morgan Kaufmann Publishers, San Francisco, California, 1997).
- [42] J. Makhoul, *IEEE Trans. Acoust., Speech, Signal Processing* **ASSP-28**, 27 (1980).
- [43] M. W. Matsen, *J. Chem. Phys.* **114**, 8165 (2000).
- [44] J.-L. Barrat and G. H. Fredrickson, *Macromolecules* **24**, 6378 (1991).
- [45] G. H. Fredrickson and H. Orland, *J. Chem. Phys.* **140**, 084902 (2014).